



**MATEUS AQUINO GONÇALVES**

**Use of *Wavelet* Signals in Molecular Dynamics Simulations of  
paramagnetic materials employed as potential spectroscopic probes**

**LAVRAS-MG**

**2018**

MATEUS AQUINO GONÇALVES

**Use of *Wavelet* Signals in Molecular Dynamics Simulations of  
paramagnetic materials employed as potential spectroscopic probes**

Tese apresentada à Universidade Federal de Lavras,  
como parte das exigências do Programa de Pós-  
Graduação em Agroquímica, área de concentração em  
Química/Bioquímica, para a obtenção do título de  
Doutor.

Orientador

Dr. Teodorico de Castro Ramalho

**LAVRAS-MG**

**2018**

Ficha catalográfica elaborada pelo Sistema de Geração de Ficha Catalográfica da Biblioteca  
Universitária da UFLA, com dados informados pelo(a) próprio(a) autor(a).

Gonçalves, Mateus Aquino.

Use of *Wavelet* Signals in Molecular Dynamics Simulations of  
paramagnetic materials employed as potential spectroscopic probes /  
Mateus Aquino Gonçalves. - 2018.

158 p. : il.

Orientador(a): Teodorico Castro Ramalho.

.

Tese (doutorado) - Universidade Federal de Lavras, 2018.

Bibliografia.

1. Cancer. 2. Agentes de Contraste. 3. Constante de  
Acoplamento Hiperfino. I. Ramalho, Teodorico Castro. . II. Título.

**Mateus Aquino Gonçalves**

**Use of *Wavelet* Signals in Molecular Dynamics Simulations of  
paramagnetic materials employed as potential spectroscopic probes**

Tese apresentada à Universidade Federal de Lavras,  
como parte das exigências do Programa de Pós-  
Graduação em Agroquímica, área de concentração em  
Química/Bioquímica, para a obtenção do título de  
Doutor.

APROVADA em 28 de 09 de 2018.

Dr. Sergio Emanuel Galembeck  
Dra. Mónica Oliva Domínguez  
Dra. Katia Julia de Almeida  
Dr. Matheus Puggina de Freitas

USP  
UJI  
UFLA  
UFLA

Orientador

Dr. Teodorico de Castro Ramalho

**LAVRAS-MG**

**2018**

*Dedico este trabalho aos meus queridos pais, Arismar e Maria Célia.  
Com carinho, OFEREÇO.*

## AGRADECIMENTOS

A Deus, um importante guia na minha trajetória, que com sua infinita sabedoria me manteve persistente diante de toda ansiedade e insegurança.

Aos meus pais, Arismar e Maria Célia, por todo amor, carinho e dedicação com seus filhos. Fonte de inspiração diária, exemplo de honestidade e humildade.

Aos meus irmãos, Juninho e Ana Flávia, pelo carinho e diversão no “sítio”.

Ao professor e amigo Téo. Desde a graduação nas suas excelentes aulas de Físico-química, (motivo que me fez pedir estágio no laboratório) até a conclusão desta Tese se mostrou um cara comprometido e dedicado com seus alunos. Com certeza, levarei seus ensinamentos e seu carisma por toda vida. Obrigado Téo, por ser essa pessoa tão inspiradora e dedicada.

Ao professor Matheus, por todo ensinamento, conversas e mensagens de incentivo, fundamentais no período de um Doutorado.

Aos professores e amigos Lizandro e Fernando Peixoto da Universidade Federal Fluminense pela parceria e toda a ajuda durante a realização do trabalho. Sem a participação deles, com certeza, esse trabalho não seria realizado, foram essenciais.

Aos amigos do departamento de Química: Willian, João, Mozarte e Josué.

Aos amigos de Lavras e UFLA: Paulo (Pingo), Cristian (Poka), Ederson (Nenzo) e Lucas Panissa.

Aos amigos do Laboratório de Química Computacional (era do gelo) pela amizade e momentos de descontração.

Aos amigos, Daiana, Giovanna, Francisco, Bruna e Joyce.

Aos amigos de Samonte (sempre presentes): Adriano, Capivara, a “Galera do mal”, Márcio e etc.

O presente trabalho foi realizado com o apoio da Coordenação de Aperfeiçoamento de Pessoal de Nível Superior -Brasil (Capes)- Código de Financiamento 001.

Obrigado!

**"Correndo pelo mesmo chão. O que encontramos?  
Os mesmos velhos medos." Wish You Were Here  
Pink Floyd**

***"As nuvens mudam sempre de posição, mas são sempre nuvens no céu.  
Assim devemos ser todo dia, mutantes, porém leais com o que pensamos e sonhamos;  
lembre-se, tudo se desmancha no ar, menos os pensamentos".  
Paulo Baleki***

## RESUMO GERAL

Atualmente, o câncer é uma das maiores causas de morte no mundo, tendo como grande dificuldade o diagnóstico na sua fase inicial. Dentre as técnicas empregadas no diagnóstico do câncer, podemos destacar a Ressonância Magnética de Imagem (RMI). A RMI é um método de diagnóstico eficaz, que por meio do uso de agentes de contraste (ACs) é capaz de localizar tumores de várias naturezas. Os ACs mais utilizados são os complexos de  $Gd^{3+}$ , apesar de serem muito eficazes, são muito tóxicos para o organismo. Assim, novos ACs estão sendo estudados para substituir os complexos de  $Gd^{3+}$ , dentre eles as nanopartículas superparamagnéticas de óxido de ferro (SPIONs) e os complexos de  $Ni^{2+}$  (paraCEST) se destacam. Os SPIONs e os paraCEST são capazes de alterar o tempo de relaxação  $T_1$  e  $T_2$  das moléculas de água do organismo. Neste trabalho, estudamos a face 100 de vários óxidos de ferro ( $\gamma$ - $Fe_2O_3$ ,  $\delta$ - $FeOOH$ ,  $\alpha$ - $FeOOH$ ,  $Fe_2O_3$  e  $Fe_3O_4$ ) e os complexos de  $Ni^{2+}$  ( $[Ni(ACAC)_2(H_2O)_2]$  e  $[Ni(TEA)]^{2+}$ ) coordenadas com moléculas de água explícitas, afim de obter as constantes de acoplamento hiperfino ( $A_{iso}$ ) do  $^1H$  e  $^{17}O$  das moléculas de água. Apresentamos também uma nova metodologia para a seleção de cálculos de dinâmica molecular (DM), denominada OWSCA (*Optimal Wavelet Signal Compression Algorithm*). Os resultados teóricos sugerem que os óxidos de ferro estudados podem ser promissores substitutos dos ACs clássicos, baseados em complexos de  $Gd^{3+}$ . O método OWSCA se mostrou eficiente e pode ser usado no tratamento dos sinais de diferentes sistemas.

Palavras-chave: Câncer, Agentes de Contraste, RMI, Constante de Acoplamento Hiperfino, OWSCA.



## GENERAL ABSTRACT

Currently, the cancer is one of the biggest causes of death in the world, having as great difficulty the diagnosis in its initial phase. Among the techniques used in the cancer diagnosis, we can highlight the Magnetic Resonance Imaging (MRI). The MRI is an effective diagnostic method, which by means of the use of contrast agents (CAs) is able to locate tumors of various natures. The most used CAs are the  $Gd^{3+}$  complexes, although they are very effective and very toxic to the organism. Thus, new CAs are being studied to replace the  $Gd^{3+}$  complexes, among them superparamagnetic iron oxide nanoparticles (SPIONs) and the  $Ni^{2+}$  complexes (paraCEST) stand out. The SPIONs and the paraCEST are able to change the relaxation time  $T_1$  and  $T_2$  of the water molecules of the organism. In this work, we studied the face 100 of various iron oxides ( $\gamma$ - $Fe_2O_3$ ,  $\delta$ - $FeOOH$ ,  $\alpha$ - $FeOOH$ ,  $Fe_2O_3$  and  $Fe_3O_4$ ) and the  $Ni^{2+}$  complexes ( $[Ni(ACAC)_2(H_2O)_2]$ ,  $[Ni(TEA)]^{2+}$ ) coordinating with explicit water molecules, in order to obtain the hyperfine coupling constants ( $A_{iso}$ ) of  $^1H$  and  $^{17}O$  atoms of the water molecules. We also present a new methodology for the selection of molecular dynamics (MD) calculations, OWSCA (*Optimal Wavelet Signal Compression Algorithm*). The theoretical results suggest that the iron oxides studied may be promising substitutes for classic CAs, based on  $Gd^{3+}$  complexes. The OWSCA method is efficient and can be used to treat signals from different systems.

Keywords: Cancer. Contrast Agents. MRI. Hyperfine Coupling Constant. OWSCA

## LIST OF FIGURES FISRT PART

### THEORETICAL BACKGROUND

Figure 1- Behavior of $e^x$ , where $x = r$ (solid line, STO) and $x = r_2$ (dashed line, GTO). .....	18
Figure 2 - EPR spectrum showing the magnitude of the isotropic hyperfine coupling.....	20
Figure 3 - Spectral density for different Larmor frequencies and rotational correlation times $\tau_c$ . .....	22
Figure 4 - Face 100 of the magnetite with the water molecules.....	23
Figure 5 - PCM model with the cavity formed by spheres centered on the atoms.....	24
Figure 6 - Representation of the wavelet in different location-scale sets.....	28
Figure 7 - Illustration of the wavelet decomposition process. a) calculation of the wavelet coefficient in a region of the domain, b) translation of the mother wavelet, c) change of scale. ....	29
Figure 8 - Haar wavelet.....	30
Figure 9 - Molecular graph showing the critical points of the bond. ....	31
Figure 10 - Graphical representation of the result of NCI calculations. ....	33

### SECOND PART

#### Article 1

Figura 1 - Parâmetros que influenciam a relaxação das moléculas de água.....	57
Figura 2 - Ligantes mais utilizados nos complexos de $Gd^{3+}$ .....	58
Figura 3 - Face 100 do a) $Fe_3O_4$ com moléculas de água, e do b) $\delta$ - $FeOOH$ com moléculas de água. ....	60
Figura 4 - Estrutura do complexo a) $[MnH_3buea(OH)]-2$ b) $[MnH_3buea(OH)]-2$ com moléculas de água. ....	61
Figura 5 - Estrutura dos complexos de $Ni^{2+}$ .....	62
Figura 6 - Híbrido SPION@CPP-Fe. ....	64

#### Article 2

Figure 1- Graph of the auto-correlation function for the time in picoseconds. a) $[Fe(H_2O)_6]$ b) $\gamma$ - $Fe_2O_3$ . The blue curve is the correction and the red curve the adjustment done. ....	80
Figure 2 - The OWSCA is summarized. ....	83
Figure 3 - Energy of MD $[Fe(H_2O)_6]^{2+}$ conformations (original and compressed) at each time (fs). ....	85
Figure 4 - Wavelet coefficients of $x(t)$ , $[Fe(H_2O)_6]^{2+}$ .....	85
Figure 5 - Optimal thresholds $\delta_j^*$ (Vertical axis: threshold value; Horizontal axis: individual threshold),	

[Fe(H <sub>2</sub> O) <sub>6</sub> ] <sup>2+</sup> .....	86
Figure 6 - Number of selected [Fe(H <sub>2</sub> O) <sub>6</sub> ] <sup>2+</sup> structures versus absolute error for OWSCA and SI methods. .....	87
Figure 7 - a) [Fe(H <sub>2</sub> O) <sub>6</sub> ] <sup>2+</sup> and γ-Fe <sub>2</sub> O <sub>3</sub> structures with water molecules, b) bond critical points (BCP)..	96
Figure 8 - Spin-density map of the compounds (the isosurface contour value is 0.0004). a) [Fe(H <sub>2</sub> O) <sub>6</sub> ] <sup>2+</sup> with water molecules b) γ-Fe <sub>2</sub> O <sub>3</sub> with water molecules. ....	97

### Article 3

Figure 1 - Energy of MD conformations (original and compressed) at each time (fs). a) [Fe(H <sub>2</sub> O) <sub>6</sub> ] <sup>2+</sup> complex and b) δ-FeOOH. ....	111
Figure 2 - Aiso values for the studied oxides. ....	116
Figure 3 - Structure of the iron oxide with water molecules and their respective spin-density map (the isosurface contour value is 0.0004). a) δ-FeOOH; b) α-FeOOH; c) Fe <sub>2</sub> O <sub>3</sub> ; d) Fe <sub>3</sub> O <sub>4</sub> .....	119
Figure 4 - NCI isosurfaces and reduced density gradient RDG vs. sign(λ <sup>2</sup> ) ρ (ua). a) δ-FeOOH; b) α- FeOOH; c) Fe <sub>2</sub> O <sub>3</sub> ; d) Fe <sub>3</sub> O <sub>4</sub> .....	121
Figure S1- OWSCA is summarized. ....	131
FigureS2- Energy of MD conformations (original and compressed) at each time (fs). a) goethite b) hemathite, c)magnethite. ....	132
Figure S3 - Optimal thresholds δ <sub>j</sub> <sup>*</sup> .....	133

### Article 4

Figure 1 - Flowsheet of the OSWCA applied to calculate the relaxation parameters. ....	143
Figure 2 - Energy of MD conformations (original and compressed) at each time (fs). a) Fe <sub>3</sub> O <sub>4</sub> , b) [Ni(ACAC) <sub>2</sub> (H <sub>2</sub> O) <sub>2</sub> ] , c) [Ni(TEA)] <sup>2+</sup> .....	144
Figure 3 - Ni <sup>2+</sup> complex a) [Ni(ACAC) <sub>2</sub> (H <sub>2</sub> O) <sub>2</sub> ] , b) [Ni(TEA)] <sup>2+</sup> .....	146
Figure 4 - Relaxivity of Ni <sup>2+</sup> complexes a) [Ni(ACAC) <sub>2</sub> (H <sub>2</sub> O) <sub>2</sub> ], b) [Ni(TEA)] <sup>2+</sup> .....	148
Figure 5 - MD system of the [Ni(ACAC) <sub>2</sub> (H <sub>2</sub> O) <sub>2</sub> ] complex .....	149

## Summary

FIRST PART.....	13
GENERAL INTRODUCTION AND THEORETICAL BACKGROUND.....	13
1.0-INTRODUCTION .....	13
2.0-General objective .....	14
5.0-Bibliographic references .....	34
SECOND PART-ARTICLES .....	51
Article 1-Agentes de Contraste para Ressonância Magnética de Imagem: Uma revisão .....	52
Article 2-Optimal Wavelet Signal Compression as an Efficient Alternative to Investigate Molecular Dynamics Simulations: Application to Thermal and Solvent Effects of MRI Probes .....	73
Article 3-Comparing Structure and Dynamics of Solvation of Different Iron Oxide Phases for Enhanced Magnetic Resonance Imaging .....	106
Article 4-NMR Relaxation Parameters of MRI probes revealed by optimal wavelet signal compression of molecular dynamics simulations .....	134
ATTACHMENT .....	154

## **FIRST PART**

### **GENERAL INTRODUCTION AND THEORETICAL BACKGROUND**

#### **1.0-INTRODUCTION**

Currently, cancer is one of the biggest causes of death in the world (FERNANDES; MAFRA, 2005). The number of cases involving this disease has increased considerably, being one of the most serious and ancient problems faced by humankind (DUNN, 2012). One of the main reasons for this high incidence is the difficulty in diagnosing it, mainly in its initial phase. Furthermore, it is well-known that cancer has a variety of types and, among this range, brain cancer can be highlighted as one of the most serious occurrences. In Brazil, for example, it is the leading cause of death in the female population (INCA, 2017).

Accordingly, one of the most effective methods to determine the size and location of tumors and cancers (such as brain cancer) is the Magnetic Resonance Imaging (MRI) technique. In fact, the MRI of brain is a recent method that has consolidated itself as an important tool in the early diagnosis of cancer in this region. The main feature of this diagnostic method is its high sensitivity (greater than 95%) in the detection of small foci of tumor nodules or microcalcifications (CECILIA, 2008; CHALA; BARROS, 2007). Basically, MRI is a method of imaging established in clinical practice, that due to its high ability in differentiating tissues, it has a wide spectrum of applications, which extends to all parts of the human body and explores anatomical and functional aspects (MAZZOLA, 2009). Moreover, it is a noninvasive technique based on the magnetic properties of the  $^1\text{H}$  nuclei (due to the high concentration of water in the human body;  $^1\text{H}$  is the most abundant atom). Although the MRI technique is one of the most effective in diagnosing cancer, it presents some limitations, such as the fact that employing only the natural relaxation of the  $^1\text{H}$  of water does not always guarantee clear images of the tissues. Thus, contrast agents (CAs) are usually used to improve tissue contrast by means of decreasing relaxation times ( $T_1$  and  $T_2$ ) of the  $^1\text{H}$  atoms of water (FILIPPE; CARVALHO, 2011).

CAs are paramagnetic compounds and their use is of utmost importance for a better visualization of the images in the MRI exams. Currently, the most commonly used CAs are  $\text{Gd}^{3+}$  complexes with different ligands, such as DOTA, DTPA, EDTA, etc. However, although they play an important role in the contrast of images (being more common the images of veins and of

cerebral tumors formation), they are very toxic to the human organism. Thus, new CAs have been studied in order to replace the  $Gd^{3+}$  complexes. The superparamagnetic iron oxide nanoparticles (SPIONs) can be highlighted among these prospective compounds. These nanoparticles have great interest in nanoscience and nanotechnology due to their nanoscale dimensions, non-toxic nature and superior magnetic properties. Among their features, the main ones are reduction of the relaxation time  $T_2$  and excellent magnetic properties (which arise from a combination of the atomic composition and the crystalline structure), biocompatibility and biodegradability, which act mainly changing the  $T_2$  and  $T_2^*$  values of tissue water hydrogen (STEPHEN; KIEVIT; ZHANG, 2012).

## **2.0-General objective**

This work is focused on the spectroscopic properties of the face 100 of various iron oxides ( $\gamma$ - $Fe_2O_3$ ,  $\delta$ - $FeOOH$ ,  $\alpha$ - $FeOOH$ ,  $Fe_2O_3$  and  $Fe_3O_4$ ) and of  $Ni^{2+}$  complexes ( $[Ni(ACAC)_2(H_2O)_2]$ ,  $[Ni(TEA)]^{2+}$ ) and on the development of an algorithm capable of selecting the structures of Molecular Dynamics, called OWSCA. Thus, it aimed to study the thermal and electronic effects of potential MRI contrast agents by means of hyperfine coupling constant ( $A_{iso}$ ) and spectral density calculations.

## **3.0-THEORETICAL BACKGROUND**

### **3.1-Cancer**

Currently, cancer is considered the second leading cause of death; the first being cardiovascular diseases (ALMEIDA, 2005; MARTÍN; LI, 2011). According to INCA (Instituto Nacional de Cancer), cancer is the name given to a set of more than 100 diseases that have in common the disordered (malignant) growth of cells, which can invade tissues and organs and may spread (metastases) to other body regions. Among this range, brain cancer is one of the most common types in the world, the causes are varied and often unknown. When a person has a tumor in the lung, for example, some cells from that lesion may fall into the bloodstream and settle in any part of the body, including the brain (INCA, 2017).

According to the NBTS (National Brain Tumor Society) brain tumors can be deadly,

significantly impact quality of life, and change everything for a patient. They do not discriminate, inflicting men, women, and children of all races and ethnicities (NBTS, 2018). In Brazil, it is estimated that approximately 11.320 people will be diagnosed brain tumors in the year 2018 (5,810 in men and 5,510 in women) (INCA, 2017).

There are a variety of diagnostic techniques employed in the identification of cancer, such as tomography, magnetic resonance imaging (MRI) and endoscopic ultrasound; however, in many occasions, the diagnosis does not bring about the desired accuracy for the identification of the disease, and many patients are victimized by this limitation (LI et al., 2013). Especially in the case of the MRI technique, it is often difficult to have clear images. Therefore, the use of contrast agents (CAs) are normally required, once those ones have the ability of increasing the relaxation of the  $^1\text{H}$  and  $^{17}\text{O}$  nuclei spins present in water molecules of the human body, which, as a consequence, intensifies the NMR signal. Thus, MRI technique is described in more details in the article 1 of this thesis, as well as the main CAs currently used and those under studies.

### **3.2-Density Functional Theory (DFT)**

Quantum Mechanics began with the Schrödinger equation (1926). The Schrödinger equation is able to determine the quantum wave function of a system containing all the information necessary to determine the state of the system. However, there are few physical systems that have an analytical solution and even the approximate numerical solution can be computationally unfeasible (CRAMER; TRUHLAR, 2009).

An approximation based only on electronic density was proposed by Thomas (1927) and Fermi (1927); this model is the precursor of the modern so-called Density Functional Theory (DFT). The DFT emerged as an alternative to the traditional *ab initio* and semi-empirical methods in the study of fundamental state properties of molecular systems. The great advantage of DFT over traditional *ab initio* methods (for example, Hartree-Fock or post-Hartree-Fock) lies in the gain of computational speed and memory space. The DFT method is very important and it is used, mainly, for structural optimization calculations and for obtaining spectroscopic properties such as those from ultraviolet, photoelectronic, nuclear magnetic resonance (NMR) and electronic paramagnetic resonance (EPR). Furthermore, this computational method is able to describe relatively large molecular systems with efficiency and low computational costs if

compared to *ab initio* methods. Such performance can be explained by the use of electronic density (instead of the wave function); as consequence, the coulomb repulsion integral needs to be calculated only for the electronic density, which is a three-dimensional function, as  $N^3$ , wherein  $N$  is the number of base functions. On another hand, the *ab initio* methods deal with functions involving more dimensions, such as  $N^4$  or larger (ALCÁCER, 2007; CRAMER; TRUHLAR, 2009; MORGON, N.H; CUSTODIO, 1994).

Accordingly, the basic entity of DFT is the electronic density ( $\rho(r)$ ), which describes the distribution of charges present in a given molecule. The modern concepts of this theory were formulated by Khon and Sham in 1965 and are based on two theorems:

- I- *The wave function of the ground state and hence all the properties of this state are functional of the electronic density,  $\rho(r)$ . Thus, the electronic density of a system will determine the external potential  $v(r)$  and the number of electrons  $N$  and, therefore, the Hamiltonian of the system itself.*
- II- *the ground state energy of a multielectronic system under a given external potential  $v(r)$ , can be written as.*

$$E_v[\rho(r)] = \int v(r)\rho(r)dr + F[\rho] \quad (1)$$

Wherein,  $F$  is called the universal functional of  $\rho$ , which is independent of the external potential  $v(r)$ . Substituting the exact density function of this state by another function close to  $\tilde{\rho}$ , it increases  $E_v$  s, thus:

$$\tilde{E} = \tilde{E}[\tilde{\rho}] = \int v(r)\tilde{\rho}(r)d(r) + F[\tilde{\rho}] \geq E_0 = E[\rho] \quad (2)$$

The total energy of the system in the DFT method uses the resolution of the time-independent Schrödinger equation, which allows determining the ground state structure of a system with many electrons and nuclei:



$$\hat{H}\phi = E\phi \quad (3)$$

The exact resolution of the Schrödinger equation, equation 3, presents a very high level of complexity. Thus, approximations are necessary to enable its use for real systems. One of the most important approximations is the so-called Born-Oppenheimer approximation. Basically, it disregards the movement of nuclei in the molecule, since the nuclear mass is several times greater than the mass of the electrons. Thus, the Schrödinger equation is solved only for the electrons, which are described by a purely electronic wave function in the presence of a potential produced by the nuclei that assume fixed positions in space (ALCÁCER, 2007; JENSEN, 2007).

The DFT method is able to solve systems of many bodies efficiently; however, it is very dependent on the choices of the functional and basis set.

### 3.2.1-Basis set

The basis set is a set of functions used to create the molecular orbitals. Essentially, there are two types of basis set used in electronic structure calculations: Slater-type atomic orbitals (STOs) and Gaussian-type atomic orbitals (GTOs). The Slater functions were the first basis set created; they have important characteristics, once they are associated to representations of hydrogen orbitals. This type of function has the form described in equation 4.

$$X_{\zeta,n,l,m}(r, \theta, \varphi) = NY_{l,m}(\theta, \varphi)r^{n-1}e^{\zeta r} \quad (4)$$

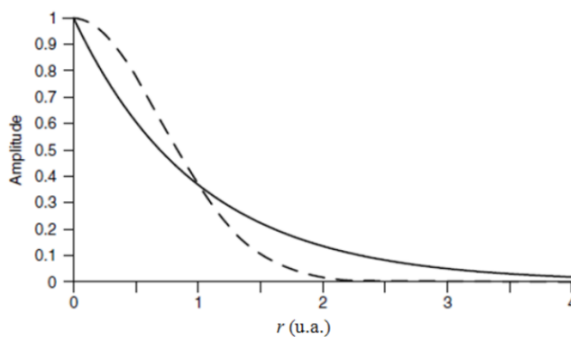
Wherein N is a normalization,  $Y_{l,m}$  constants are the usual spherical harmonic functions and  $\zeta = \frac{Z-W}{n}$  is a constant. The term Z-W stands for the effective nuclear charge, wherein W is a shielding constant. Although the exponential part of the STOs represents well the dependence on the distance between nucleus and electron for the hydrogen atom, it does not have any radial node. These are introduced by making linear combinations of STOs (JENSEN, 2007). The Gaussian-type basis sets (GTOs) were created by Boys (1950) as an alternative to the use of

STOs. In this case, the integrals are more easily solved. The GTOs can be written in terms of polar coordinates as shown in equation 5.

$$X_{\zeta,n,l,m}(r, \theta, \varphi) = NY_{l,m}(\theta, \varphi)r^{2(n-1)-l}e^{-\zeta r^2} \quad (5)$$

Due to the computational efficiency achieved through the use of GTOs, they are normally preferred and widely used as basic functions in electronic structure calculations (JENSEN, 2007). Thus, it was observed, based on equations 4 and 5, that the basis set of STOs followed an exponential behavior  $x = r$ , while the GTOs functions followed an exponential behavior  $x = r^2$ . Figure 1 shows the behavior of  $e^{-x}$  of the STOs and GTOs functions.

Figure 1- Behavior of  $e^{-x}$ , wherein  $x = r$  (solid line, STO) and  $x = r^2$  (dashed line, GTO).



Source: Jensen (2007).

### 3.2.2-DFT Functionals

#### 3.2.2.1-Exchange and correlation functional (XC)

Different classes of approximations for the XC functional followed during the development of the DFT method. The simplest approximation was proposed by Hohenberg and Kohn in 1964, and it is called local density approximation (LDA). The exchange and correlation energy of the LDA functional can be represented according to equation 6.

$$E_{XC}[n] = \int dr^3 n(r) \xi_{XC}(n(r)) \quad (6)$$

Wherein  $E_{XC}$  is the energy of exchange and correlation per particle in an electronic density  $n(r)$ . Another type of exchange and correlation functional is the so-called Generalized Gradient Approximation (GGA). The GGA functional is an improvement applied to the LDA and LSDA functionals. It consisted in the implementation of the density gradient,  $(r) e (r)$ , which can be represented in the electronic correlation energy according to equation 7.

$$E_{XC}[n^\alpha, n^\beta] = \int d^3r \xi^{GGA}(n^\alpha(r), n^\beta(r), \nabla n^\alpha(r), \nabla n^\beta(r)) \quad (7)$$

A functional widely used in GGA is the PBE, which was developed by Perdew, Burke and Ernzerhof. The results obtained with the PBE approach show that for the binding energies of molecules there is a significant improvement, as well as those of atomization, when compared to the results using the LDA (ORGANUM, 2016).

### 3.3-Hyperfine interactions

Electronic Paramagnetic Resonance (EPR) or Electronic Spin Resonance (ESR) is a technique used in systems that have at least one unpaired electron. The existence of this unpaired electron is crucial in an EPR analysis; however, as the most stable molecules exist in singlet state (having all electrons paired), the applicability of the EPR technique is reduced. Nevertheless, this limitation can be seen as an advantage, once it allows the study of specific molecules (FRECUS, 2013).

The EPR analysis consists of contributions from the electronic tensors  $g$  and the hyperfine coupling constant ( $A$ ). In this work specifically, the focus will be in its influence on the values of relaxation times ( $T_1$  and  $T_2$ ) as mentioned in Article 1. The hyperfine coupling constant can be

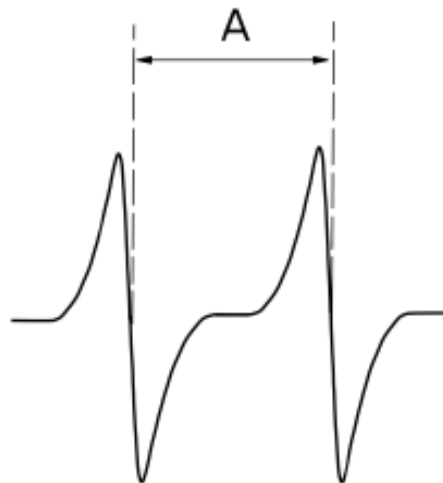
separated into isotropic (HFCC or  $A_{iso}$ ) and three anisotropic coupling constants ( $A_{SD}$ ),  $A_{xx}$ ,  $A_{yy}$  and  $A_{zz}$ , wherein  $A_{xx} + A_{yy} + A_{zz} = 0$  (BÜHL; MAILKIN, 2004).

Thus, hyperfine interactions can be

- 1- a contact interaction that is isotropic ( $A_{iso}$ ) and was originated from the displacement of the unpaired electron over the nucleus;
- 2- a dipole interaction between electron and nucleus spins, which is directional and therefore anisotropic ( $A_{SD}$ ) (OLIVEIRA, 2010).

In Article 1, it is shown that the hyperfine coupling constant is, basically, dependent on the isotropic interaction ( $A_{iso}$ ). The hyperfine coupling constant of a nucleus is directly related to the spectral line spacing and, in the simplest cases, it is essentially the spacing itself (this spacing is measured in MHz). In Figure 2, it is shown a spectrum of EPR, and can be highlighted the hyperfine coupling constant ( $A$ ), which is the difference between the two recorded peaks (FRECUS, 2013).

Figure 2 - EPR spectrum showing the magnitude of the isotropic hyperfine coupling.



Source: Frecus (2013).

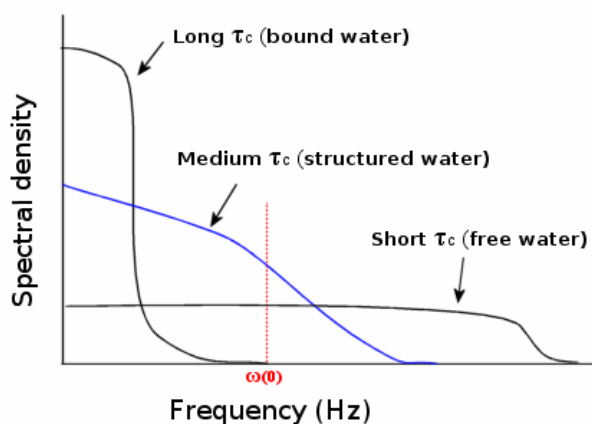
### 3.4- Spectral density ( $J(\omega)$ )

Another way of measuring the values of relaxation parameters ( $T_1$  and  $T_2$ ) is through the spectral density. In 1955, Solomon, building on the work of Bloembergen, Purcell, and Pound, developed a model using correlation times and spectral densities to explain and predict the  $T_1$  and  $T_2$  values of pure liquids and other simple substances. The Spectral density is obtained using the Fourier transform of the correlation function. For spherical molecules in solution, the form of the spectral density is expressed by the equation 8 (VILLA, 2006).

$$J(\omega) = \frac{\tau_c}{1+\omega^2\tau_c^2} \quad (8)$$

Equation 8 is a generic form to obtain the spectral density, which takes into account only correlation functions ( $\tau_c$ ) and the Larmor frequency ( $\omega$ ). The equation of spectral density for two hydrogen protons engaging in a dipole-dipole interaction is shown in article 4 (equation 6) of this thesis. This situation is important because it is the kind of dipole-dipole interaction that takes place between water protons and a paramagnetic ion in solution, such as gadolinium. The analysis and equations are analogous to the proton-proton case with a few important differences (explained in Article 4). However, equation 8 is important to understand the relationship between correlation function and the Larmor frequency. We can observe this relation by Figure 3 (Villa, 2006). Figure 3 shows that the spectral density of protons is very dependent on the Larmor frequency. This graph indicates the number (the spectral- (relating to frequency) density) of protons which are tumbling at or near the Larmor frequency. We are interested in the blue line (correlation function of the soft tissues of the body); if we increase  $B_0$ , the Larmor frequency increases, and so the spectral density at the Larmor frequency reduces. The Larmor frequency is proportional to  $B_0$  ( $\omega_0 = \gamma B_0$ ) (MCROBBIE, 2017).

Figure 3 - Spectral density for different Larmor frequencies and rotational correlation times  $\tau_c$ .



Source: McRobbie (2017).

The Spectral density describes if a certain frequency can induce relaxation and whether it is efficient. It is a shorter way to get the parameters of relaxation ( $T_1$  and  $T_2$ ), i.e., it is not necessary to obtain the hyperfine coupling constant.

### 3.5-Solvent effects

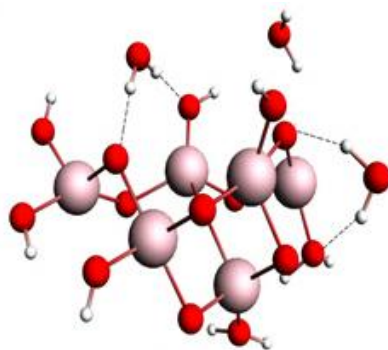
The free energy of solvation ( $\Delta G^*_{\text{solv}}$ ) has a central aspect in the understanding of these physicochemical processes. Great progress has been made in recent years in the attempt of developing models for obtaining this property through molecular dynamics (MD) simulation and quantum calculations (QC). In the computational chemistry approach, two models of solvation are used, explicit and implicit solvent model (PLIEGO, 2006).

#### 3.5.1-Explicit model of solvation

The explicit solvation model is the model in which the solvent molecules are introduced into the system with the solute. It is the most realistic model, but the computational cost is high. This model is very important for analyzing specific interactions, as hydrogen bonds, and it is widely used in molecular dynamics and quantum calculations (as spectroscopy). Figure 4 shows

the face 100 of the magnetite with the water molecules (explicit solvent); it can be observed that the water molecules make hydrogen bonds with the oxygen of the magnetite.

Figure 4 - Face 100 of the magnetite with the water molecules.



Source: By author (2017).

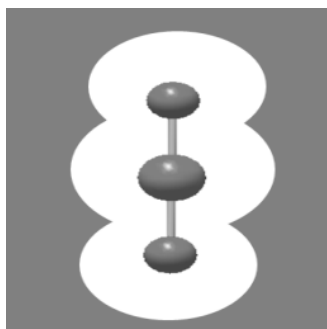
### 3.5.2-Implicit model of solvation

The implicit solvation model (also called the continuous solvation model) is a method for representing the solvents as a continuous medium (characterized by the dielectric constant ( $\xi$ ) of the solvent) instead of the individual solvent molecules (explicit). Implicit solvation models can provide useful quantitative estimations and are computationally cheap (PLIEGO, 2006; ROUX; SIMONSON, 1999). Lars Onsager developed one of the first implicit models of solvation in 1936. This model was a continuation and improvement of the Born model (1920), which was the first model to use a dielectric continuum. From the Onsager model, several other methods of implicit solvation were developed such as PCM, I-PCM, IEF-PCM, and COSMO. In this work, PCM (polarizable continuum model-PCM) solvation model was the focus and, then, it was the chosen model for all the calculations performed herein.

The PCM solvation method is one of the most modern methods used to deal with implicit solvation, and it was developed by Tomasi and collaborators in 1981 (COSSI et al., 1996). In the PCM method, the cavity to accommodate the solute is formed through the Van de Walls radius (Figure 5). The model is based on the Poisson equation (equation 9), which describes the

interaction between an arbitrary charge density  $\rho(r)$  and a continuous dielectric, through the electrostatic potential and the dielectric constant ( $\xi$ ).

Figure 5 - PCM model with the cavity formed by spheres centered on the atoms.



Source: Tomasi (1999).

$$\nabla^2 \phi(r) = -\frac{4\pi\rho(r)}{\xi} \quad (9)$$

The PCM treats the solute via quantum mechanics, calculating its energy through the wave function in vacuum and, posteriorly, including the response of the dielectric-continuous solvent field in the Hamiltonian of the solute. The modified Hamiltonian is employed in a new energy calculation of the solute and the cycle repeats until a consistent result is obtained (TOMASI; MENNUCCI; CANCÈS, 1999).

### 3.6-Molecular Dynamics

The Molecular Dynamics (MD) method studies the physical movements of atoms and molecules in a given system. Generally, the MD methodology is based on the principles of Classical Mechanics and provides information on the microscopic dynamic behavior, which is treated as dependent on time and on the individual atoms that make up the system (NAMBA; SILVA; SILVA, 2008). Furthermore, the MD simulations consist on the numerical solution of the equation of motion, which can be described for a simple atomic system by equations 10, 11 and 12 (NAMBA; SILVA; SILVA, 2008).



$$\vec{F} = \frac{\partial \vec{p}}{\partial t} \quad (10)$$

$$\vec{F} = m \frac{\partial \vec{v}}{\partial t} \quad (11)$$

$$\vec{F} = m \frac{\partial^2 \vec{x}}{\partial t^2} \quad (12)$$

Wherein  $\vec{F}$  is the force acting on each particle of the system at an instant of time  $t$ .

Based on Molecular Mechanics (MM), the molecules are treated as a collection of atoms that can be described by Newtonian forces, i.e., they are treated as a collection of particles joined by harmonic or elastic forces. A complete set of potential interaction among the particles is referred to as “force field”. A force field is a fundamental piece, if not the most important in MM. Basically, a force field is a function that describes the potential energy through contributions of bound and unbound atoms (CHENOWETH; VAN DUIN; GODDARD, 2008).

ReaxFF is a reactive molecular dynamics (MD) method that uses a bond-order-dependent potential energy formulation, in conjunction with time-dependent, polarizable charge descriptions, to continuously describe bond formation and cleavage in a wide range of chemical environments (FANTAUZZI et al., 2014). We briefly describe each type of interaction that constitutes the Reax force field, the total energy can be written as sum of different energy terms as follows:

$$E_{system} = E_{bond} + E_{lp} + E_{over} + E_{under} + E_{val} + E_{tors} + E_{conj} + E_{H-bond} + E_{vdWalls} + E_{Coulomb} \quad (13)$$

Wherein  $E_{bond}$  is the energy of the bond between atoms;  $E_{lp}$  is the energy accounts for unpaired electrons of an atom (therefore classical MD terms do not explicitly compute this term),  $E_{over}$  and  $E_{under}$  are energy penalties which enforce valency;  $E_{val}$  is the angle stretching energy;

$E_{tors}$  corresponds to the torsion energy;  $E_{H-bond}$  is the energy associated with a hydrogen bond  $E_{vdWalls}$  is the van der Waals energy, and, lastly,  $E_{Coulomb}$  is the Coulomb energy (VAN DUIN et al., 2001).

In this work, in order to perform the MD calculations, the REAX-FF software was employed (DUIN, 2002); in each simulation, 300 water molecules were used as explicit solvent coordinated to the iron oxides. 8000 conformations were obtained from each simulation. The REAX-FF is part of the ADF-BAND program package developed by Adri Van Duin and collaborators in the California Institute of Technology. It is a program for modeling chemical reactions with atomistic potentials, which is based on the reactive force field approach. REAX-FF was developed to bridge the gap between quantum chemistry (QC) and empirical force field (EFF). The main difference between traditional unreactive force fields and REAX-FF is that, in REAX-FF, the connectivity is determined by bond orders, which are calculated from interatomic distances which are updated every MD step. This allows bonds to break and form during the simulation. In order to account for nonbonded interactions, such as van der Waals and Coulomb interactions, for a system with changing connectivity, these interactions are calculated between every pair of atoms, irrespective of connectivity. Any excessive close-range nonbonded interactions are avoided by inclusion of a shielding term. In addition, REAX-FF accounts for polarization effects by using a geometry-dependent charge calculation scheme. Thus, the contributions involving the reactive force field and the polarization effects are added in the equation of the traditional force field (equation 13). In the calculations performed herein, the FeOCH force field was employed. FeOCH was developed for iron oxides and oxyhydroxides (ARYANPOUR; VAN DUIN; KUBICKI, 2010).

The MD simulations were very important for the subsequent quantum calculations of  $A_{iso}$ . However, generally, the greatest difficulty of the MD simulations is to select the conformations for the quantum calculations, since to perform the calculations with all the generated conformations is computationally infeasible. Thus, in this work, it was used two independent methods for selecting the structures, IS and OWSCA. The details of each method are discussed in topic 2.6.

### 3.7-Selection Methods of MD Structures

#### 3.7.1-Statistical Inefficiency (SI)

Prof. S Canuto and Prof. K Coutinho have proposed and applied the sequential quantum mechanical/molecular mechanics methodology. This methodology suggests the structure selection by using Statistical Inefficiency (SI) calculations and has been previously reviewed on several different occasions (COUTINHO; CANUTO; ZERNER, 2000). The method can be efficiently applied in the treatment of MD signals.

The method uses the autocorrelation energy function to calculate the correlation time ( $\tau$ ), which is obtained by an exponential decay following a Markovian process, equation 14. Thus, through the autocorrelation function, it is possible to calculate the correlation time ( $\tau$ ) and, then obtaining the statistical inefficiency (s), equation 15. The correlation time between the structures shows that they are statistically different (COUTINHO; CANUTO, 1997; COUTINHO; CANUTO; ZERNER, 2000).

$$C(n) = \sum_{i=1}^N c_i e^{-n/\tau_i} \quad (14)$$

$$\tau = \int_0^{\infty} C(t) dt \quad (15)$$

Following this line, the statistical inefficiency (s) occurs when the configurations are separated by  $2\tau$  ( $s = 2\tau$ ) or larger intervals, i.e., in this interval, there is no correlation among the configurations. Thus, the SI method was used to obtain the uncorrelated MD configurations. In this sense, it is observed that the uncorrelated structures are able to present statistically the same results of all the structures obtained by the MD simulation (COUTINHO et al., 2007).

#### 3.7.2-Optimal Wavelet Signal Compression Algorithm (OWSCA)

Another selection method of MD structures was also used in this work, the so-called Optimal Wavelet Signal Compression Algorithm (OWSCA), which is based on the wavelet

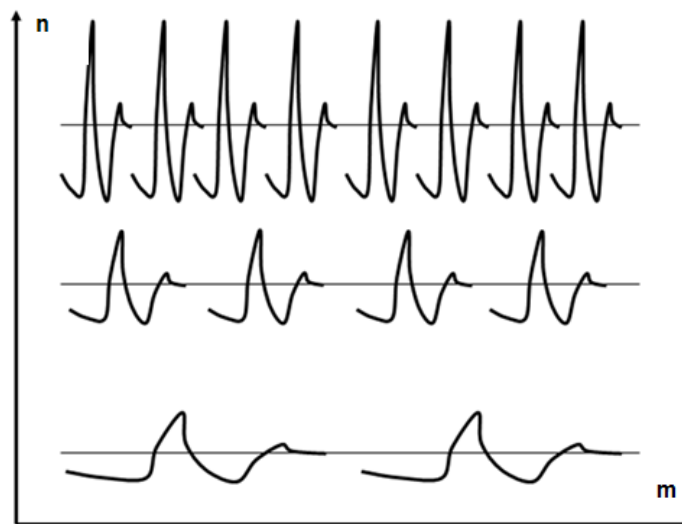
transform. The wavelets are functions used as tools for processing or manipulating data in order to analyze them at different resolution scales, and aiming, mainly, to detect transients, remove noise and data compress (GONÇALVES et al., 2017; SANTOS, 2014).

Wavelet transformations can be interpreted as mechanisms for data decomposition into their constituent parts, allowing them to be analyzed in different ranges of frequencies and space (GONÇALVES et al., 2017; SANTOS, 2014). The discrete wavelet transform can be defined by equation 16.

$$d_{n,m} = \int_{-\infty}^{\infty} f(t)\Psi_{n,m}dt \quad (16)$$

Wherein  $d_{n,m}$  is the discrete wavelet transform of  $f(t)$ , which results in a vector of coefficients  $d$ . It is possible to calculate the value of the wavelet from the shrinkage (or expansion) and translation of a simple wavelet-mother function ( $\Psi$ ). When changing the index  $m$  changes the location of the wavelet in the domain, changing the index  $n$  changes the scale of the wavelet (shrinking or stretching function). The behavior of this function can be shown in Figure 6 (SANTOS, 2014).

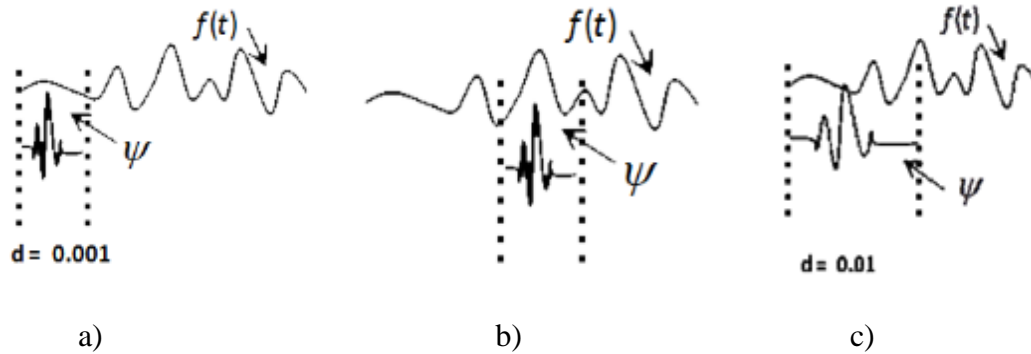
Figure 6 - Representation of the wavelet in different location-scale sets.



Source: Santos (2014).

Considering a continuous function  $f(t)$ , its treatment by the wavelet transform basically consists of three steps. The first step (Figure 7 (a)) is based on comparing a particular wavelet to a region of the function, by means of the internal product of equation 16. The next step (Figure 7 (b)) consists of translating the wavelet and performing the same procedure as before; this step is repeated until the full domain is covered. Lastly, the third step (Figure 7 (c)) is to repeat the previous steps for a different scale (SANTOS, 2014).

Figure 7 - Illustration of the wavelet decomposition process. a) calculation of the wavelet coefficient in a region of the domain, b) translation of the mother wavelet, c) change of scale.

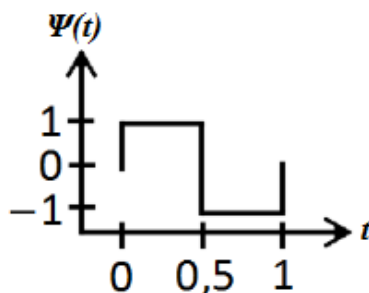


Source: Santos (2014).

There are several families of wavelet functions, for example; Daubechies, Meyer, Biortogonais, Haar, etc. In the realization of the present project, it will be used the Haar wavelet function (simplest of the wavelet transforms), which was proposed in 1909 by the Hungarian mathematician Alfred Haar (GAO; YAN, 2011; OPPENHEIM, 2007). The Haar transform is a particular case of the discrete wavelet transform. The Haar function is a square pulse that uses an orthonormal basis defined over the interval  $[0,1]$  (SALOMON, 2000), as described below in equation 17 and shown in Figure 8.

$$\psi_{Haar}(t) = \begin{cases} -1 & 0 \leq t < 0.5 \\ 1 & 0.5 \leq t < 1 \\ 0 & otherwise \end{cases} \quad (17)$$

Figure 8 - Haar wavelet.



Source: Santos (2014).

The wavelet transform presents an alternative for the signal processing, being able to substitute the Fourier transform. The wavelets have a number of advantages over the Fourier transform, for example, it has a simpler mathematics, being faster, and provides a precise representation of a signal as a function of time and frequency, simultaneously, besides allowing to analyze any type of signal to which the Fourier series is limited in certain occasions (STRANG, 1993; VILANI, 2011). The wavelets have been used in many areas, such as in fluid mechanics, numerical computation, image analysis, signal processing, control system, biological phenomena, medicine, and psychology. Soon, it is expected that the wavelet analysis is going to become an analysis and visualization tool as powerful as the Fourier transform.

### 3.8-Quantum theory of atoms in molecules (QTAIM)

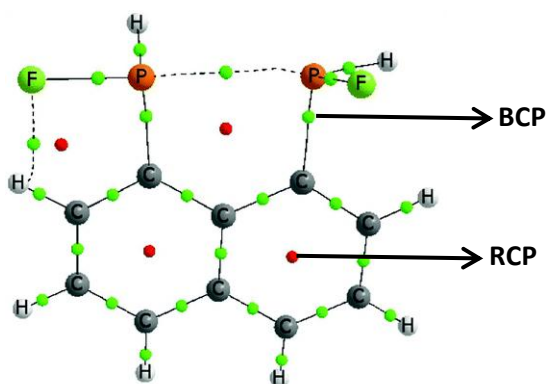
Some properties, such as electronic density ( $\rho(r)$  has played a key role in the development of chemistry. Thus, these data can provide important contributions to thermodynamic and spectroscopic properties as well (MATTA et al., 2003). In this sense, Richard Bader and his research group, at McMaster University, developed a method based on electronic structure and chemical bonds, called *Quantum Theory of Atoms in Molecules-QTAIM* (CORTESGUZMAN; BADER, 2005; MATTA et al., 2003; SOSA et al., 2002).

According to the quantum-mechanical concepts of QTAIM, the observable properties of a chemical system are contained in its molecular electronic density,  $\rho$ . The electronic density is used as a quantum-mechanical observable for the execution of numerical integrations, in which the gradient vector  $\nabla\rho$  is the basic condition for determining the molecular topology. The gradient

is perpendicular to a unit vector ( $n_{(r)}$ ) (OLIVEIRA et al., 2010).

The electronic density is shaped to describe a chemical system. These trajectories do not originate from infinity, but, instead, from a point located between two attractors, the so-called *bond critical points-BCP*. The location of BCPs is made through the laplacian of the electronic density ( $\nabla^2\rho$ ), according to equation 18. Besides BCP, there are other critical points of minimum and maximum, such as *nuclear attractor-NA-NA* and the *ring critical points-RCP*. Figure 9 shows the critical points (BCP and RCP) of bond (MATTA; BOYD, 2007; OLIVEIRA, 2010).

Figure 9 - Molecular graph showing the critical points of the bond.



Source: Sánchez (2014).

$$\nabla^2\rho = \underbrace{\frac{\delta^2\rho}{\delta x^2}}_{\lambda_1} + \underbrace{\frac{\delta^2\rho}{\delta y^2}}_{\lambda_2} + \underbrace{\frac{\delta^2\rho}{\delta z^2}}_{\lambda_3} \quad (18)$$

The laplacian fields, or the second derivatives of the electronic density, bring about vital information for the understanding of the chemical system. The Laplacian signal  $\nabla^2\rho$  has the property of describing the concentration of the electronic density in a given bond zone. For example, if  $\nabla^2\rho > 0$  (K) characterizes intra- or intermolecular interactions, while  $\nabla^2\rho < 0$  (U) describes the covalent or unsaturated bonds (hydrocarbons or hyperconjugated biological

systems). Equation 19 shows the relationship between the laplacians and kinetic energies (K) and potential (U) (BADER, 1994; OLIVEIRA, 2010; POPELIER, 2000).

$$\nabla^2\rho = 2K + U \quad (19)$$

By means of the criterion proposed by Koch and Popelier (KOCH; POPELIER, 1995), it is also possible to observe the formation of hydrogen bonds. This criterion takes into account a hydrogen atom that is not interacting with other atoms of the system. Thus, it was analyzed the atomic charge values ( $q(H)$ ), atomic volume ( $V(H)$ ), dipole moment ( $M1(H)$ ) and atomic energy ( $E(H)$ ). If there is a hydrogen bond, it should be noted a loss in the  $q(\Omega)$  values, and, as a consequence to this loss, an increase in  $E(\Omega)$  values and a decrease in the values of  $V(H)$  and  $M1(H)$  (BADER, 1994; OLIVEIRA, 2010; POPELIER, 2000).

### 3.9-Non-covalent interactions (NCI)

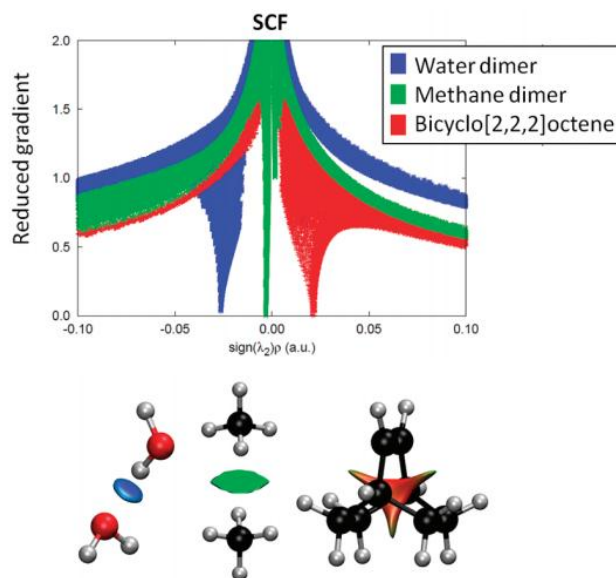
The non-covalent interactions method holds the key to understand many chemical, biological and technological problems. Introduced by Johnson and collaborators (OTERO-DE-LA-ROZA; JOHNSON; CONTRERAS-GARCÍA, 2012), the method can serve as a complement to Bader's method (QTAIM) in order to characterize, for example, weak hydrogen bonds in 3D space of five membered rings. The NCI method calculates the non-covalent interactions based on the analysis of the regions where the electron density  $\rho(r)$  and the density gradient  $s(r)$  are low, equation 20. The origin of the method can be studied through the contribution of the exchange energy gradient, from the theory of functional density (CONTRERAS-GARCÍA et al., 2011).

$$s = \frac{1}{2(3\pi^2)^{1/3}} \frac{|\nabla\rho|}{\rho^{4/3}} \quad (20)$$



The density gradient,  $\nabla\rho$ , undergoes changes according to the type of interaction among atoms, producing critical points of density between the interacting fragments, represented graphically by the appearance of depressions. The electron density values in the depressions are an indicator of the strength of the existing interactions; however, both attractive and repulsive interactions appear in the same region of reduced gradient space density. The differentiation between the two types of interaction is observed based on the second derivative of the density along the main axis of the variation ( $\nabla^2\rho$ ) (CONTRERAS-GARCÍA et al., 2011). The Laplacian indicates if the density flow is entering ( $\nabla^2\rho < 0$ ) or leaving ( $\nabla^2\rho > 0$ ) in an infinitesimal volume around a reference point, determining whether the density will be high or low in relation to its surroundings. Figure 10 shows these interactions, the hydrogen bonds are represented by the blue wedge (attractive interactions), the repulsive interactions are represented by the red wedge and the Van der Waals (VDW) interactions are represented by the green wedge.

Figure 10 - Graphical representation of the result of NCI calculations.



Fonte: CONTRERAS-GARCÍA et al., 2011

#### 4.0-Conclusion

From the above, it is possible to observe that cancer is one of the most serious problems faced by mankind, thus, the RMI technique has been used in an efficient way in detecting the same. Moreover, it is possible to conclude that the DFT method is appropriate for carrying out the present work and we see that the development of a new methodology for the selection of MD structures is of paramount importance for a more accurate QM result, thus, we present the selection method called OWSCA.

The next section will cover the results of this thesis, which will be presented in articles 1, 2, 3 and 4.

#### 5.0-Bibliographic references

ABREU, S. F. Geologia e recursos minerais da folha Casimiro de Abreu. Ministério de Minas e Energia Secretaria de Geologia, Mineração e Transformação Mineral Serviço Geológico do Brasil – CPRM, Belo Horizonte, 2012.

ACCARDO, A. et al. Supramolecular aggregates containing lipophilic Gd(III) complexes as contrast agents in MRI. **Coordination Chemistry Reviews**, Lausanne, v. 253, n. 17, p. 2193–2213, Set. 2009.

AHMAD, TANVEER; RHEE, ILSU; HONG, SUNGWOOK; CHANG, YONGMIN; LEE, J. Ni-Fe<sub>2</sub>O<sub>4</sub> Nanoparticles as Contrast Agents for Magnetic Resonance Imaging. **Journal of Nanoscience and Nanotechnology**, Valencia, v. 11, n. 7, p. 5645–5650(6), Jul, 2011.

AHMAD, M. W. et al. Potential dual imaging nanoparticle: Gd<sub>2</sub>O<sub>3</sub> nanoparticle. **Scientific Reports**, London, v. 5, p. 8549, Fev. 2015.

AL-ABADLEH, H. A. Review of the bulk and surface chemistry of iron in atmospherically relevant systems containing humic-like substances. **RSC Advances**, Cambridge, v. 5, n. 57, p. 45785–45811, Fev. 2015.

ALARCÓN, E. et al. Photophysical characterization of atorvastatin (Lipitor®) ortho-hydroxy

metabolite: role of hydroxyl group on the drug photochemistry. **Photochemical & photobiological sciences**, Cambridge, v. 9, n. 10, p. 1378–84, Out. 2010.

ALCÁCER, L. **Introdução a química quântica**. IST Press, 2007. 325 p.

ALMEIDA, K. J. **Optical and Magnetic Properties of**. School of Biotechnology, 2007.

ALMEIDA, V. L. DE et al. Câncer e agentes antineoplásicos ciclo-celular específicos e ciclo-celular não específicos que interagem com o DNA: uma introdução. **Química Nova**, Sao Paulo, v. 28, n. 1, p. 118–129, May. 2005.

APPL, M. Ammonia, 2. Production Processes. In: **Ullmann's Encyclopedia of Industrial Chemistry**. Weinheim, Germany: Wiley-VCH Verlag GmbH & Co. KGaA, 2011.

ARYANPOUR, M.; VAN DUIN, A. C. T.; KUBICKI, J. D. Development of a Reactive Force Field for Iron–Oxyhydroxide Systems. **The Journal of Physical Chemistry A**, Washington, v. 114, n. 21, p. 6298–6307, Jun. 2010.

AUGUSTUS, G.; RIBEIRO, P. As Propriedades Magnéticas da Matéria : um Primeiro Contato. **Revista Brasileira de Ensino de Física**, Salinas, v. 22, n. 3, p. 299-305, Set. 2000.

BAČIĆ, G.; PAVIĆEVIĆ, A.; PEYROT, F. In vivo evaluation of different alterations of redox status by studying pharmacokinetics of nitroxides using magnetic resonance techniques. **Redox Biology**, Amsterdam, v. 8, p. 226–242, Ago. 2016.

BAERENDS, E. J.; AUTSCHBACH, J.; BASHFORD, D.; BÉRCES, A.; BICKELHAUPT, F. M.; BO, C.; BOERRIGTER, P. M.; CAVALLO, L.; CHONG, D. P.; DENG, L. . ET AL. **ADF2009.01** The Netherlands, 2009.

BALASUBRAMANIAN, K. **Relativistic effects in chemistry – Part A**. Wiley, New York, 1997, 301 p.

BATISTA, D. R. R.; MATTOS, M. DE; SILVA, S. F. DA. Convivendo com o câncer: do diagnóstico ao tratamento. **Revista de Enfermagem da UFSM**, Santa Maria, v. 5, n. 3, p. 499–510, Out. 2015.

BOREL, A. et al. Multiexponential Electronic Spin Relaxation and Redfield's Limit in Gd(III) Complexes in Solution: Consequences for  $^{17}\text{O}$  /  $^1\text{H}$  NMR and EPR Simultaneous Analysis. **Journal of the American Chemical Society**, Washington, v. 124, n. 9, p. 2042–2048, Mar. 2002.

BORGES, M. et al. Dual  $T_1$  /  $T_2$  MRI contrast agent based on hybrid SPION @ coordination polymer nanoparticles. **RSC Advances**, Cambridge, p. 86779–86783, Out. 2015.

BOROS, E. et al. Gd(DOTAAla): a single amino acid Gd-complex as a modular tool for high relaxivity MR contrast agent development. **Journal of the American Chemical Society**, Washington, v. 134, n. 48, p. 19858–19868, Dez. 2012.

CARAVAN, P. et al. Gadolinium ( III ) Chelates as MRI Contrast Agents : Structure , Dynamics, and Applications. **Chemical Reviews**, Washington, v. 99, n. 9, p 2293–2352, Set. 1999.

CARNES, M. et al. A Stable Tetraalkyl Complex of Nickel(IV). **Angewandte Chemie**, Weinheim, v. 121, n. 19, p. 290–294, Abr. 2009.

CARVALHO, R. F. S. **Nanopartículas como potenciais agentes de contraste para imagem de ressonância magnética**: caracterização físico-química de polioxometalatos (POMs) contendo íons lantanídeos (III) e suas nanopartículas revestidas de sílica. 2011. 41 p. Dissertação (Mestrado em Bioquímica) - Universidade de Coimbra, Coimbra, 2011.

CECILIA, L. Câncer de mama e sofrimento psicológico : aspectos relacionados ao feminino breast cancer and psychological suffering : female-related aspects el cáncer de mama y el sufrimiento psicológico : aspectos. **Psicologia em Estudo**, Maringá, v. 13, n. 2, p. 231–237, Jun. 2008.

CHALA, L. F.; BARROS, N. de. Editorial avaliação das mamas com métodos de imagem. **Radiologia Brasileira**, São Paulo, v. 40, n. 1, p. 1-3, Jan. 2007.

CHAUDHURI, S.; PAHARI, B. P.; SENGUPTA, P. K. ground- and excited-state proton transfer and antioxidant activity of 7-hydroxyflavone in model membranes: absorption and fluorescence spectroscopic studies. **Biophysical Chemistry**, New York, v. 139, n. 6, p. 29-36, Jan. 2009.

CHAVHAN, G. B. et al. Principles, techniques, and applications of T2\*-based MR imaging and its special applications. **RadioGraphics**, Oak Brook, v. 29, n. 5, p. 1433–1449, Set. 2009.

CHENOWETH, K.; VAN DUIN, A. C. T.; GODDARD, W. A. ReaxFF reactive force field for molecular dynamics simulations of hydrocarbon oxidation. **The journal of physical chemistry. A**, Washington, v. 112, n. 5, p. 1040–1053, Fev. 2008.

CORTESGUZMAN, F.; BADER, R. F. W. Complementarity of QTAIM and MO theory in the study of bonding in donor-acceptor complexes. **Coordination Chemistry Reviews**, Lausanne, v. 249, n. 5–6, p. 633–662, Mar. 2005.

COSSI, M. et al. Ab initio study of solvated molecules: a new implementation of the polarizable continuum model. **Chemical Physics Letters**, Amsterdam, v. 255, n. 4–6, p. 327–335, Jun. 1996.

COUTINHO, K. et al. An efficient statistically converged average configuration for solvent effects. **Chemical Physics Letters**, Amsterdam, v. 437, n. 1-3, p. 148-152, Jan. 2007.

COUTINHO, K.; CANUTO, S. Solvent Effects from a Sequential Monte Carlo - Quantum Mechanical Approach. *Advances in Quantum Chemistry*. Amsterdam, v. 28, p. 89–105, Mar. 1997.

COUTINHO, K.; CANUTO, S.; ZERNER, M. C. Monte Carlo-quantum mechanics study of the solvatochromic shifts of the lowest transition of benzene. **Journal of Chemical Physics**, Zurich, v. 112, n. 22, p. 9874–9880, Jun. 2000.

CRAMER, C. J.; TRUHLAR, D. G. Density functional theory for transition metals and transition metal chemistry. **Physical Chemistry Chemical Physics**, Cambs, v. 11, n. 46, p. 10757–10816, Apr. 2009.

DA SILVA GONÇALVES, A. et al. Reactivation steps by 2-PAM of tabun-inhibited human acetylcholinesterase: reducing the computational cost in hybrid QM/MM methods. **Journal of Biomolecular Structure and Dynamics**, Philadelphia, v. 32, n. 2, p. 301–307, Fev. 2014.

DE ANGELIS, C.; BRIZZI, R. F.; PELLICANO, R. Endoscopic ultrasonography for pancreatic cancer: current and future perspectives. **Journal of Gastrointestinal Oncology**, Hoboken, v. 4,

n. 2, p. 220–230, Jun. 2013.

DIRAC, P. A. M. The Quantum Theory of the Electron (Part II). **Proceedings of the Royal Society of London**, London, v. 118, n. 779, p. 351–361, Mar. 1928.

DOMINGUES, M. O.; GOMES, S. M.; CORTINA, E. Biorthogonal wavelets applied to meteorological satellite images (METEOSAT) image compressing. **Wavelet Applications II DOMINGUES**, Orlando, v. 2491, p. 726-733, Abr. 1995.

DOMINGUES, M. O.; MENDES, O.; DA COSTA, A. M. On wavelet techniques in atmospheric sciences. **Advances in Space Research**, OXFORD, v. 35, n. 5, p. 831–842, Mar. 2005.

DORAZIO, S. J.; MORROW, J. R. The development of iron(II) complexes as ParaCEST MRI contrast agents. **European Journal of Inorganic Chemistry**, Washington, v. 2012, n. 12, p. 2006–2014, Abr. 2012.

DUCLA-SOARES, J. L. et al. Wavelet analysis of autonomic outflow of normal subjects on head-up tilt, cold pressor test, Valsalva manoeuvre and deep breathing. **Experimental physiology**, Malden, v. 92, n. 4, p. 677–686, Jul. 2007.

DUIN, V. **ReaxFF User Manual**, 2002.

ESTEBAN-GÓMEZ, D. et al. Hyperfine coupling constants on inner-sphere water molecules of Gd(III)-based MRI contrast agents. **Chemphyschem : a European journal of chemical physics and physical chemistry**, Weinheim, v. 13, n. 16, p. 3640–50, Nov. 2012.

FERNANDES, A. G.; MAFRA, D. Zinco e câncer: uma revisão. **Revista Saúde.Com**, Jequié, v. 1, p. 144–156, Mar. 2005.

FANTAUZZI, D; BANDLOW, J; SABO, L; MUELLER, J. E; VAN DUIN, A. C. T; JACOB, T. Development of a ReaxFF potential for Pt–O systems describing the energetics and dynamics of Pt-oxide formation, **Physical Chemistry Chemical Physics**, Cambridge, v. 16, p. 23118-23133, Jul. 2014.

FERREIRA, C. S. D. O. **Estudos de Modelação Molecular e de Ressonância Magnética**

**Nuclear de Complexos de Inclusão entre Ciclodextrinas e Poliazamacrocíclós de Gadolínio ( III ).** 2001. Dissertação (Mestrado em Química) - Faculdade de Ciências da Universidade do Porto, Porto, 2011.

FLAMENT, J. et al. In vivo CEST MR imaging of U87 mice brain tumor angiogenesis using targeted LipoCEST contrast agent at 7 T. **Magnetic resonance in medicine : official journal of the Society of Magnetic Resonance in Medicine / Society of Magnetic Resonance in Medicine**, Hoboken, v. 69, n. 1, p. 179–87, Jan. 2013.

FRATILA, R. M. et al. Shape matters: synthesis and biomedical applications of high aspect ratio magnetic nanomaterials. **Nanoscale**, Cambridge, v.7, n. 1, p. 8233–8260, Fev. 2015.

GALDINO, B. et al. Uma comprovação químico-quântica sobre a formação de ligações de hidrogênio e interações secundárias em sistemas heterocíclicos intermoleculares. **Orbital**, Santa Maria, v. 1, n. 2, p. 167–182, Mar. 2009.

GAO, D. et al. Compact chelator-free Ni-integrated CuS nanoparticles with tunable near-infrared absorption and enhanced relaxivity for in vivo dual-modal photoacoustic/MR imaging. **Nanoscale**, Cambridge, v. 7, n. 42, p. 17631–6, Nov. 2015.

GAO, R. X.; YAN, R. **From Fourier Transform to Wavelet Transform: A Historical Perspective**. Boston, MA: Springer US, 2011. p. 17–32.

GERALDES, C. F. G. C.; LAURENT, S. Classification and basic properties of contrast agents for magnetic resonance imaging. **Contrast media & molecular imaging**, Hoboken, v. 4, n. 1, p. 1–23, Jan. 2009.

GHOSE, S. K. et al. Hydrated goethite ( $\alpha$ -FeOOH) (100) interface structure: Ordered water and surface functional groups. **Geochimica et Cosmochimica Acta**, Amsterdam, v. 74, n. 7, p. 1943–1953, Dec. 2010.

GODBOUT, N. et al. Optimization of Gaussian-type basis sets for local spin density functional calculations. Part I. Boron through neon, optimization technique and validation. **Canadian Journal of Chemistry**, Toronto, v. 70, n. 2, p. 560–571, Set. 1992.

GONÇALVES, M. A. et al. Dynamics, NMR parameters and hyperfine coupling constants of the Fe<sub>3</sub>O<sub>4</sub>(100)–water interface: Implications for MRI probes. **Chemical Physics Letters**, Amsterdam, v. 609, p. 88–92, Ago. 2014.

GONÇALVES, M. A. et al. Probing thermal and solvent effects on hyperfine interactions and spin relaxation rate of  $\delta$ -FeOOH(100) and [MnH<sub>3</sub>buea(OH)]<sub>2</sub><sup>-</sup>: Toward new MRI probes. **Computational and Theoretical Chemistry**, Amsterdam, v. 1069, p. 96–104, Out. 2015.

GONÇALVES, M. A. et al. Optimal wavelet signal compression as an efficient alternative to investigate molecular dynamics simulations: application to thermal and solvent effects of MRI probes. **Theoretical Chemistry Accounts**, New York, v. 136, n. 1, p. 15, Jan. 2017.

GORDON, W. Der Comptoneffekt nach der Schrödingerschen Theorie, **Zeitschrift für Physik**, Berlin, v. 40, n. 3, p. 117–133, Set.1926.

GRABOWSKI, S. J. What is the covalency of hydrogen bonding? **Chemical reviews**, Euskadi, v. 111, n. 1-2, p. 2597–625, Abr. 2011.

GRAHAM E. JACKSON , MICHAEL J. BYRNE , GERRY BLEKKENHORST, A. J. H. Chromium - cage complex as contrast agent in MR imaging—Biodistribution studies of the [57Co] cobalt analogue. **International Journal of Radiation Applications and Instrumentation. Part B. Nuclear Medicine and Biology**, Oxford, v. 18, n. 8, p. 855–858, Fev. 1991.

GRAU-CRESPO, R. et al. Vacancy ordering and electronic structure of  $\gamma$ -Fe<sub>2</sub>O<sub>3</sub> (maghemite): a theoretical investigation. **Journal of physics. Condensed matter : an Institute of Physics journal**, Bristol, v. 22, n. 25, p. 255401, Jun. 2010.

GUPTA, R. et al. Characterization of Monomeric Mn-II/III/IV-Hydroxo Complexes from X- and Q-Band Dual Mode Electron Paramagnetic Resonance (EPR) Spectroscopy. **Inorganic Chemistry**, Washington, v. 52, n. 21, p. 12568-12575, Out. 2013.

GUPTA, R.; BOROVNIK, A. S. Monomeric MnIII/II and FeIII/II Complexes with Terminal Hydroxo and Oxo Ligands: Probing Reactivity via O-H Bond Dissociation Energies. **Journal of**



**the American Chemical Society**, Washington, v. 125, n. 43, p. 13234–13242, Oct. 2003.

HAN, L.; ZHOU, X. Synthesis and characterization of liposomes nano-composite-particles with hydrophobic magnetite as a MRI probe. **Applied Surface Science**, Amsterdam, v. 376, n. 1, p. 252–260, Jul. 2016.

HANESCH, M. Raman spectroscopy of iron oxides and (oxy)hydroxides at low laser power and possible applications in environmental magnetic studies. **Geophysical Journal International**, Malden, v. 177, n. 3, p. 941–948, Jun. 2009.

HARIBABU, V. et al. Optimized Mn-doped iron oxide nanoparticles entrapped in dendrimer for dual contrasting role in MRI. **Journal of Biomedical Materials Research Part B: Applied Biomaterials**, Hoboken, v. 104, n. 4, p. 817–824, May. 2016.

HARRIS, D.; LOEW, G. H.; KOMORNICKI, A. Structure and Relative Spin-State Energetics of  $[\text{Fe}(\text{H}_2\text{O})_6]^{3+}$ : A Comparison of UHF, Møller–Plesset, Nonlocal DFT, and Semiempirical INDO/S Calculations. **The Journal of Physical Chemistry A**, Washington, v. 101, n. 21, p. 3959–3965, May. 1997.

HEDEGA, E. D.; KONGSTED, J.; SAUER, S. P. A. Validating and analyzing EPR hyperfine coupling constants with density functional theory. **Journal of Chemical Theory and Computation**, Copenhagen, v. 9, n. 5, p. 2380–2388, Apr. 2013.

HEDEGÅRD, E. D.; KONGSTED, J.; SAUER, S. P. A. Optimized Basis Sets for Calculation of Electron Paramagnetic Resonance Hyperfine Coupling Constants: aug-cc-pVTZ-J for the 3d Atoms Sc–Zn. **Journal of Chemical Theory and Computation**, Copenhagen, v. 7, n. 12, p. 4077–4087, Dez. 2011.

HEDEGÅRD, E. D.; KONGSTED, J.; SAUER, S. P. A. Improving the calculation of electron paramagnetic resonance hyperfine coupling tensors for d-block metals. **Physical Chemistry Chemical Physics**, Cambs, v. 14, n. 30, p. 10669, Aug. 2012.

HOCAOGLU, I. et al. Cyto/hemocompatible magnetic hybrid nanoparticles ( $\text{Ag}_2\text{S}-\text{Fe}_3\text{O}_4$ ) with luminescence in the near-infrared region as promising theranostic materials. **Colloids and**

**Surfaces B: Biointerfaces**, Amsterdam, v. 133, p. 198–207, Set. 2015.

HUANG, C.-H.; TSOURKAS, A. Gd-based macromolecules and nanoparticles as magnetic resonance contrast agents for molecular imaging. **Current topics in medicinal chemistry**, Sharjah v. 13, n. 4, p. 411–421, Fev. 2013.

JENSEN, F. **Introduction to Computational Chemistry**. Wiley, 1999, 660 p.

JIN, M. et al. Hydroxy double salts intercalated with Mn(II) complexes as potential contrast agents. **Solid State Sciences**, Amsterdam, v. 53, p. 9–16, Mar. 2016.

JØRGENSEN, J.-E. et al. Formation of  $\gamma$ -Fe<sub>2</sub>O<sub>3</sub> nanoparticles and vacancy ordering: An in situ X-ray powder diffraction study. **Journal of Solid State Chemistry**, Amsterdam, v. 180, n. 1, p. 180–185, Jan. 2007.

DUARTE, J. A.; FURTADO, A. P.; MARRONI, C.A. Use of pineapple juice with gadopentetate dimeglumine as a negative oral contrast for magnetic resonance cholangiopancreatography: a multicentric study. **Abdominal Imaging**, New York, v. 37, n. 3, p. 447–456, Jun. 2011.

JUNG, H. et al. Dual MRI T1 and T2(\*) contrast with size-controlled iron oxide nanoparticles. **Nanomedicine: Nanotechnology, Biology, and Medicine**, Amsterdam, v. 10, n. 8, p. 1679–1689, May. 2014.

KAMADA, M. et al. Analysis of motion features for molecular dynamics simulation of proteins. **Chemical Physics Letters**, Amsterdam, v. 502, n. 4-6, p. 241–247, Jan. 2011.

KHOSROSHAHI, M. E. et al. Evaluation of cell viability and T2 relaxivity of fluorescein conjugated SPION-PAMAM third generation nanodendrimers for bioimaging. **Materials science & engineering. C, Materials for biological applications**, Amsterdam, v. 62, p. 544–552, May. 2016.

KLUG, G. et al. Intracellular and extracellular T1 and T2 relaxivities of magneto-optical nanoparticles at experimental high fields. **Magnetic Resonance in Medicine**, Hoboken, v. 64, n. 6, p. 1607–1615, Dez. 2010.

KOCH, U.; POPELIER, P. L. A. Characterization of C-H-O Hydrogen Bonds on the Basis of the Charge Density. **The Journal of Physical Chemistry**, Washington, v. 99, n.24, p. 9747–9754, Jun. 1995.

KORETSKY, A. P.; SILVA, A. C. Manganese-enhanced magnetic resonance imaging (MEMRI). **NMR in biomedicine**, Berlin, v. 17, n. 8, p. 527–31, Dez. 2004.

LASOROSKI, A.; VUILLEUMIER, R.; POLLET, R. Hyperfine interactions in a gadolinium-based MRI contrast agent: high-frequency modulations from ab initio simulations. **The Journal of chemical physics**, Zurich, v. 139, n. 10, p. 104115, Set. 2013.

LEE, Y. C. et al. The Use of Silica Coated MnO Nanoparticles to Control MRI Relaxivity in Response to Specific Physiological Changes. **Biomaterials**, Daegu, v. 33, n. 13, p. 3560–3567, May. 2012.

LEPAGE, M.; GORE, J. C. Contrast mechanisms in magnetic resonance imaging. **Journal of Physics: Conference Series**, Sherbrooke, v. 3, p. 78–86, Jan. 2004.

LEWARS, E. G. **Computational Chemistry**. Springer, 2011, 664 p.

LI, Y. et al. Gd-complex labeled magnetite nanoparticles as fluorescent and targeted magnetic resonance imaging contrast agent. **Materials Letters**, Amsterdam, v. 98, p. 34–37, May. 2013.

LI, J. Y. ET AL. A highly specific tetrazole-based chemosensor for fluoride ion: a new sensing functional group based on intramolecular proton transfer. **Spectrochimica Acta Part A: Molecular and Biomolecular Spectroscopy**, Nanjing, v. 102, p. 66–70, Fev. 2013.

LITTER, M. I.; BLESA, M. A. Photodissolution of iron oxides. IV. A comparative study on the photodissolution of hematite, magnetite, and maghemite in EDTA media. **Canadian Journal of Chemistry**, Toronto, v. 70, n. 9, p. 2502–2510, Set. 1992.

MCROBBIE, D.W. et. al. **MRI from Picture to Proton**. Cambridge University Press, 2017. 400 p.

MANCINI, D. T. et al. <sup>99</sup>Tc NMR as a promising technique for structural investigation of

biomolecules: theoretical studies on the solvent and thermal effects of phenylbenzothiazole complex. **Magnetic resonance in chemistry : MRC**, Hoboken, v. 52, n. 4, p. 129–37, Abr. 2014.

MANCINI, D. T. et al. Excited-State Proton Transfer Can Tune the Color of Protein Fluorescent Markers. **Chemphyschem : a European journal of chemical physics and physical chemistry**, Weinheim, v. 16, n. 16, p. 3444–3449, Nov. 2015.

MARTIN KAUPP, MICHAEL BÜHL, V. G. M. **Calculation of NMR and EPR Parameters: Theory and Applications**. Wiley, 1999, 661 p.

MARTINS, T. S. et al. Terras raras: aplicações industriais e biológicas. São Paulo, v. 28, n. 1, p. 111–117, Nov. 2005.

**MATLAB 7.6 and Statistics Toolbox**. Massachusetts, 2007.

MATTA, C. F.; BOYD, R. J. **The quantum theory of atoms in molecules: from solid state to DNA and drug design**. London: Wiley, 2007. 524 p.

MATTA, C. F. et al. Hydrogen-hydrogen bonding: a stabilizing interaction in molecules and crystals. **Chemistry-A EUROPEAN JOURNAL**, Weinheim, v. 9, n. 9, p. 1940–51, May. 2003.

MAZZOLA, A. A. Ressonância magnética : princípios de formação da imagem e aplicações em imagem funcional Magnetic resonance : principles of image formation and applications in funcional imaging. **Revista Brasileira de Física Médica**, Natal, v. 3, n. 1, p. 117–129, Mar. 2009.

MESQUITA, A. M. et al. Boron as a promoter in the goethite ( $\alpha$ -FeOOH) phase: Organic compound degradation by Fenton reaction. **Applied Catalysis B: Environmental**, Amsterdam, v. 192, p. 286–295, Set. 2016.

MITCHELL, M. **An Introduction to Genetic Algorithms**. The MIT Press, 1998 p. 209.

MOLAR, M. Ferro. **Química Nova na Escola**, Sao Paulo, v. 32, n. 3, p. 2008–2010, Mar. 2010.

MORGON, N.H; CUSTODIO, R. Teoria do Funcional de Densidade. **Química Nova**, Sao Paulo v. 18, n. 1, p. 44–55, Jul. 1994.

NAMBA, A. M.; SILVA, V. B.; SILVA, C. H. T. P. Dinâmica molecular : teoria e aplicações em planejamento de fármacos. **Eclética Química**, São Paulo, v. 33, n. 4, p. 13–23, Out. 2008.

NBTS- National Brain Tumor Society, 2018. Disponível em:

< <http://braintumor.org>>, acesso: 06 de outubro de 2018.

NEWQUIST, H. **The Human Body: The Story of How We Protect, Repair, and Make Ourselves Stronger (Smithsonian: Invention & Impact)**, Hardcover, 2015, 112 p.

NOGUEIRA-BARBOSA, H.; MUGLIA, V. F. Complicações do uso intravenoso de agentes de contraste à base de gadolínio para ressonância magnética \* for magnetic resonance imaging. **Radiologia Brasileira**, v. 41, n. 4, p. 263–267, Jul. 2008.

OLATUNDE, A. O. et al. The NiCEST approach: nickel(II) paraCEST MRI contrast agents. **Journal of the American Chemical Society**, Washington, v. 134, n. 45, p. 18503–1805, Nov. 2012.

OLIVEIRA, B. G. et al. A Topologia molecular qtaim e a descrição mecânico-quântica de ligações de hidrogênio e ligações de di-hidrogênio. **Química Nova**, Sao Paulo, v. 33, n. 5, p. 1155–1162, Abr. 2010.

OLIVEIRA, I. S.; GUIMARÃES, A. P. Introdução as Interações Hiperfinas em Ions Livres. São Paulo, v. 22, n. 3, p. 353-359, Set. 2000.

OLIVEIRA, LUIZ C A; FABRIS, J D; PEREIRA, M. C. Óxidos de ferro e suas aplicações em processos catalíticos: uma revisão Luiz. **Química Nova**, Sao Paulo, v. 36, n. 1, p. 123–130, Nov. 2012.

OLIVEIRA, L. C. **Estudos dosimétricos da hidroxiapatita por ressonância paramagnética eletrônica e termoluminescência**. 2010. 109 p. Tese (Doutorado em Física Aplicada à Medicina e Biologia) - Universidade de São Paulo, Ribeirão Preto, 2010.

OLIVEIRA, L. C. A. et al. Pure niobia as catalyst for the oxidation of organic contaminants: Mechanism study via ESI-MS and theoretical calculations. **Chemical Physics Letters**, Amsterdam, v. 446, n. 1-3, p. 133–137, Set. 2007.

OPPENHEIM, G. **Wavelets and Their Applications**. Wiley, 2007. 330 p.

ORGANUM, P.; LDA, T. Teoria do funcional da densidade Uma Possível Solução para o Problema de Muitos Elétrons da Mecânica Quântica. **Physicae Organum** v. 2, n. 1, p. 1-14, Mar. 2016.

PANKHURST, Q. A. et al. Applications of magnetic nanoparticles in biomedicine. **Journal of Physics D: Applied Physics**, Bristol, v. 36, n. 13, p. R167–R181, Jul. 2003.

PATINEC, V. et al. Hyperfine coupling constants on inner-sphere water molecules of a triazacyclononane-based Mn(II) complex and related systems relevant as MRI contrast agents. **Inorganic Chemistry**, Washington, v. 52, n. 19, p. 11173–11184, Oct. 2013.

PERAZELLA, M. A. Current status of gadolinium toxicity in patients with kidney disease. **Clinical journal of the American Society of Nephrology : CJASN**, v. 4, n. 2, p. 461–469, Abr. 2009.

PLIEGO, J. R. Modelos Contínuos Do Solvente: Fundamentos. **Química Nova**, Sao Paulo, v. 29, n. 3, p. 535–542, Fev. 2006.

POWELL, D. H. et al. Structural and Dynamic Parameters Obtained from  $^{17}\text{O}$  NMR, EPR, and NMRD Studies of Monomeric and Dimeric  $\text{Gd}^{3+}$  Complexes of Interest in Magnetic Resonance Imaging: An Integrated and Theoretically Self-Consistent Approach. **Journal of the American Chemical Society**, v. 7863, n. 3, p. 9333–9346, Oct. 1996.

PRESS, D. Nanoparticles in magnetic resonance imaging: from simple to dual contrast agents. **International journal of nanomedicine**, Albany, v.10, p. 1727–1741, Jun. 2015.

RAMALHO, T. C.; CUNHA, E. F. F. DA; ALENCASTRO, R. B. DE. Solvent effects on  $^{13}\text{C}$  and  $^{15}\text{N}$  shielding tensors of nitroimidazoles in the condensed phase: a sequential molecular dynamics/quantum mechanics study. **Journal of physics. Condensed matter : an Institute of Physics journal**, Bristol, v. 16, n. 34, p. 6159–6170, Set. 2004.

RAMALHO, T. C.; DA CUNHA, E. F. F.; DE ALENCASTRO, R. B. Theoretical Study of Adiabatic and Vertical Electron Affinity of Radiosensitizers in Solution Part 2: Analogues of

Tirapazamine. **Journal of Theoretical and Computational Chemistry**, Singapore, v. 3, n. 1, p. 1–13, Mar. 2004.

RAMALHO, T. C.; PEREIRA, D. H.; THIEL, W. Thermal and Solvent Effects On NMR Indirect Spin–Spin Coupling Constants of a Prototypical Chagas Disease Drug. **The Journal of Physical Chemistry A**, Washington, v. 115, n. 46, p. 13504–13512, Nov, 2011.

RAYMOND K N;PIERRE, V. C. Raymond K.Next generation, high relaxivity gadolinium MRI agents, **Bioconjugate Chemistry**, Washington, v. 16, n. 1, p. 3-8, Fev. 2005.

RODRÍGUEZ-RODRÍGUEZ, A. et al. Solution structure of Ln(III) complexes with macrocyclic ligands through theoretical evaluation of <sup>1</sup>H NMR contact shifts. **Inorganic chemistry**, Washington, v. 51, n. 24, p. 13419–13429, Dez. 2012.

ROJAS, J. M. et al. Superparamagnetic iron oxide nanoparticle uptake alters M2 macrophage phenotype, iron metabolism, migration and invasion. **Nanomedicine : nanotechnology, biology, and medicine**, Amsterdam, v. 12, n. 4, p. 1127–1138, May. 2016.

ROUX, B.; SIMONSON, T. Implicit solvent models. **Biophysical Chemistry**, New York, v. 78, n. 1-2, p. 1–20, Abr. 1999.

RUIZ, E.; CIRERA, J.; ALVAREZ, S. Spin density distribution in transition metal complexes. **Coordination Chemistry Reviews**, Lausanne, v. 249, n. 23, p. 2649–2660, Dec. 2005.

SALOMON,D; MOTTA, G. Handbook of Data Compression. 5<sup>th</sup>. ed. [S.I]:Springer Publishing Company, Incorporated, 2009.

SANTOS, L. DE S. **OTIMIZAÇÃO DINÂMICA USANDO APROXIMAÇÃO COM BASE WAVELETS ADAPTATIVA**. 2014. 197 p. Tese (Doutorado em Engenharia Química)-Universidade Federal do Rio de Janeiro, Rio de Janeiro, 2014.

SCHRODER, P. Wavelets for computer graphics: a primer.1. **IEEE Computer Graphics and Applications**, New York, v. 15, n. 3, p. 76–84, May. 1995.

SCHWARZ, S. et al. Synthetic and biogenic magnetite nanoparticles for tracking of stem cells

and dendritic cells. **Journal of Magnetism and Magnetic Materials**, Amsterdam, v. 321, n. 10, p. 1533–1538, May. 2009.

SIMPSON, A. W. Some superparamagnetic properties of fine particles  $\delta$ -FeOOH. **Journal of Applied Physics**, Ann Arbor, v. 33, n. 3, p. 1203–1206, May. 1962.

SOSA, G. L. et al. Topological and NBO analysis of hydrogen bonding interactions involving C–H $\cdots$ O bonds. **Journal of Molecular Structure: THEOCHEM**, Amsterdam, v. 577, n. 2-3, p. 219–228, Jan. 2002.

STEPHEN, Z. R.; KIEVIT, F. M.; ZHANG, M. Magnetite Nanoparticles for Medical MR Imaging. **National Institutes of Health**, Washington, v. 14, n. 11, p. 330–338, Jul. 2011.

STRANG, G. Wavelet transforms versus fourier transforms. **Bulletin (New Series) of the American Mathematical Society**, New York, v. 28, n. 2, p. 288–305, Abr.1993.

STRIJKERS, G. J. et al. MRI contrast agents: current status and future perspectives. **Anti-Cancer Agents in Medicinal Chemistry**, Eindhoven, v. 7, n. 3, p. 291-305, May. 2007.

SUN, C.; LEE, J. S. H.; ZHANG, M. Magnetic nanoparticles in MR imaging and drug delivery. **Advanced Drug Delivery Reviews**, Amsterdam, v. 60, n. 11, p. 1252–1265, Aug. 2008.

TACHIKAWA, H. Ab initio molecular dynamics (MD) calculations of hyperfine coupling constants of methyl radical. **Chemical Physics Letters**, Amsterdam, v. 352, n. 1-2, p. 113–119, Out. 2002.

TELEGRAFO, M. et al. Unenhanced breast MRI (STIR, T2-weighted TSE, DWIBS): An accurate and alternative strategy for detecting and differentiating breast lesions. **Magnetic Resonance Imaging**, New York, v. 33, n. 8, p. 951–955, Out. 2015.

TOMASI, J.; MENNUCCI, B.; CANCÈS, E. The IEF version of the PCM solvation method: an overview of a new method addressed to study molecular solutes at the QM ab initio level. **Journal of Molecular Structure (Theochem)**, Amsterdam, v. 464, p. 211–226, May. 1999.

TSAI, Z.-T. et al. In situ preparation of high relaxivity iron oxide nanoparticles by coating with



chitosan: A potential MRI contrast agent useful for cell tracking. **Journal of Magnetism and Magnetic Materials**, Amsterdam, v. 322, n. 2, p. 208–213, Jan. 2010.

UMUT, E. et al. Magnetic, optical and relaxometric properties of organically coated gold–magnetite (Au–Fe<sub>3</sub>O<sub>4</sub>) hybrid nanoparticles for potential use in biomedical applications. **Journal of Magnetism and Magnetic Materials**, Amsterdam, v. 324, n. 15, p. 2373–2379, Ago. 2012.

VAN DER WIJST, T. et al. Rare Tautomers of 1-Methyluracil and 1-Methylthymine: Tuning Relative Stabilities through Coordination to Pt II Complexes. **Chemistry - A European Journal**, Weinheim, v. 15, n. 1, p. 209–218, Jan. 2009.

VAN DUIN, A. C. T. et al. ReaxFF: A Reactive Force Field for Hydrocarbons. **The Journal of Physical Chemistry A**, Washington, v. 105, n. 41, p. 9396–9409, Set. 2001.

VILANI, M. T. Análise de fourier e wavelet em variáveis micrometeorológicas em diferentes tipologias de ocupação. **Revista Brasileira de Engenharia Agrícola e Ambiental**, Campina Grande, v.17, n. 12, p. 1340–1346, Dez. 2011.

VILLA, A; STOCK, G. What NMR Relaxation Can Tell Us about the Internal Motion of an RNA Hairpin: A Molecular Dynamics Simulation Study. **Journal of Chemical Theory and Computation**, Copenhagen, v. 2, n. 5, p. 1228-1236. May. 2006.

WERNER, E. J. et al. High-relaxivity MRI contrast agents: where coordination chemistry meets medical imaging. **Angewandte Chemie (International ed. in English)**, Weinheim, v. 47, n. 45, p. 8568–80, Jan. 2008.

XU, F. et al. Magnetite Nanocrystal Clusters with Ultra-High Sensitivity in Magnetic Resonance Imaging. **Chemphyschem : a European journal of chemical physics and physical chemistry**, Weinheim, v. 13, n. 1, p. 336–341, Jan. 2012.

YAZYEV, O. V; HELM, L. Gadolinium (III) ion in liquid water: structure, dynamics, and magnetic interactions from first principles. **The Journal of chemical physics**, Zurich, v. 127, n. 8, p. 84506, Ago. 2007.

YOFFE, S. et al. Superparamagnetic Iron Oxide Nanoparticles (SPIONs): Synthesis and Surface

Modification Techniques for use with MRI and Other Biomedical Applications. **Current Pharmaceutical Design**, Sharjah, v. 19, n. 1-2, p. 493–509, Jan. 2013.

ZHANG, Y. et al. Synergistic Effect of Human Serum Albumin and Fullerene on Gd-DO3A for Tumor-Targeting Imaging. **ACS Applied Materials & Interfaces**, Washington, v. 8, n. 18, p. 11246–11254, May. 2016.

ZIENER, C. H. et al. Structure-specific magnetic field inhomogeneities and its effect on the correlation time. **Magnetic resonance imaging**, New York, v. 24, n. 10, p. 1341–7, Dez. 2006.

## **SECOND PART-ARTICLES**

**Article 1-Agentes de Contraste para Ressonância Magnética de Imagem: Uma revisão**

**(article published in *Revista Virtual de Química-RVq*)**

## **Agentes de Contraste para Ressonância Magnética de Imagem: Uma revisão**

### **Abstract:**

The Magnetic Resonance Imaging (MRI) is a noninvasive technique based on the magnetic properties of the  $^1\text{H}$  and  $^{17}\text{O}$  atoms. Currently, about 30% of MRI exams use paramagnetic compounds, which are defined as contrast agents (CAs), able to reduce the relaxation times ( $T_1$  and  $T_2$ ) of  $^1\text{H}$  and  $^{17}\text{O}$  atoms of water molecules. In this review, we show the main compounds employed as CAs. Among these,  $\text{Gd}^{3+}$  complexes are frequently used, but problems related to their high toxicity, promoting the development of new ACs, such as iron oxides, hybrid compounds as well as  $\text{Mn}^{2+}$  and  $\text{Ni}^{2+}$  complexes, which are less toxic and more effective.

### **Resumo:**

A Ressonância Magnética de Imagem (RMI) é uma técnica não invasiva baseada nas propriedades magnéticas dos átomos de  $^1\text{H}$  e  $^{17}\text{O}$ . Atualmente, cerca de 30% dos exames de RMI utilizam compostos paramagnéticos capazes de reduzir os tempos de relaxação ( $T_1$  e  $T_2$ ) dos átomos de  $^1\text{H}$  e  $^{17}\text{O}$  das moléculas de água, que são definidos como agentes de contrastes (ACs). Nesta revisão, mostramos os principais compostos utilizados como ACs. Entre eles, complexo de  $\text{Gd}^{3+}$  são frequentemente utilizados, mas os problemas relacionados com a sua elevada toxicidade, promoveu o desenvolvimento de novos ACs, tais como óxidos de ferro, compostos híbridos, bem como complexos de  $\text{Mn}^{2+}$  e  $\text{Ni}^{2+}$  que são menos tóxicos e mais eficazes.

## 1.0-Introdução:

Esta revisão tem como objetivo explorar os principais compostos usados como agentes de contraste (ACs) e mostrar suas respectivas aplicabilidades, tais como sondas para Ressonância Magnética de Imagem (RMI). A RMI é uma técnica baseada nos princípios da Ressonância Magnética Nuclear (RMN), em que as imagens são geradas através da codificação do sinal de RMN, especialmente os sinais vindos dos núcleos de hidrogênio<sup>1</sup>. Atualmente, a RMI é um método de diagnóstico por imagem estabelecido na prática clínica. Dada a alta capacidade de diferenciar tecidos, o espectro de aplicações se estende a todas as partes do corpo humano, explorando aspectos anatômicos e funcionais<sup>2</sup>, a primeira visualização do corpo humano através da RMI ocorreu em 1977<sup>3</sup>. Essa técnica de diagnóstico é não invasiva e baseada nas propriedades magnéticas dos núcleos de <sup>1</sup>H e <sup>17</sup>O, pois, a elevada concentração de água existente em sistemas biológicos faz com que estes sejam os átomos mais abundantes no corpo humano<sup>2</sup>.

Nas últimas décadas, a RMI surgiu como uma poderosa ferramenta de diagnóstico que utiliza os tempos de relaxação longitudinal ( $T_1$ ) e transversal ( $T_2$ ) dos hidrogênios da água para obter imagens dos tecidos. O valor de  $T_1$  está relacionado ao tempo de retorno da magnetização para o eixo longitudinal e é influenciada pela interação dos spins com a rede (ambiente)<sup>1</sup>. Já o valor de  $T_2$  faz referência à redução da magnetização no plano transversal e é influenciada pela interação spin-spin (dipolo-dipolo)<sup>2</sup>, existe também uma defasagem dos momentos magnéticos, aumentando ainda mais a relaxação no plano transversal e acelerando o decaimento do sinal de indução livre, assim, temos um outro tempo de relaxação definido como  $T_2^*$ <sup>4</sup>. As equações 1 e 2 mostram os tempos de relaxação. O tempo de relaxação longitudinal ( $T_1$ ) depende do spin eletrônico total do íon metálico ( $S$ ), dos fatores eletrônicos do elétron livre e do núcleo ( $g_e$  e  $g_N$ , respectivamente), do magnéton de Bohr e nuclear ( $\beta$  e  $\beta_N$ , respectivamente), da constante de acoplamento hiperfino ( $A$ ), da distância entre o próton e o íon metálico ( $r$ ), da frequência de Larmor para o próton girar ( $\omega_I$ ) e do tempo de correlação ( $\tau_e$ ), que caracteriza o tempo de correlação rotacional interno das moléculas. Para o tempo de relaxação transversal ( $T_2$ ),  $\omega_S$  é a frequência de Larmor para o elétron girar e  $\tau_C$  é o tempo de correlação caracterizado pela taxa de variação das interações dos íons entre o metal e os hidrogênios vizinhos,  $\tau_C$  é o tempo de correlação rotacional total da molécula, as outras constantes da equação 2 já foram mencionadas acima.

Equação 1:

$$R_1 = \frac{1}{T_1} \cong \frac{1}{15} \frac{S(S+1)g^2\beta^2g_N^2\beta_N^2}{\hbar^2r^6} + \left(\frac{A}{\hbar}\right)^2 \frac{S(S+1)}{3} \left[ \frac{2\tau_e}{1 + (\omega_I\tau_e)^2} \right]$$

Equação 2:

$$R_2 = \frac{1}{T_2} \cong \frac{1}{15} \frac{S(S+1)g_e^2\beta^2g_N^2\beta_N^2}{\hbar^2r^6} + \left(\frac{A}{\hbar}\right)^2 \frac{S(S+1)}{3} \left[ \tau_c + \frac{\tau_c}{1 + (\omega_S\tau_e)^2} \right]$$

Pela equação 1 e 2, a constante de acoplamento hiperfino (A) é a variável mais sensível. Os parâmetros de A descrevem as interações dos elétrons desemparelhados com núcleos magnéticos. Essas interações são caracterizadas pelo acoplamento isotrópico ( $A_{iso}$ ), representado pelo Contato de Fermi (FC), e estão relacionados com as densidades de spin dos núcleos, representados pela equação 3<sup>5,6</sup>.

Equação 3:

$$A_{iso} = \frac{4\pi}{3} \beta_e\beta_N g_e g_N \langle S_Z \rangle^{-1} \rho_N^{\alpha-\beta}$$

em que  $\beta_e$  é o magnéton de Bohr,  $\beta_N$  é o magnéton nuclear,  $g_e$  é o fator eletrônico do elétron livre (valor igual a 2,00231931),  $g_N$  é o valor do núcleo,  $\langle S_Z \rangle$  é o valor esperado da componente z do spin eletrônico global e  $\rho_N^{\alpha-\beta}$  é a densidade de rotação na posição do núcleo  $N^6$ .

O ganho de massa dos elétrons internos em átomos mais pesados fazem com que seus orbitais internos se contraem expandindo assim seus orbitais de valência (orbitais d e f), fazendo com que estes tenham uma energia e sejam mais reativos. Entretanto, para elementos pesados, esses efeitos podem influenciar significativamente muitas propriedades físicas e químicas, então para levar em consideração essa correção, efeitos relativísticos são utilizados<sup>7</sup>. Historicamente, os efeitos relativísticos na mecânica quântica tiveram seus primeiros passos com Schrödinger por meio da teoria da relatividade proposta por Einstein em 1905<sup>8,9</sup>, a teoria foi melhorada em 1928

por Dirac<sup>10</sup>. Sabe-se que os efeitos relativísticos se tornam mais aparentes na medida em que a velocidade das partículas se aproxima da velocidade da luz, o que ocorre com os elétrons mais internos em átomos pesados. Assim, os efeitos relativísticos são importantes para os orbitais mais próximos ao núcleo, que irá, por sua vez, induzir efeitos indiretos sobre orbitais de valência. Além disso, uma vez que os efeitos relativísticos melhoram a descrição dos orbitais *s* e *p*, eles também dilatam significativamente os orbitais de valência *d* e *f*<sup>7</sup>. Portanto, os efeitos relativísticos são importantes para átomos com um volume atômico grande.

Para os cálculos sem efeitos relativísticos, a constante de acoplamento hiperfino é dada por duas contribuições, como mostra a Equação 4<sup>11</sup>.

Equação 4:

$$A = A_{iso} + A_{SD}$$

Em que  $A_{iso}$  representa o contato isotrópico e o  $A_{SD}$  representa o contato anisotrópico. Pela Equação 4, a parte isotrópica pode ser determinada em ensaios realizados em fase gasosa e em solução, como já mostrado na equação 3, que é determinado pelo Contato de Fermi (FC). Os componentes anisotrópicos só são significativos em amostras ordenadas em que as moléculas são orientadas pelo campo externo estático, portanto, geralmente, o contanto anisotrópico é igual a zero. Assim, pode-se representar a Equação 4 de forma mais simples,  $A_{iso}=A_{FC}$ . Além da contribuição do Contato de Fermi, para os efeitos relativísticos, se faz necessário considerar a rotação spin-órbita introduzida a um prazo adicional conhecido como “pseudocontato” (PC). Essa contribuição é mostrada na Equação 5<sup>11,12</sup>.

Equação 5:

$$A_{iso} = A_{FC} + A_{PC}$$

Na maioria dos exames de RMI apenas com a relaxação natural dos hidrogênios da água não é possível obter imagens claras dos tecidos<sup>13</sup>. Assim, para se ter imagens mais claras é necessário o uso de Agentes de Contraste (ACs), que são compostos paramagnéticos capazes de diminuir os tempos de relaxação  $T_1$  e  $T_2$  dos hidrogênios da água presentes nos tecidos, atualmente, certa de 30% dos exames de RMI incluem o uso de ACs<sup>14-16</sup>.



A utilização dos ACs é de suma importância para uma melhor visualização das imagens de RMI. Para um uso eficiente, esses ACs precisam ser compostos paramagnéticos, ter uma baixa toxicidade, rápida e completa excreção após o exame médico e uma elevada relaxação<sup>17,18</sup>. Para se ter uma elevada relaxação é necessário seguir alguns parâmetros (Figura 1), como conter moléculas de água na esfera interna de coordenação (q), aumento da velocidade de permuta entre as moléculas de água diretamente coordenadas ao metal ( $\tau_M$ ), tempo de relaxação do metal ( $\tau_S$ ) e diminuição da velocidade molecular do agente de contraste ( $\tau_R$ ). Mantendo esses parâmetros, pode-se promover suficientemente a estabilidade termodinâmica<sup>6</sup>. Atualmente, os ACs mais utilizados são os complexos de  $Gd^{3+}$ , óxidos de  $Fe^{2+}$  e complexos de  $Mn^{2+}$ . Nos próximos tópicos vamos discutir um pouco de cada um desses materiais.

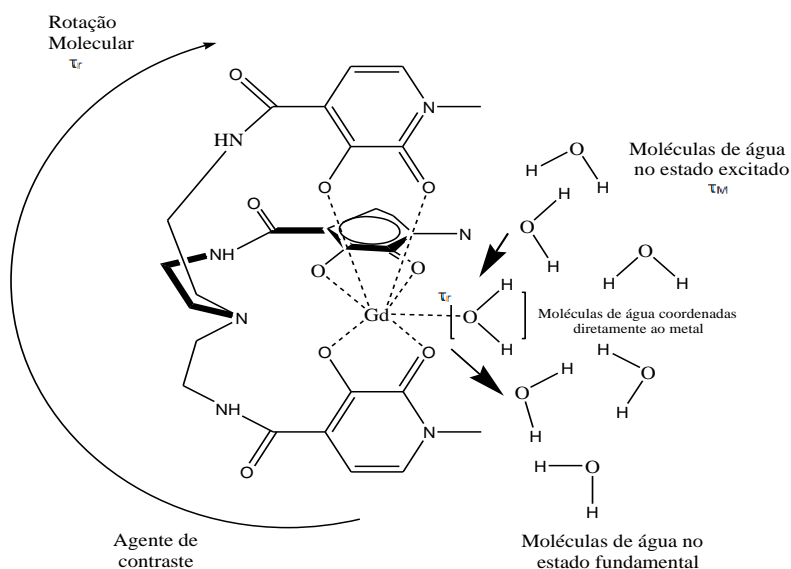


Figura 1 - Parâmetros que influenciam a relaxação das moléculas de água.

## 2-Agentes de Contraste

### 2.1-Agentes de Contraste baseados em complexos de gadolínio.

O gadolínio (Gd) é um metal de transição interno pertencente a família dos lantanídeos<sup>19</sup>. Desde os relatos iniciais, o Gd tornou-se o centro metálico mais utilizado para a produção de ACs<sup>20</sup>. Os sete elétrons desemparelhados do Gd combinados com um tempo de relaxação

relativamente longo, torna este lantanídeo um AC eficaz<sup>8</sup>. O Gd vem sendo utilizado como AC desde o final da década de 1980, esses ACs alteram tanto o tempo de relaxação  $T_1$  como o  $T_2$ , porém estudos mostram que são mais eficazes em  $T_1$ <sup>15,21-25</sup>. Até o ano de 1987, apenas 30 artigos poderiam ser encontrados na literatura relatando o uso do Gd como AC, 10 anos mais tarde já era possível encontrar mais de 600 referências a cada ano<sup>15</sup>.

O gadolínio só tem um estado de oxidação disponível em potenciais acessíveis biologicamente ( $Gd^{3+}$ )<sup>10</sup>. O íon  $Gd^{3+}$ , quando livre na circulação, é bastante tóxico com meia-vida biológica de algumas semanas<sup>22</sup>. Assim, para diminuir sua toxicidade, o  $Gd^{3+}$  é complexado com ligantes quelatos reduzindo sua meia-vida no organismo por volta de 1,5 hora. O íon  $Gd^{3+}$ , quando complexado a uma molécula, tem sua farmacocinética alterada, acelerando sua depuração e, portanto, reduzindo acentuadamente a sua toxicidade relativa<sup>22,26-29</sup>. A Figura 2 mostra os ligantes mais utilizados nos complexos de  $Gd^{3+}$ .

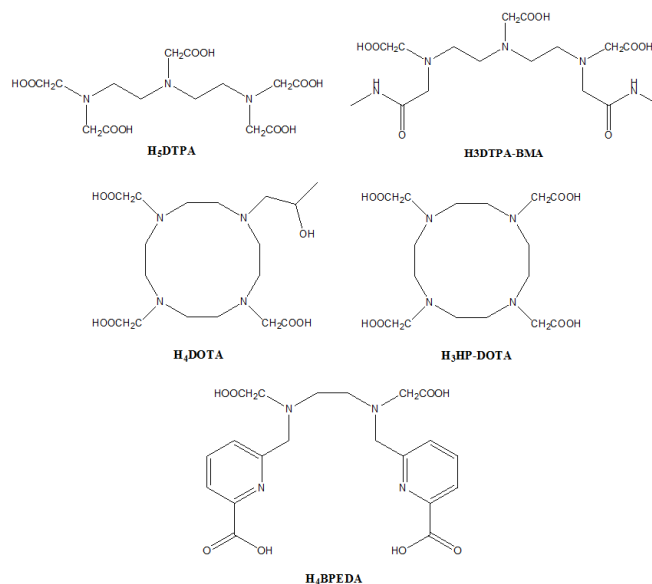


Figura 2 - Ligantes mais utilizados nos complexos de  $Gd^{3+}$ .

Os ACs baseados em complexos de  $Gd^{3+}$  mais utilizados atualmente são Gd-DTPA e Gd-DOTA (Figura 2). O Gd-DTPA foi o primeiro complexo a ser utilizado como AC oral negativo, é muito utilizado em exames para o tratamento gastrointestinal<sup>30,31</sup>. O complexo Gd-DOTA é o AC mais utilizado devido a sua alta estabilidade, esse composto reduz o tempo de

relaxação  $T_1$  (e até certo ponto dos tempos de relaxação  $T_2$  e  $T_2^*$ ), é frequentemente utilizado durante a visualização de lesões intracranianas com vascularização anormal ou anomalias na barreira sangue-cérebro<sup>16,32,33</sup>. Entretanto, a sua alta toxidez faz com que recentes estudos surjam no intuito de desenvolver novos ACs.

## 2.2-Óxidos de ferro como agentes de contraste.

O Ferro (Fe) é um elemento químico de número atômico 26 e massa atômica 56 u. Este metal de transição é encontrado no grupo 8 (VIII B) da tabela periódica. É o quarto elemento mais abundante da crosta terrestre (aproximadamente 5%)<sup>34</sup>. Esse metal já é utilizado há milhares de anos, os primeiros indícios do uso do ferro aconteceram em torno de 4000 a 3500 a.C<sup>16</sup>. O Ferro é encontrado também nos minerais, como óxido de ferro. Os principais óxidos de ferro comumente encontrados na natureza são: hematita ( $Fe_2O_3$ ), magnetita ( $Fe_3O_4$ ) e goethita ( $\alpha-Fe_2O_3$ )<sup>35,36</sup>.

As nanopartículas superparamagnéticas de óxido de ferro (do inglês SPIONs - *Superparamagnetic iron oxide nanoparticles*) são de considerável interesse na nanociência e nanotecnologia devido às suas dimensões em nanoescala, natureza não tóxica e propriedades magnéticas superiores<sup>37-40</sup>. Uma nanopartícula pode ser definida como uma partícula que tem pelo menos 1 nm de dimensão e não mais que 100 nm. No que diz respeito às nanopartículas, as propriedades magnéticas e outras propriedades físicas estão dependentes do seu tamanho. Os SPIONs têm despertado, atualmente, um grande interesse nas pesquisas como ACs<sup>41,42,43</sup>. Suas principais características são redução do tempo de relaxação  $T_2$  e  $T_2^*$ , excelentes propriedades magnéticas, biocompatibilidade e biodegradabilidade.

Os SPIONs atuam principalmente para alterar os valores de  $T_2$  dos átomos de  $^1H$  e  $^{17}O$  da água do tecido<sup>45,46</sup>. O acoplamento dipolar entre os momentos magnéticos dos hidrogênios da água e os momentos magnéticos das partículas causam uma defasagem eficiente na rotação e na relaxação em  $T_2$  levando a uma diminuição da intensidade do sinal. O contraste proporcionado por SPIONs em  $T_2$  é denominado realce do contraste negativo, assim, áreas com alta concentrações de SPIONs aparecem escuras nas imagens de RMI<sup>41</sup>. Entre os óxidos de ferro mais utilizados como ACs, podemos citar a magnetita<sup>24,41</sup>, entretanto mais recentemente estudos vêm sendo realizados também com a ferroxita ( $\delta-FeOOH$ )<sup>25,44</sup>.

A magnetita ( $\text{Fe}_3\text{O}_4$ ) é um mineral ferrimagnético que contém ferro em dois estados de oxidação,  $\text{Fe}^{2+}$  e  $\text{Fe}^{3+}$ . A cela unitária é composta por 56 átomos: 32 ânions de  $\text{O}^{2-}$ , 16 cátions de  $\text{Fe}^{3+}$  e 8 cátions de  $\text{Fe}^{2+}$ . Sua fórmula química é  $\text{Fe}_3\text{O}_4$ , porém, é definida mais apropriadamente como  $\text{FeO}\cdot\text{Fe}_2\text{O}_3$ <sup>47</sup>. Esse material pode ser usado como catalisador para síntese da amônia<sup>48</sup>, por ser um material ferromagnético e não tóxico para os seres humanos, a magnetita é também muito utilizada para a medicina como por exemplo, ACs para RMI<sup>49</sup>.

A maghemita ( $\gamma\text{-Fe}_2\text{O}_3$ ) é um mineral ferrimagnético e possui a mesma estrutura da magnetita. A maghemita é formado pelo intemperismo ou oxidação de baixa temperatura dos espinelios contendo ferro ferroso, comumente magnetita<sup>50</sup>. A maghemita possui uma alta estabilidade química e um baixo custo, assim, esse material tem uma vasta aplicação: uma delas é como pigmento magnético no suporte de gravação eletrônica, desde 1940<sup>51</sup>. Uma outra aplicação desse material é em biomedicina, pois são biocompatíveis e não tóxico para os seres humanos<sup>52</sup>.

Recentemente, outra importante fase de óxido de ferro magnético que vem se destacando na literatura é o  $\delta\text{-FeOOH}$ , um polimorfo de vários oxidróxidos de ferro de estruturas de coordenação e cristalográfia conhecidas, baseadas em um empacotamento hexagonal, semelhante ao da hematita ( $\alpha\text{-Fe}_2\text{O}_3$ ), formado por octaedros de coordenação  $\text{Fe-O}$ <sup>53</sup>. Estudos mostram que a face 100 da magnetita e da ferroxita possui um subdomínio quiral, assim, as moléculas de água do organismo interagem preferencialmente na face 100 desses óxidos, a Figura 3a e 3b mostra a face 100 do  $\text{Fe}_3\text{O}_4$  e do  $\delta\text{-FeOOH}$ , respectivamente.

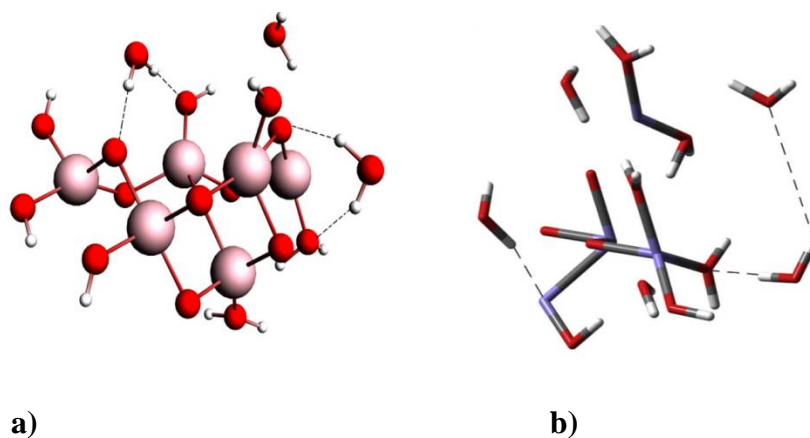


Figura 3 - Face 100 do a)  $\text{Fe}_3\text{O}_4$  com moléculas de água, e do b)  $\delta\text{-FeOOH}$  com moléculas de água.

### 2.3-Complexos de Manganês

O manganês (Mn) possui número atômico 25 e massa atômica 54,93 u, na temperatura ambiente está no estado sólido<sup>54,55</sup>. Situa-se no grupo 7 (7B) da tabela periódica, sendo um metal de transição externa, possui ponto de fusão de 1260°C e densidade de 7,2g/cm<sup>3,56</sup>. O metal apresenta uma cor prata cinzenta, é duro e quebradiço. Seus estados de oxidação mais comuns são +2, +3, +4, +6 e +7, o Mn é um átomo paramagnético possuindo cinco elétrons desemparelhados<sup>57,58</sup>. Atualmente, os complexos de Mn<sup>2+</sup> estão sendo muito estudados para substituir os ACs clássicos baseados em Gd<sup>3+</sup>, uma vez que os complexos de Mn<sup>2+</sup> são menos tóxicos para o organismo e alteram o tempo de relaxação T<sub>1</sub> dos hidrogênios da água<sup>59</sup>. Dentre os complexos de Mn<sup>2+</sup> utilizados como ACs, podemos citar o complexo [MnH3buea(OH)]<sup>-2</sup> (Figura 4a). De fato, os complexos de Mn<sup>2+</sup> com ligantes com a terminação oxo e hidroxilo podem simular uma variedade de metaloproteínas<sup>60</sup>. Os complexos biomédicos fornecem uma visão sobre os efeitos de protonação das espécies metal-oxo sem a complexidade introduzida pela proximidade da estrutura proteica, como por exemplo o ligante ([H3buea]<sup>3-</sup>) que tem ambas as formas monoméricas Mn-OH e Mn-OXO com vários estados de oxidação, porém a estrutura mais estável em solução é o complexo [MnH3buea(OH)]<sup>-2</sup>, que possui estado de oxidação +2, a Figura 4b mostra o complexo [MnH3buea(OH)]<sup>-2</sup> coordenado com moléculas de água<sup>25,61</sup>. Estudos mostram<sup>60</sup> que esse complexo pode ser um promissor AC, pois quando em contato com o organismo, ele consegue diminuir significativamente o tempo de relaxação T<sub>1</sub> dos átomos de <sup>1</sup>H e <sup>17</sup>O das moléculas de água. Entretanto, na última década, complexos de outros metais paramagnéticos, tais como o níquel, são também propostos como promissores ACs.

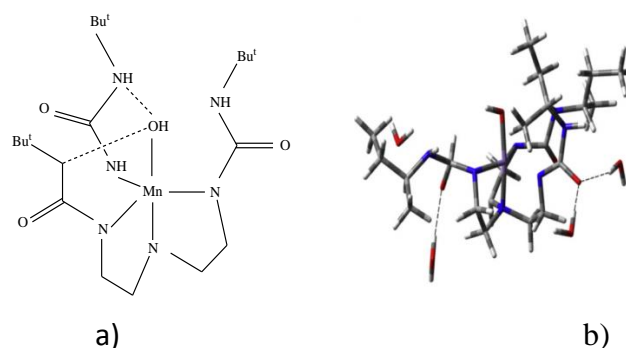


Figura 4 - Estrutura do complexo a) [MnH3buea(OH)]<sup>-2</sup> b) [MnH3buea(OH)]<sup>-2</sup> com moléculas de água.

## 2.4-Complexos de Níquel: agentes de contraste menos convencional.

O Níquel (Ni) possui número atômico 28 e massa atômica 58,7 u, é sólido a temperatura ambiente. É um elemento de transição situado no grupo 10 (8 B) da tabela periódica. A temperatura ambiente, é um metal paramagnético podendo apresentar coloração branca ou prateada, seus estados de oxidação mais comuns são 0, +1, +2 e +3<sup>62</sup>.

Além dos ACs já mencionados, existem uma série de ACs menos convencionais baseados em complexos de Ni<sup>2+</sup>, que ainda estão sendo desenvolvidos e estudados. Os complexos de Ni<sup>2+</sup> podem encurtar o tempo de relaxação T<sub>1</sub> dos átomos de <sup>1</sup>H e <sup>17</sup>O da água, desta forma, podem ser usados como promissores ACs<sup>63</sup>, alguns complexos de Ni<sup>2+</sup> já estudados como ACs estão apresentados na Figura 5.

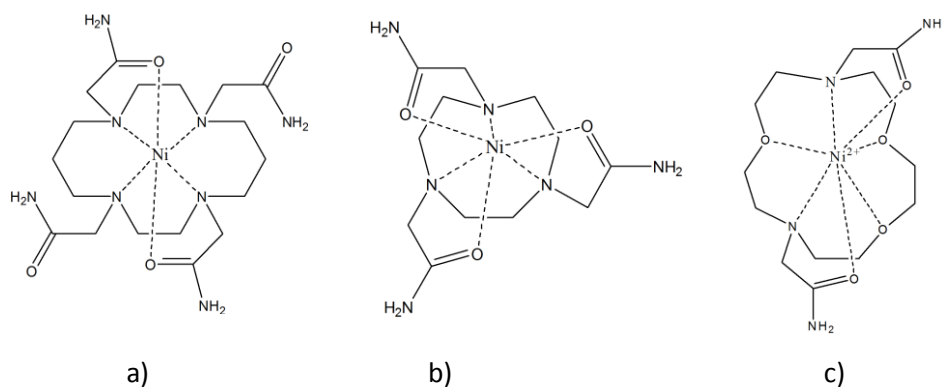


Figura 5 - Estrutura dos complexos de Ni<sup>2+</sup>.

O composto **5a** forma um complexo hexacoordenado com uma geometria antiprisma trigonal torcida. O composto **5b** também forma um complexo hexacoordenado, como por exemplo, o ligante tetracarboxilato (análogo ao ligante do complexo **5b**). O composto **5c** forma um complexo heptacoordenado com uma geometria bipirâmide pentagonal com cinco átomos de oxigênio e dois átomos de nitrogênio ligados diretamente ao metal formando um macrociclo<sup>64</sup>. Esses complexos possuem uma alta estabilidade termodinâmica e são capazes de diminuir o tempo de relaxação T<sub>1</sub> das moléculas de água presentes no organismo. Recentes estudos também apontam complexos de Co, Re e <sup>99</sup>Tc como promissores ACs<sup>65</sup>.

Nanopartículas de magnetita revestida com  $\text{Ni}^{2+}$  ( $\text{Ni-Fe}_2\text{O}_4$ ) foram estudadas para serem utilizadas como ACs em RMI, elas são capazes de alterar os tempos de relaxação  $T_1$  e  $T_2$ <sup>22</sup>. Verificou-se que o tempo de relaxação  $T_1$  para a solução aquosa das nanopartículas revestida com  $\text{Ni}^{2+}$  foi ligeiramente maior do que a de um AC de Gd-DTPA-BMA comercial<sup>22,66</sup>. O tempo de relaxação em  $T_2$ , no entanto, foi quase o dobro do AC comercial, Gd-DTPA-BMA. A experimentação animal também demonstrou que as nanopartículas de  $\text{Ni-Fe}_2\text{O}_4$  são adequadas para utilização como ACs ( $T_1$  ou  $T_2$ ) em RMI<sup>67,64,68</sup>. Além desses compostos, alguns estudos apontam materiais híbridos como promissores sondas espectroscópicas<sup>69,70</sup>.

## 2.5-Materiais híbridos.

As mais recentes tecnologias requerem materiais com combinação de propriedades que não são encontradas nos materiais convencionais<sup>69,71</sup>. Esses materiais são chamados de materiais híbridos, são mais comuns tendo uma parte orgânica e uma parte inorgânica (chamados de híbridos orgânicos-inorgânicos), podem ocorrer também de terem duas partes inorgânicas, como por exemplo, uma parte sendo um complexo e a outra constituída de nanopartículas de algum material<sup>27</sup>. Os materiais híbridos constituem uma alternativa para a produção de novos materiais multifuncionais, com uma larga faixa de aplicações<sup>70,72</sup>. Normalmente, as características desejadas não são encontradas em um único constituinte e a combinação adequada dos componentes tem levado à formação de materiais que apresentam propriedades complementares, que não são encontradas em uma única substância<sup>70,73</sup>.

Dentre das diversas aplicações desses materiais híbridos, podemos citar o uso deles como ACs, os estudos ainda são muito recentes, mas já mostram serem promissores<sup>69</sup>. Os materiais híbridos são capazes de alterar ambos os tempos de relaxação ( $T_1$  e  $T_2$ ) dos átomos de  $^1\text{H}$  e  $^{17}\text{O}$  das moléculas de água presentes no corpo. Recentemente, partículas de polímeros coordenados em nanoescala (CPPs) surgiram como uma alternativa para fornecer novas oportunidades para a engenharia de sistemas multifuncionais, os CPPs exibem altas cargas, alta biocompatibilidade, baixa toxicidade e oferecem a possibilidade de incluir funções adicionais<sup>73</sup>. Assim, a capacidade de incorporar diversos metais úteis para a RMI permite construir novos ACs para a imagiologia biomédica<sup>73</sup>. Nanopartículas de  $\text{Fe}^{3+}$  coordenados a polímeros à base de catecol (CPP-Fe) tem atuado como ACs ponderados em  $T_1$  para RMI<sup>73</sup>. Essas novas nanopartículas de  $\text{Fe}^{3+}$  podem

atuar como matrizes funcionais para encapsular nanopartículas superparamagnéticas de óxido de ferro (SPIONs) durante o processo de precipitação de polimerização. Essa combinação resulta na formação de um material híbrido (SPION@CPP-Fe), Figura 6, capaz de atuar em  $T_1$  e  $T_2$ . Esse material apresenta boas respostas ao serem estudados como ACs para RMI, os resultados mostram serem bastante promissores, comparados inclusive com os complexos de  $Gd^{3+73}$ .

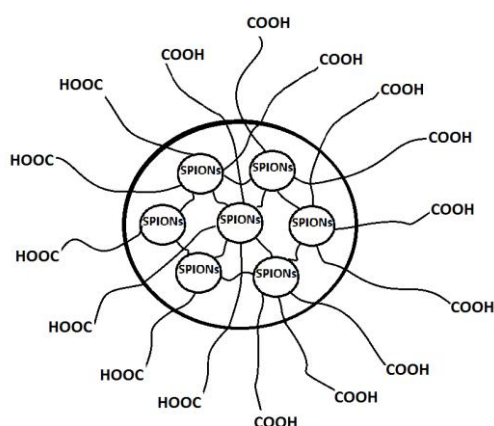


Figura 6 - Híbrido SPION@CPP-Fe.

### 3-Conclusões

Atualmente, novos compostos capazes de atuar como ACs são umas das mais promissoras áreas de pesquisa da medicina. Os ACs mais utilizados, atualmente, são complexos de  $Gd^{3+}$ , capazes de alterar os tempos de relaxação  $T_1$  e  $T_2$ , e apesar de serem bastante eficazes, a sua alta toxicidade faz com que novos estudos surjam para substituir esses ACs clássicos por outros compostos mais eficientes e menos tóxicos ao organismo.

Neste sentido, os SPIONs são capazes de atuar como ACs, estudos mostram que são eficientes e capazes de alterar o tempo de relaxação  $T_2$  dos átomos de  $^1H$  e  $^{17}O$  das moléculas de água e não são tóxicos para o organismo, os mais utilizados são a magnetita ( $Fe_3O_4$ ) e a ferroxita ( $\delta-FeOOH$ ). Além dos SPIONs, complexos de  $Mn^{2+}$ ,  $Ni^{2+}$  e compostos híbridos, são bastante estudados como novos ACs, ambos são capazes de alterar o tempo de relaxação  $T_1$ . No Brasil, esses ACs não clássicos ou ainda não foram introduzidos ou têm seu uso muito restrito, devido ao alto custo.



## Referências Bibliográficas:

1. Gerald, C. F. G. C.; Laurent, S. Classification and basic properties of contrast agents for magnetic resonance imaging. *Contrast media & molecular imaging* **2009**, *4*, 1. [[CrossRef](#)] [[PubMed](#)]
2. Mazzola, A. A. Ressonância magnética : princípios de formação da imagem e aplicações em imagem funcional Magnetic resonance : principles of image formation and applications in functional imaging. *Revista Brasileira de Física Médica* **2009**, *3*, 117.
3. Newquist, H. *The Human Body: The Story of How We Protect, Repair, and Make Ourselves Stronger (Smithsonian: Invention & Impact)*. Hardcover, 2015.
4. Chavhan, G. B.; Babyn, P. S.; Thomas, B.; Shroff, M. M.; Haacke, E. M. Principles, Techniques, and Applications of T2\*-based MR Imaging and Its Special Applications1. *RadioGraphics* **2009**, *29*, 1433. [[CrossRef](#)] [[PubMed](#)]
5. Oliveira, I. S.; Guimarães, A. P. Introdução as Interações Hiperfinas em Ions Livres. *Revista Brasileira de Ensino de Física* **2000**, *22*, 353.
6. Kaupp, M.; Bühl, M.; Malkin, V. G. *Calculation of NMR and EPR Parameters: Theory and Applications*. 2004. [[CrossRef](#)]
7. Lewars, E. G. *Computational Chemistry*. 2011.
8. GORDON, W. Der Compton effekt nach der Schrödingerschen Theorie. *Zeitschrift für Physik* **1926**, *40*, 117. [[CrossRef](#)]
9. BALASUBRAMANIAN, K. Relativistic effects in chemistry – *Part A*. 1997.
10. DIRAC, P. A. M. The Quantum Theory of the Electron (Part II). *Proceedings of the Royal Society of London* **1928**, *118*, 351. [[CrossRef](#)]
11. Hedega, E. D.; Kongsted, J.; Sauer, S. P. A.; Validating and Analyzing EPR Hyper fine Coupling Constants with Density Functional Theory. *Journal of Chemical Theory and Computation* **2013**, *9*, 2380. [[CrossRef](#)]
12. Almeida, K. J. Optical and Magnetic Properties of Copper (II) compounds, 2007.

[ [CrossRef](#) ]

13. Bačić, G.; Pavićević, A.; Peyrot, F. In vivo evaluation of different alterations of redox status by studying pharmacokinetics of nitroxides using magnetic resonance techniques. *Redox Biology* **2016**, *8*, 226. [[CrossRef](#)]
14. Umut, E. *et al.* Magnetic, optical and relaxometric properties of organically coated gold–magnetite (Au–Fe<sub>3</sub>O<sub>4</sub>) hybrid nanoparticles for potential use in biomedical applications. *Journal of Magnetism and Magnetic Materials* **2012**, *324*, 2373. [[CrossRef](#)]
15. Caravan, P.; Ellison, J. J.; McMurry, T. J.; Lauffer, R. B. Gadolinium ( III ) Chelates as MRI Contrast Agents : Structure , Dynamics , and Applications. *Chemical reviews* **1999**, *99*, 2293. [[CrossRef](#)]
16. Yazyev, O. V.; Helm, L. Gadolinium (III) ion in liquid water: structure, dynamics, and magnetic interactions from first principles. *The Journal of chemical physics* **2007**, *127*, 084506. [[CrossRef](#)] [[PubMed](#)]
17. Ferreira, C. S. D. O. Tese de doutorado, 2001. [[CrossRef](#)]
18. Wener, E. J.; Datta, A.; Jocher, C. J.; Raymond, K. N. High-Relaxivity MRI Contrast Agents: Where Coordination Chemistry Meets Medical Imaging. *Angewandte Chemie International Edition* **2008**, *47*, 8568. [[CrossRef](#)]
19. Lasoroski, A.; Vuilleumier, R.; Pollet, R. Hyperfine interactions in a gadolinium-based MRI contrast agent: high-frequency modulations from ab initio simulations. *The Journal of chemical physics* **2013**, *139*, 104115. [[CrossRef](#)]
20. Estelrich, J.; Sánchez-Martín, M. J.; Busquets, M.A. Nanoparticles in magnetic resonance imaging : from simple to dual contrast agents. *International Journal of Nanomedicine* **2015**, *10*, 1727. [[CrossRef](#)]
21. Werner, E. J.; Datta, A.; Jocher, C. J.; Raymond, K. N. High-relaxivity MRI contrast agents: where coordination chemistry meets medical imaging. *Angewandte Chemie (International ed. in English)* **2008**, *47*, 8568. [[CrossRef](#)] [[PubMed](#)]
22. Nogueira-barbosa, H.; Muglia, V. F; Complicações do uso intravenoso de agentes de

- contraste à base de gadolínio para ressonância magnética. *Radiologia Brasileira* **2008**, *41*, 263.
23. Zhang, Y. *et al.* Synergistic Effect of Human Serum Albumin and Fullerene on Gd-DO3A for Tumor-Targeting Imaging. *ACS Applied Materials & Interfaces* **2016**, *8*, 11246. [\[CrossRef\]](#)
24. Gonçalves, M. A.; Peixoto, F. C.; da Cunha, E. F. F.; Ramalho, T. C. Dynamics, NMR parameters and hyperfine coupling constants of the Fe<sub>3</sub>O<sub>4</sub>(100)–water interface: Implications for MRI probes. *Chemical Physics Letters* **2014**, *609*, 88. [\[CrossRef\]](#)
25. Gonçalves, M. A.; da Cunha, E. F. F.; Peixoto, F. C.; Ramalho, T. C. Probing thermal and solvent effects on hyperfine interactions and spin relaxation rate of  $\delta$ -FeOOH(100) and [MnH<sub>3</sub>buea(OH)]<sup>2-</sup>: Toward new MRI probes. *Computational and Theoretical Chemistry* **2015**, *1069*, 96. [\[CrossRef\]](#)
26. Martins, T. S.; Isolani, P. C.; Terras raras: aplicações industriais e biológicas, *Química Nova* **2005**, *28*, 111.
27. Li, Y.; Yang, Z.; Wang, B.; Liu, Z.; Li, S. Gd-complex labeled magnetite nanoparticles as fluorescent and targeted magnetic resonance imaging contrast agent. *Materials Letters* **2013**, *98*, 34. [\[CrossRef\]](#)
28. Ahmad, M. W. *et al.* Potential dual imaging nanoparticle : *Scientific Reports* **2015**, *5*, 8549. [\[CrossRef\]](#)
29. Flament, J. *et al.* In vivo CEST MR imaging of U87 mice brain tumor angiogenesis using targeted LipoCEST contrast agent at 7 T. *Magnetic resonance in medicine : official journal of the Society of Magnetic Resonance in Medicine / Society of Magnetic Resonance in Medicine* **2013**, *69*, 179. [\[CrossRef\]](#) [\[PubMed\]](#)
30. Esteban-Gómez, D.; de Blas, A.; Rodríguez-Blas, T.; Helm, L.; Platas-Iglesias, C. Hyperfine coupling constants on inner-sphere water molecules of Gd(III)-based MRI contrast agents. *Chemphyschem : a European journal of chemical physics and physical chemistry* **2012**, *13*, 3640. [\[CrossRef\]](#) [\[PubMed\]](#)
31. Duarte, J. A.; Alegre, A. P.; Furtado, C. A. M. Use of pineapple juice with gadopentetate

- dimeglumine as a negative oral contrast for magnetic resonance cholangiopancreatography: a multicentric study. *Abdominal Imaging* **2011**, *37*, 447. [[CrossRef](#)] [[PubMed](#)]
32. Boros, E.; Polasek, M.; Zhang, Z.; Caravan, P. Gd(DOTA) as a single amino acid Gd-complex as a modular tool for high relaxivity MR contrast agent development. *Journal of the American Chemical Society* **2012**, *134*, 19858. [[CrossRef](#)]
33. Strijkers, G. J.; Mulder, W. J. M.; Tilborg, G. A. F.; Van, T.; Nicolay, K. MRI Contrast Agents: Current Status and Future Perspectives. *Anti-Cancer Agents in Medicinal Chemistry* **2007**, *7*, 291. [[CrossRef](#)] [[PubMed](#)]
34. Al-Abadleh, H. A. Review of the bulk and surface chemistry of iron in atmospherically relevant systems containing humic-like substances. *Royal Society of Chemistry* **2015**, *5*, 45785. [[CrossRef](#)]
35. Molar, M. Fe 208. *Química Nova na Escola* **2010**, *32*, 2008.
36. Oliveira, Luiz C A; Fabris, J D; Pereira, M. C. ÓXIDOS DE FERRO E SUAS APLICAÇÕES EM PROCESSOS CATALÍTICOS: UMA REVISÃO Luiz. *Química Nova* **2013**, *36*, 123.
37. Tsai, Z.-T. *et al.* In situ preparation of high relaxivity iron oxide nanoparticles by coating with chitosan: A potential MRI contrast agent useful for cell tracking. *Journal of Magnetism and Magnetic Materials* **2010**, *322*, 208. [[CrossRef](#)]
38. Rojas, J. M. *et al.* Superparamagnetic iron oxide nanoparticle uptake alters M2 macrophage phenotype, iron metabolism, migration and invasion. *Nanomedicine: nanotechnology, biology, and medicine* **2016**, *12*, 1127. [[CrossRef](#)]
39. Ahmad, T. *et al.* Chitosan-coated nickel-ferrite nanoparticles as contrast agents in magnetic resonance imaging. *Journal of Magnetism and Magnetic Materials* **2015**, *381*, 151. [[CrossRef](#)]
40. Hocaoglu, I. *et al.* Cyto/hemocompatible magnetic hybrid nanoparticles (Ag<sub>2</sub>S–Fe<sub>3</sub>O<sub>4</sub>) with luminescence in the near-infrared region as promising theranostic materials. *Colloids and Surfaces B: Biointerfaces* **2015**, *133*, 198. [[CrossRef](#)]

41. Stephen, Z. R.; Kievit, F. M.; Zhang, M. Magnetite Nanoparticles for Medical MR Imaging. *National Institutes of Health* **2012**, *14*, 330. [[CrossRef](#)]
42. Fratila, R. M.; Rivera-fernández, S.; De, J. M.; Rivera-fernández, S.; Rivera-fernández, S. Shape matters: synthesis and biomedical applications of high aspect ratio magnetic nanomaterials. *Nanoscale* **2015**, *18*, 8233. [[CrossRef](#)] [[PubMed](#)]
43. Hocaoglu, I. *et al.* Cyto/hemocompatible magnetic hybrid nanoparticles (Ag<sub>2</sub>S–Fe<sub>3</sub>O<sub>4</sub>) with luminescence in the near-infrared region as promising theranostic materials. *Colloids and Surfaces B: Biointerfaces* **2015**, *133*, 198. [[CrossRef](#)]
44. Khosroshahi, M. E.; Rezvani, H. A.; Keshvari, H.; Bonakdar, S.; Tajabadi, M. Evaluation of cell viability and T2 relaxivity of fluorescein conjugated SPION-PAMAM third generation nanodendrimers for bioimaging. *Materials science & engineering. C, Materials for biological applications* **2016**, *62*, 544. [[CrossRef](#)]
45. Flament, J. *et al.* In vivo CEST MR imaging of U87 mice brain tumor angiogenesis using targeted LipoCEST contrast agent at 7 T. *Magnetic resonance in medicine: official journal of the Society of Magnetic Resonance in Medicine / Society of Magnetic Resonance in Medicine* **2013**, *69*, 179. [[CrossRef](#)] [[PubMed](#)]
46. Han, L.; Zhou, X. Synthesis and characterization of liposomes nano-composite-particles with hydrophobic magnetite as a MRI probe. *Applied Surface Science* **2016**, *376*, 252. [[CrossRef](#)]
47. Augustus, G.; Ribeiro, P. As Propriedades Magneticas da Materia : um Primeiro Contato. *Revista Brasileira de Ensino de Física* **2000**, *22*, 299.
48. Appl, M. in *Ullmann's Encyclopedia of Industrial Chemistry* (Wiley-VCH Verlag GmbH & Co. KGaA), 2011. [[CrossRef](#)]
49. Xu, F.; Cheng, C.; Chen, D. X.; Gu, H. Magnetite Nanocrystal Clusters with Ultra-High Sensitivity in Magnetic Resonance Imaging. *ChemPhysChem* **2012**, *13*, 336. [[CrossRef](#)]
50. Hanesch, M. Raman spectroscopy of iron oxides and (oxy)hydroxides at low laser power and possible applications in environmental magnetic studies. *Geophysical Journal International* **2009**, *177*, 941. [[CrossRef](#)]

51. Litter, M. I.; Blesa, M. A. Photodissolution of iron oxides. IV. A comparative study on the photodissolution of hematite, magnetite, and maghemite in EDTA media. *Canadian Journal of Chemistry* **1992**, *70*, 2502. [[CrossRef](#)]
52. Pankhurst, Q. A.; Connolly, J.; Jones, S. K.; Dobson, J. Applications of magnetic nanoparticles in biomedicine. *Journal of Physics D: Applied Physics* **2003**, *36*, R167. [[CrossRef](#)]
53. Simpson, A. W. Some superparamagnetic properties of fine particles  $\delta$ -FeOOH. *Journal of Applied Physics*. *Journal of Applied Physics* **1962**, *33*, 1203.
54. Koretsky, A. P.; Silva, A. C. Manganese-enhanced magnetic resonance imaging (MEMRI). *NMR in biomedicine* **2004**, *17*, 527. [[CrossRef](#)] [[PubMed](#)]
55. Haribabu, V.; Farook, A. S.; Goswami, N.; Murugesan, R.; Girigoswami, A. Optimized Mn-doped iron oxide nanoparticles entrapped in dendrimer for dual contrasting role in MRI. *Journal of Biomedical Materials Research Part B: Applied Biomaterials* **2016**, *104*, 817. [[CrossRef](#)]
56. Haribabu, V.; Farook, A. S.; Goswami, N.; Murugesan, R.; Girigoswami, A. Optimized Mn-doped iron oxide nanoparticles entrapped in dendrimer for dual contrasting role in MRI. *Journal of Biomedical Materials Research Part B: Applied Biomaterials* **2016**, *104*, 817. [[CrossRef](#)]
57. Abreu, S. F. Ferro e metais da indústria do aço. *Recursos Minerais do Brasil* **1973**, *2*, 451.
58. Jin, M. *et al.* Hydroxy double salts intercalated with Mn(II) complexes as potential contrast agents. *Solid State Sciences* **2016**, *53*, 9. [[CrossRef](#)]
59. Lee, Y. C. *et al.* The Use of Silica Coated MnO Nanoparticles to Control MRI Relaxivity in Response to Specific Physiological Changes. *Biomaterials* **2012**, *33*, 3560. [[CrossRef](#)]
60. Gupta, R.; Borovik, A. S. Monomeric MnIII/II and FeIII/II Complexes with Terminal Hydroxo and Oxo Ligands: Probing Reactivity via O-H Bond Dissociation Energies. *Journal of the American Chemical Society* **2003**, *125*, 13234. [[CrossRef](#)]
61. Gupta, R.; Taguchi, T.; Borovik, A. S.; Hendrich, M. P. Characterization of Monomeric Mn. *inorganic chemistry* **2013**, *52*, 12568. [[CrossRef](#)]

62. Carnes, M. *et al.* A Stable Tetraalkyl Complex of Nickel(IV). *Angewandte Chemie* **2009**, *121*, 3435. [[CrossRef](#)]
63. Olatunde, A. O.; Dorazio, S. J.; Sperryak, J. A.; Morrow, J. R. The NiCEST approach: nickel(II) paraCEST MRI contrast agents. *Journal of the American Chemical Society* **2012**, *134*, 18503. [[CrossRef](#)] [[PubMed](#)]
64. Olatunde, A. O.; Dorazio, S. J.; Sperryak, J. A.; Morrow, J. R. The NiCEST approach: nickel(II) paraCEST MRI contrast agents. *Journal of the American Chemical Society* **2012**, *134*, 18503. [[CrossRef](#)] [[PubMed](#)]
65. Jackson, G. E.; Byrne, M. J.; Blekkenhorst, G.; Hendry, A. J. Chromium - cage complex as contrast agent in MR imaging—Biodistribution studies of the [ <sup>57</sup> Co]cobalt analogue. *International Journal of Radiation Applications and Instrumentation. Part B. Nuclear Medicine and Biology* **1991**, *18*, 855. [[CrossRef](#)] [[PubMed](#)]
66. Accardo, A.; Tesauro, D.; Aloj, L.; Pedone, C.; Morelli, G. Supramolecular aggregates containing lipophilic Gd(III) complexes as contrast agents in MRI. *Coordination Chemistry Reviews* **2009**, *253*, 2193. [[CrossRef](#)]
67. Ahmad, T.; Rhee, I.; Hong, S.; Chang, Y.; Lee, J. Ni-Fe<sub>2</sub>O<sub>4</sub> Nanoparticles as Contrast Agents for Magnetic Resonance Imaging. *Journal of Nanoscience and Nanotechnology* **2011**, *11*, 5645. [[CrossRef](#)]
68. Gao, D. *et al.* Compact chelator-free Ni-integrated CuS nanoparticles with tunable near-infrared absorption and enhanced relaxivity for in vivo dual-modal photoacoustic/MR imaging. *Nanoscale* **2015**, *7*, 17631. [[CrossRef](#)]
69. Zuo, L. *et al.* New Technology and Clinical Applications of Nanomedicine. *Medical Clinics of North America* **2007**, *91*, 845. [[CrossRef](#)]
70. José, N. M. Materiais híbridos orgânico-inorgânicos: preparação e algumas aplicações. *Química Nova* **2005**, *28*, 281.
71. You, B. *et al.* A Hybrid Silica Nanoreactor Framework for Encapsulation of Hollow Manganese Oxide Nanoparticles of Superior T<sub>1</sub> Magnetic Resonance Relaxivity. *Advanced Functional Materials* **2015**, *33*, 5269. [[CrossRef](#)]

72. Esteves, A. C. C.; Barros-timmons, A.; Trindade, T. Nanocompósitos de matriz polimérica: estratégias de síntese de materiais híbridos. *Química Nova* **2004**, *27*, 798.
73. Borges, M.; Yu, S.; Laromaine, A., Roig, A.; Suárez-García, S.; Lorenzo, J.; Ruiz-Molina, D.; Novio, F. D Dual. T1/T2 MRI contrast agent based on hybrid SPION@coordination polymer nanoparticles, *Royal Society of Chemistry* **2015**, *5*, 86779. [CrossRef]



**Article 2-Optimal Wavelet Signal Compression as an Efficient Alternative to Investigate Molecular Dynamics Simulations: Application to Thermal and Solvent Effects of MRI Probes**

(article published in *Theoretical Chemistry Accounts-TCA*)

## Abstract

Currently, cancer is one of the most serious problems facing humanity and one of the most widely used and versatile diagnostic techniques is Magnetic Resonance Imaging (MRI), which may require an injection of contrast agents (CAs). CAs are paramagnetic compounds capable of increasing the relaxation rate of water protons, thereby obtaining clearer MRI exam images. In this work, the solvent and thermal effects on spectroscopic parameters of  $[\text{Fe}(\text{H}_2\text{O})_6]^{2+}$ ,  $[\text{Mn}(\text{H}_2\text{O})_6]^{2+}$ ,  $[\text{Gd}(\text{H}_2\text{O})_8]^{3+}$  and  $\gamma\text{-Fe}_2\text{O}_3$ , coordinated to explicit water molecules, were studied in the light of the classical and quantum methods. For the classical part of the simulation a new method of selection of configurations from the molecular dynamics simulations, denominated Optimal Wavelet Signal Compression Algorithm (OWSCA), is presented. Our findings indicate that OWSCA leads to a good agreement with the experimental available data and the thermal effects greatly influence our system. Thus, the Molecular Dynamics (MD) calculations are indispensable for this type of system. Our results show the  $\gamma\text{-Fe}_2\text{O}_3$  as a promising alternative to conventional contrast agents.

## 1-Introduction

Cancer is a leading cause of death worldwide, having great impact on the quality of life of many people. Among the most common and aggressive types, breast cancer is at the top of the list [1]. This outlook is still aggravated, because this type of cancer is fatal and its preoperative and postoperative diagnoses are difficult. In this context, the mortality rate of the breast cancer can drastically be reduced by early diagnosis and correct treatment. Nevertheless, one of the biggest challenges of diagnostic imaging is to develop a system able to detect the focus of cancer with high resolution in different environments [1, 2].

To date, many techniques, such as tomography, ultrasound endoscopy and magnetic resonance imaging (MRI), are used. However, due to sensitivity and easy operation analysis in live systems, MRI is one of the most employed techniques for cancer diagnosis [3, 4]. MRI uses the NMR signal of water protons present in the body, whose contrast among different tissues is related to NMR relaxation rates, longitudinal ( $R_1=1/T_1$ ) or transverse ( $R_2=1/T_2$ ), of those nuclei. In most cases, only the natural relaxation rate of water protons is not sufficient for providing good visualization of tissue images [3]. Thus, to increase the relaxation rate and provide a more detailed view of tissues, the use of paramagnetic compounds as contrast agents (CAs) able to enhance the relaxation longitudinal and transverse time ( $T_1$  and  $T_2$ ) of water molecules in the vicinity of CA[5], is a quite common strategy. It is important to keep in mind that both relaxation rates ( $R_1$  and  $R_2$ ) depend on the hyperfine coupling constant ( $\frac{A}{h}$ ) between the electron spin of the metal ion and the nuclear spin of  $^1\text{H}$  and  $^{17}\text{O}$  of the water molecules [6, 7].

Currently, the most widely used contrast agents for MRI are based on gadolinium ( $\text{Gd}^{3+}$ ) complexes [8]. These materials can shorten the  $T_2$  relaxation time, affecting also the  $T_1$  relaxation time in small proportion. Although gadolinium metallic complexes are highly efficient in the proton relaxation of water molecules, in general, they are very toxic and have serious effects on the organism. Thus, the interest in developing other MRI-probes able to diminish health risks has increased significantly [9]. Recently, superparamagnetic iron oxide nanoparticles (SPIONs) are a new and promising class of compounds being studied to substitute the classics CAs based on  $\text{Gd}^{3+}$  complexes [8]. The SPIONs are ferromagnetic materials which have their iron atoms magnetic moments aligned with each other, producing a net magnetization mainly due to this magnetic property, which makes them important SPIONs for medical imaging applications

[10, 11]. These nanoparticles can shorten the  $T_1$ ,  $T_2$  and  $T_2^*$  relaxation times due to the difference between sensitivity the iron oxide core and the surrounding water. These properties make them attractive to act as CAs in MRI [7, 12, 13]. Although magnetic nanoparticles of iron oxide, SPIONs, such as magnetite ( $\text{Fe}_3\text{O}_4$ ) and the  $\delta$ - $\text{FeOOH}$ , have been already studied as promising contrast agents for MRI [8], to our knowledge there is no any report about the use of maghemite ( $\gamma$ - $\text{Fe}_2\text{O}_3$ ) as CA.

The  $\gamma$ - $\text{Fe}_2\text{O}_3$  is a ferromagnetic oxide with a structure very similar to magnetite ( $\text{Fe}_3\text{O}_4$ ), however the main difference is the presence of  $\text{Fe}^{3+}$  as the only cation in the structure [14]. Thus, it is believed that face 100 of  $\gamma$ - $\text{Fe}_2\text{O}_3$  has a chiral subdomain, as in face 100 of  $\text{Fe}_3\text{O}_4$  and of  $\alpha$ - $\text{Fe}_2\text{O}_3$ , which it is very important for many processes [15, 16]. Recently, maghemite nanoparticles have been widely used in biomedicine because their magnetism allows remote manipulation with external fields and they are biocompatible and not potentially toxic to humans [17].

In spite of its great importance, little computational work has appeared on the study of spectroscopic properties of MRI probes in solution. Actually, understanding this process requires the evaluation of the solvent and thermal effects on the relaxation rate as well as hyperfine coupling constants ( $A_{\text{iso}}$ ) of water molecules on paramagnetic ions [18, 19]. One alternative to exploit these effects is the use of molecular dynamics (MD) simulations with an adequate force field, that gives us direct information of inter and intramolecular movements of the system at the atomistic level [20]. The electronic structure calculations are, then, subsequently incorporated to take into account the quantum effects. However, the main difficulty of MD calculations is the number of conformations generated to perform the quantum mechanical (QM) calculations. In fact, it would be computationally infeasible to perform QM calculations for all conformers. In this context, many theoretical methods have been developed for selecting configurations from MD simulations [21]. Currently, the most common and widely used method is to select random conformations from MD simulations [22, 23]. Since random configurations are selected, it is possible that crucial system configurations can be neglected, having great consequences for accurate determination of electronic and steric parameters of the system. Another possibility is to employ statistical methods which are able to capture the average properties of the studied systems [24, 25]. In this sense, since 1993, the Coutinho and Canuto group has proposed and validated the sequential quantum mechanics and molecular mechanics procedure [26] using statistical inefficiency (SI) calculations for selecting configurations from Monte Carlo simulations, which

has been successfully employed on many occasions [18, 24, 25]. However, the recent use of the wavelet transform analysis has shown to be a promising technique, in computer graphics [26], for image processing [27], blood pressure tests [28], as well as identification of patterns in molecular simulations [29]. Aiming, then, to reduce the number of QM calculations without loss of the relevant information from the simulation, a new method based on the wavelet analysis for selecting MD conformations had been developed, Optimal Wavelet Signal Compression Algorithm (OWSCA). In addition, thermal and solvent effects on  $^1\text{H}$  and  $^{17}\text{O}$  hyperfine coupling constants ( $A_{\text{iso}}$ ) of promising MRI probes in solution have been investigated at the DFT level.

## 2-Computational methods

### 2.1-Construction and optimization of $[\text{Fe}(\text{H}_2\text{O})_6]^{2+}$ , $[\text{Mn}(\text{H}_2\text{O})_6]^{2+}$ , $[\text{Gd}(\text{H}_2\text{O})_8]^{3+}$ and $\gamma\text{-Fe}_2\text{O}_3$

Initially, the of  $\gamma\text{-Fe}_2\text{O}_3$  structure was built using the following coordinates: Space group Fd-3m, network parameters:  $a=8.4053(1)\text{\AA}$ ; and the atom position parameters were: Fe (1): x, y, z = 0.1250; Fe(2): x, y, z: 0.5000; O: x,y,z: 0.2512 [30]. The structure was optimized using the ADF-BAND program [31] with the functional PBE and the base Slater triple-zeta (TZP) for all atoms. For  $[\text{Fe}(\text{H}_2\text{O})_6]^{2+}$ ,  $[\text{Mn}(\text{H}_2\text{O})_6]^{2+}$  and  $[\text{Gd}(\text{H}_2\text{O})_8]^{3+}$  complex the structures were optimized using the Gaussian 09 program [32], with the functional B3LYP and the basis set Lanl2dz for the  $\text{Fe}^{2+}$ ,  $\text{Mn}^{2+}$  and  $\text{Gd}^{3+}$  atoms and 6-311g++(d,p) for hydrogen and oxygen atoms were employed.

### 2.2-Molecular Dynamics Simulations

After the optimization step, Molecular Dynamics (MD) simulations were performed for the  $\gamma\text{-Fe}_2\text{O}_3$  using the REAX-FF program, which was developed and validated by van Duin and coworkers (REAX-FF) [33]. The MD simulations were performed at 310.65 K (physiological temperature). In fact, this temperature is suitable to simulate the behavior of compounds in biological systems [22]. As usual, periodic boundary conditions (PBC) and a cutoff distance of 10.0  $\text{\AA}$  have been applied. The system consists of 300 water molecules in a cubic cell with a side

of 20 Å. The volume of the cube was determined by the density of liquid water ( $\rho=0.996 \text{ g.cm}^{-3}$ ). The constant atom number, temperature and volume (NVT) ensemble, known as the canonical ensemble, was applied for both systems. First, the initial configuration was minimized using the steepest descent and the conjugate gradient algorithm until an energy gradient of  $0.01 \text{ kcal.mol}^{-1}\text{Å}^{-1}$  was reached. In the  $\gamma\text{-Fe}_2\text{O}_3$  system, with water molecules, the simulation consisting of a thermalization phase of 500 ps, followed by an additional period of 2.0 ns, was employed.

The simulation of  $\gamma\text{-Fe}_2\text{O}_3$  and  $[\text{Fe}(\text{H}_2\text{O})_6]^{2+}$  were performed using the force field FEOCH [34], which was developed and validated for the iron oxides. Turning now to systems  $[\text{Mn}(\text{H}_2\text{O})_6]^{2+}$  [35] and  $[\text{Gd}(\text{H}_2\text{O})_8]^{3+}$  [36], the force field NiCH was used.

### **2.3-Computational Implementation of the Optimal Wavelet Signal Compression Algorithm (OWSCA)**

The optimal wavelet-signal compression algorithm (OWSCA), discussed in the previous section, was performed in the Matlab 7.6<sup>®</sup> [37] software with its built-in Wavelet Toolbox. The time-series data of MD conformations was used as an input for the OWSCA. This method is composed of four steps, (i) the discrete wavelet transform of the original MD data; (ii) optimization of compression parameters, (iii) wavelet compression and (iv) inverse discrete wavelet transform, resulting in a lower number of MD conformations. Firstly, in the wavelet transform, the original dataset is decomposed into different frequencies, allowing a more precise evaluation of the MD conformation profiles. Secondly, in the wavelet compression, the decomposed dataset of MD conformations is compressed, according to a particular compression rule. This step is crucial because an optimization procedure is conducted, allowing to select the best MD conformations which represents the most significant part of the dataset. A Genetic Optimization Algorithm [38] was used for this purpose.

## 2.4-Statistical inefficiency (SI) and hyperfine coupling constant (HFCC) calculations

The statistical inefficiency (SI) calculations were performed using *the Matlab 7.6*® software [34]. From the simulation MD, uncorrelated configurations were selected for the hyperfine coupling constant (HFCC or  $A_{\text{iso}}$ ) calculations.

The HFCC calculations were performed using the Gaussian 09 program [32], for the equilibrium structure, the functional PBE1PBE, BP86, B3LYP and BLYP were used. For the other structures, we used functional PBE1PBE, with the basis set aug-cc-pVTZ-J [39] for the oxygen and hydrogen atoms and Lanl2dz for the iron atoms for all structures. It is important to also mention the notation used in the discussion of this work, the notation used has already been used successfully in other papers. Thus, we follow the following notation: level of  $A_{\text{iso}}$  computation//level of geometry optimization or MD simulation. For example: the notation (PBE1PBE(H<sub>2</sub>O)//PBE1PBE(H<sub>2</sub>O)) means  $A_{\text{iso}}$  computation with explicit solvent//geometry optimization with explicit solvent; (PBE1PBE(H<sub>2</sub>O)/PCM//PBE1PBE(H<sub>2</sub>O)) means  $A_{\text{iso}}$  computation with explicit and implicit solvent (PCM)//geometry optimization with explicit solvent molecules. The notation (MD(H<sub>2</sub>O)//MD(H<sub>2</sub>O)) takes into account the dynamic effect (MD simulation). For all simulations the system was composed of  $\gamma\text{-Fe}_2\text{O}_3$  with 300 water molecules in a cubic cell with a side of 20 Å, however, for quantum mechanical (QM) calculations ( $A_{\text{iso}}$ ), we considered only the first layer of solvation. It would not be computationally feasible to perform the QM calculations with 300 water molecules in the system. The calculations with the solvent hybrid (implicit and explicit) were performed to verify whether the first hydration layer was sufficient to realistically represent our system.

## 3-Results and Discussion

### 3.1-Time correlation

Recently, many studies have been conducted showing the interaction between DM and MQ calculations, as for example  $A_{\text{iso}}$  calculations. However, one of the great difficulties inserting a precise combination of these two methods, is how to select MD configurations for the MQ calculations [40]. In this regard, the statistical inefficiency (SI) is a method that has already been successfully used to select the DM configurations [24, 41]. Thus, in the present study one of the methods used to select the MD conformations was the SI. This approach uses the statistically

uncorrelated structures for quantum mechanical calculations by using the energy auto-correlation function from MD simulations [41, 42]. The statistical interval obtained from the energy autocorrelation function,  $C(t)$ , is very important. For a markovian process,  $C(t)$ , follows an exponential decay, Eq. 1, as demonstrated by the Canuto and Coutinho group [24]. The interval between uncorrelated configurations, or the correlation step  $\tau$  (the molecular rotational correlation time in Eq. 2), is calculated by integration of  $C(t)$  from zero to infinity, the variable  $t$  represent the simulation time in picoseconds. The theory shows that configurations separated by  $2\tau$ , or larger intervals, are considered uncorrelated [25]. This exponential decay can be seen in Figure 1.

Equation 1:

$$C(t) = \sum_{i=1}^N C_i e^{-t/\tau_i}$$

Equation 2:

$$\tau = \int_0^{\infty} C(t) dt$$

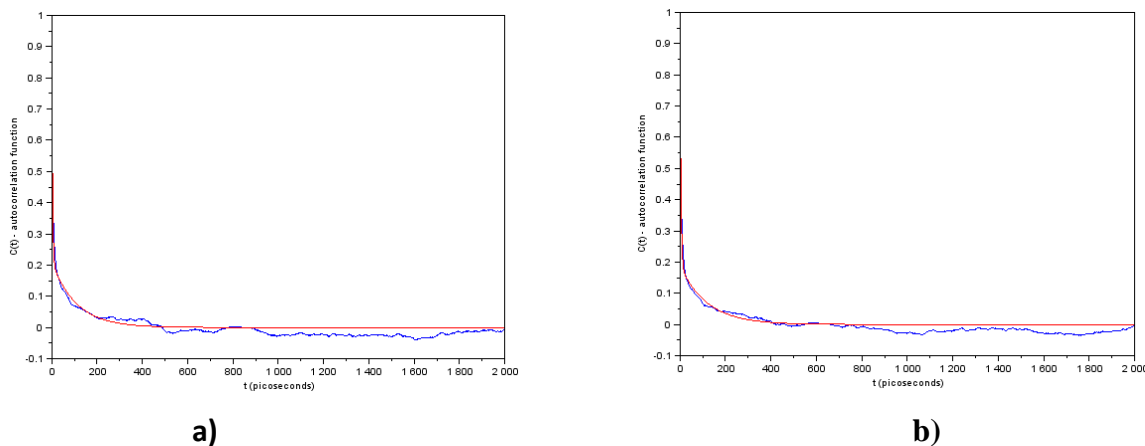


Figure 1- Graph of the auto-correlation function for the time in picoseconds. a)  $[\text{Fe}(\text{H}_2\text{O})_6]$  b)  $\gamma\text{-Fe}_2\text{O}_3$ . The blue curve is the correction and the red curve the adjustment done.



From the MD simulation, the auto-correlation function (Figure 1) was obtained, the correlation times for  $[\text{Fe}(\text{H}_2\text{O})_6]^{2+}$  with water molecules were 24.41 ps and for  $\gamma\text{-Fe}_2\text{O}_3$  it was 25.75ps. The correlation time for both systems were similar, which is to be expected.

### 3.2-The Optimal wavelet signal compression algorithm (OWSCA)

The optimal wavelet-signal compression algorithm (OWSCA) is based on the wavelet analysis [43]. The discrete wavelet transform is a mathematical procedure that converts a signal into a different form. Such conversion reveals the main characteristics hidden within the signal and represents the original signal more succinctly. In this way, a wavelet function is needed in order to realize the wavelet transform.

Basically, the discrete wavelet transform of a given dataset  $x(t)$  can be defined according to Equation 3[44].

Equation 3:

$$d_{j,k} = \int_{-\infty}^{\infty} x(t) \psi_{j,k}(t) dt$$

where  $d_{j,k}$  is the wavelet coefficient,  $t$  is the variable time (normalized between 0 and 1),  $j$  represents the scaling parameter (resolution), which determines the time and frequency resolutions of the scaled wavelet function  $\psi$  and  $k$  represents the shifting parameter, which translates the scaled wavelet along the time axis. Typically  $j$  and  $k$  are correlated, where  $j = 0 \cdots N - 1$  and  $k = 0 \cdots M$ , where  $N$  denotes the maximum resolution and  $M = 2^N - 1$ . In this way,  $\psi_{j,k}$  can be defined by Equation 4:

Equation 4:

$$\psi_{j,k}(t) = \frac{1}{\sqrt{2^j}} \psi\left(\frac{t - k2^j}{2^j}\right)$$

where  $\psi$  is known as the mother wavelet.

The wavelet  $\psi$  can be said to be a “small wave” that has an oscillating wavelike characteristic and has its energy concentrated in time or space. A wavelet function may be irregular in shape, and normally lasts only for a limited period of time. There are several types and families of wavelets whose properties differ along the following principal criteria: (i) convergence speeds when the time tends to 0; (ii) symmetry, (iii) compression potential and (iv) smoothness. One of the advantages of wavelet transform for signal analysis is the abundance of the wavelet functions developed for different purposes, such as Haar, Daubechies, Morlet and Symlets. In this research we have used the Haar wavelet, also known as Daubechies-1, defined according to Equation 5:

Equation 5:

$$\psi_{Haar}(t) = \begin{cases} -1 & 0 \leq t < 0.5 \\ 1 & 0.5 \leq t < 1 \\ 0 & otherwise \end{cases}$$

Haar is the simplest wavelet function and presents a compact support as noticed in Equation 4 but presents a discontinuous profile. This property can, however, be an advantage for the analysis of signals with abrupt (non-smooth) transitions [43]. The discrete wavelet transform, defined by Equation 3, results in a vector of wavelet coefficients,  $\mathbf{d}$ , where  $\mathbf{d} = \{d_{0,0}, d_{0,1}, \dots, d_{N,M}\}$ . Therefore, each wavelet level represents a frequency, or resolution, and has its own coefficients. Generally, the major part of the wavelet coefficients is very small, indicating that they can be removed from  $\mathbf{d}$  without damaging the main characteristics of the original data set. In other words, each  $d_{j,k} < \delta_j$  is removed, where  $\delta_j$  is the threshold of a specific wavelet level  $j$ . This procedure is known as wavelet compression [48]. The major reason for the effectiveness of the wavelet coefficients stems from the ability of wavelets to generally concentrate signal energy in a few significantly nonzero coefficients. In this way, the Optimal Wavelet Signal Compression Algorithm (OWSCA), proposed in the present work, is based on a wavelet compression strategy, in which an optimization algorithm is applied to compress the

maximum number of wavelet coefficients, instead of using heuristically chosen parameters [38]. The OWSCA is summarized in Figure 2:

<b>Description of OWSCA</b>
<p style="text-align: center;"><b>1. Discrete wavelet transform</b></p> $d_{j,k} = \int_{-\infty}^{\infty} x(t) \psi_{j,k}(t) dt, j = 0, \dots, N - 1; k = 0, \dots, 2^N - 1$ <p style="text-align: center;"><b>2. Optimization to find <math>\delta_j^*</math>, <math>j = 0, \dots, N - 1</math></b></p> <p style="text-align: center;"><b>3. Wavelet compression ( for each <math>j</math> )</b></p> $d_{j,k} = 0 \text{ if } d_{j,k} \leq \delta_j^*, j = 0, \dots, N - 1; k = 0, \dots, 2^N - 1$ <p style="text-align: center;"><b>4. Inverse discrete wavelet transform</b></p> $y(t) = \sum_{j=0}^{N-1} \sum_{k=0}^{2^N-1} d_{j,k} \psi_{j,k}(t)$

Figure 2 - The OWSCA is summarized.

In Step 1 of OWSCA the signal  $x(t)$  corresponds to the MD conformations data set, with a dimension equals to 10000 points. Thus, OWSCA aims to compress  $x(t)$  in order to reduce the number of MD conformations to be analyzed. After compression,  $x(t)$  is reduced to  $y(t)$ . In Step 2, an optimization is performed in order to calculate optimum threshold values. Hence, an optimization problem was formulated according to Equation 6:

Equation 6:

$$\mathbf{min} \delta_j \parallel x(t) - y(t) \parallel$$

**s. t.**

$$n_y \leq \mathbf{50}$$

$$d_{j,k} = 0 \text{ if } d_{j,k} \leq \delta_j, j = 0, \dots, N - 1; k = 0, \dots, 2^N - 1$$

$$y(t) = \sum_{j=0}^{N-1} \sum_{k=0}^{2^n-1} d_{j,k} \psi_{j,k}(t)$$

where  $n_y$  is the dimension of the compressed data set  $y(t)$  and  $\|\cdot\|$  is the  $L_2$  norm. Thus, the optimization seeks to perform the compression without damaging the main characteristics of the original data set  $x(t)$ . Notice that both  $x(t)$  and  $y(t)$  can be evaluated at any time. However  $y(t)$  presents a smoother profile according to Haar expansion. In this way,  $n_y$  corresponds to the number of changes observed in the  $y(t)$  profile. It must be said that the  $L_2$  norm takes into account the complete set of points in the original signal and the correspondent ones within the Haar expansion (and not only the ones in the compressed signal). According to Equation 6,  $n_y$  is the constraint of the optimization problem, forcing the maximum number of MD conformations to be 50. Such value has been chosen heuristically, based on our experience of the maximum feasible number of conformations to be simulated. A Genetic Algorithm (GA) [34] was used in this step. Basically, at each GA iteration, different  $\delta_j$  values are tested in order to minimize  $\|x(t) - y(t)\|$ .

In Step 3, the wavelet compression is performed with the optimal threshold values,  $\delta_j^*$ . Finally, Step 4 computes the inverse wavelet transform to obtain  $y(t)$ . After this step, the OWSCA was applied to compress a data set with 7801 points (MD conformations). The comparison between the original data  $x(t)$  and the compressed data  $y(t)$  can be observed in Figure 3. As seen, Figure 3 plots the Energy of MD conformations ( $[\text{Fe}(\text{H}_2\text{O})_6]^{2+}$ ) at each time. We have considered, for this analysis, the period between 40000 and 10000 fs. It was observed that the period of energy decrease (dynamic period) was between 0 fs and 40000 fs. In view of this, such period was excluded from the analysis and the compression was performed only in the stationary phase, where the energy oscillates periodically. It can be observed that the original data set  $x(t)$  presents a high oscillatory (noisy) profile while the compressed data set  $y(t)$ , with  $n_y$  equals to 50, presents a smoother profile not equidistantly spaced. Notice that the trajectory of both curves is similar, meaning that  $y(t)$  captures the main features of  $x(t)$ .

Figure 4 shows the spectrum of wavelet coefficients after of the DWT of  $x(t)$  (for  $[\text{Fe}(\text{H}_2\text{O})_6]^{2+}$ ). As seen, the data set  $x(t)$  was decomposed into 12 wavelet levels,  $j$ . The

amplitude of the coefficients can be visualized in the vertical axis, while the horizontal axis shows the number of points. Notice that lower wavelet levels contain high frequency data while high wavelet levels contain low frequency data. Thus, each level must have a different threshold. According to OSWCA, most of the high frequency coefficients were compressed as shown in Figure 5.

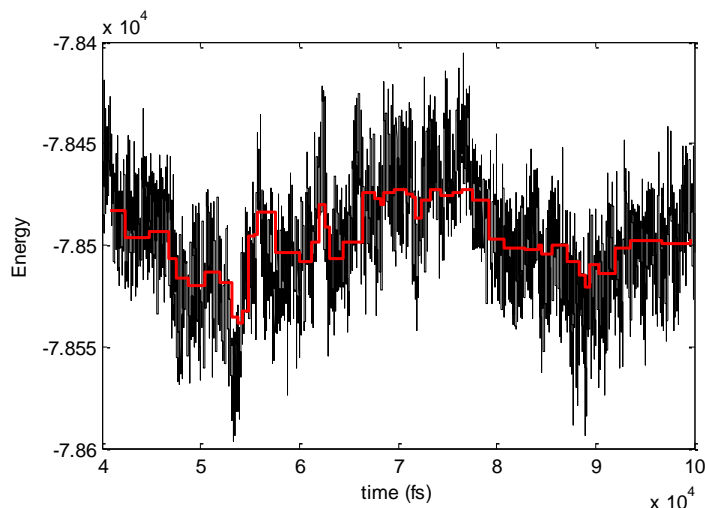


Figure 3 - Energy of MD  $[\text{Fe}(\text{H}_2\text{O})_6]^{2+}$  conformations (original and compressed) at each time (fs).

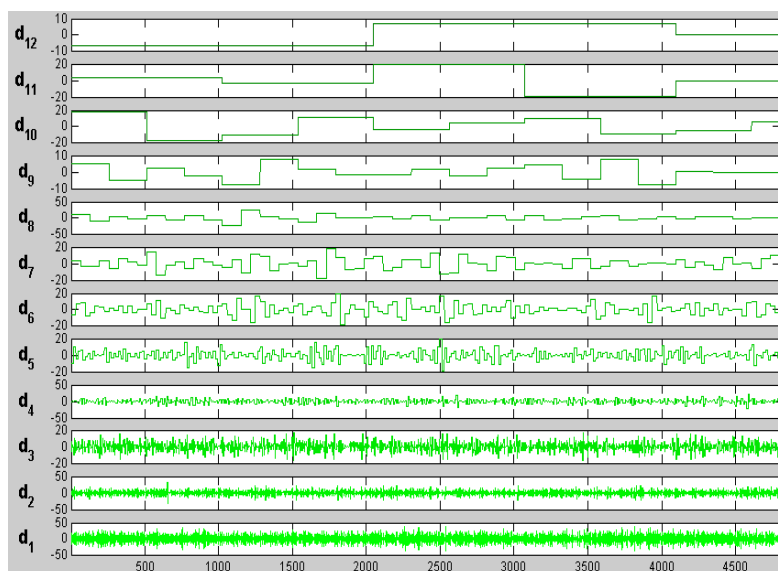


Figure 4 - Wavelet coefficients of  $x(t)$ ,  $[\text{Fe}(\text{H}_2\text{O})_6]^{2+}$ .

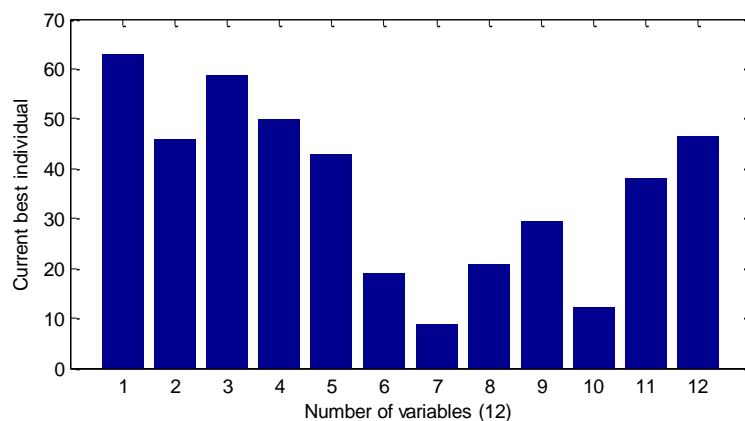


Figure 5 - Optimal thresholds  $\delta_j^*$  (Vertical axis: threshold value; Horizontal axis: individual threshold),  $[\text{Fe}(\text{H}_2\text{O})_6]^{2+}$ .

In order to quantify the precision of the OWSCA procedure, we have computed the residue defined as:

Equation 7:

$$res = \frac{\sqrt{\sum_i (E_i - \bar{E}_i)^2}}{\bar{E}}$$

where  $E_i$  is the  $i$ th MD conformation energy of the original data set  $x(t)$  and  $\bar{E}_i$  is the  $i$ th MD conformation energy of the compressed data set  $y(t)$ , both evaluated at  $i = 1, \dots, n_y$ .  $\bar{E}$  is the average MD conformation energy of the original data set  $x(t)$  evaluated at all points. According to OWSCA results, the computed residue was 0.18 % for  $[\text{Fe}(\text{H}_2\text{O})_6]^{2+}$ . This value is significantly small, considering that the compressed data set has 50 conformations while the original data set has 7801 conformations.

The same OWSCA analysis was performed for  $[\text{Mn}(\text{H}_2\text{O})_6]^{2+}$  and  $[\text{Gd}(\text{H}_2\text{O})_8]^{3+}$ . The residues and number of conformations for  $[\text{Mn}(\text{H}_2\text{O})_6]^{2+}$  were 0.208 % and 49 while 0.210% and 50 conformations for  $[\text{Gd}(\text{H}_2\text{O})_8]^{3+}$ . It should be emphasized that the validation of the OWSCA method was done after theoretical spectroscopic calculations, explained in the next topic.

### 3.3-Statistical Convergence

To assess the \*sampling\* error arising from the OWSCA and SI approaches, one should compare to the DFT result using converged sampling (i.e. using a large number of MD configurations so that the results are statistically converged). Otherwise there may be fortuitous cancellation of errors between the sampling error and the DFT error that one can't tell apart [41]. In this line, the  $[\text{Fe}(\text{H}_2\text{O})_6]^{2+}$  complex has been selected, because it is the simpler system and have experimental values. In this study, the SI and OWSCA methods have been used as the criterion to select conformations from the MD simulation. Thus, in order to check the influence of the number of structures (N) selected from the MD calculation on the  $A_{\text{iso}}$  with the SI and OWSCA method, we changed N and carried out  $A_{\text{iso}}$  calculations with 1, 13, 20 and 40 structures from the MD simulation. According to Figure 6, it can be observed that the absolute error in the  $A_{\text{iso}}$  values decreases sharply with the number of selected conformations from the MD simulation, thus, to structures with  $N < 20$  the error decreases considerably. It is possible to also notice that from 40 structures the error is practically constant, which shows the efficiency of both methods.

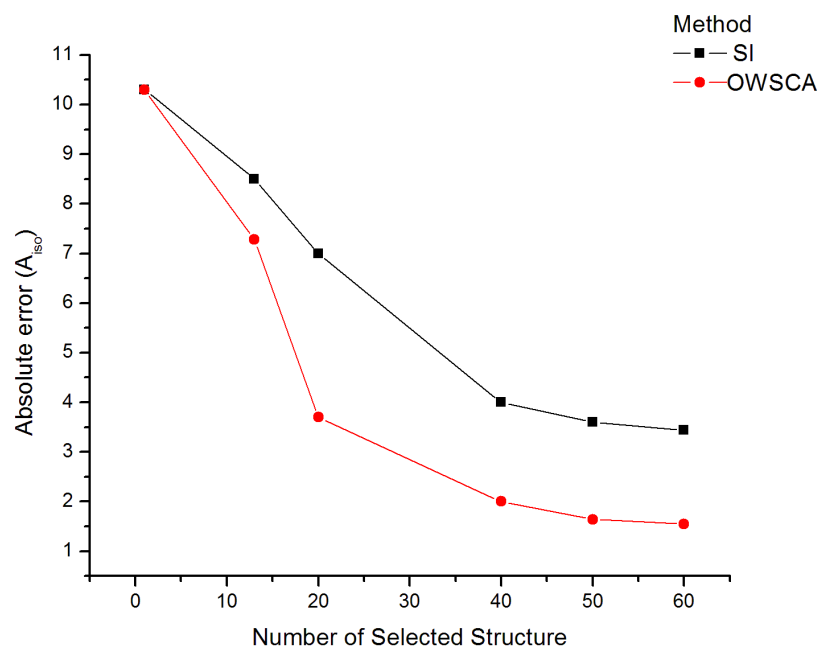


Figure 6 - Number of selected  $[\text{Fe}(\text{H}_2\text{O})_6]^{2+}$  structures versus absolute error for OWSCA and SI methods.

### 3.4-Validating the theoretical strategies by hyperfine coupling constant (HFCCs) calculations

Chemical species with at least one unpaired electron, currently have aroused great interest. This interest has grown tremendously with the increasing understanding of their role in biological systems [45, 46]. An important and powerful technique for the study of these species is the electron paramagnetic resonance (EPR) spectroscopy, having the hyperfine coupling constant ( $A_{\text{iso}}$ ) as a parameter to assess these properties. Thus, the  $A_{\text{iso}}$  calculations are highly dependent on the level of theory and great effort has been made to try to understand the requirements of the theory for an accurate prediction of the HFCC calculations [39, 47]. The choice of the computational methods for  $A_{\text{iso}}$  calculations was based on previous studies in the literature from the Esteban Gomez group [46], which suggests the functional PBE1PBE as the most suitable, as well as Jacob Kongsted's group [48, 49], which suggested the basis set aug-cc-pVTZ-J for  $A_{\text{iso}}$  values of  $^1\text{H}$  and  $^{17}\text{O}$  atoms due to satisfactory results. Iron oxide nanoparticles affect the HFCCs and consequently the relaxation time  $T_2$  and  $T_2^*$ . Equation 8 and 9 shows the transverse relaxation time ( $T_1$  and  $T_2$ ). The transverse relaxation time depends on the electron spin ( $S$ ), the electronic and proton  $g$  factors ( $g_e$  and  $g_N$ , respectively), the Bohr magneton ( $\beta$ ), the nuclear magneton ( $\beta_N$ ), the hyperfine coupling constant ( $A$ ), the ion-nucleus distance ( $r$ ), the Larmor frequencies for the proton and electron spins ( $\omega_I$  and  $\omega_S$ ), and the correlation times  $\tau_c$  and  $\tau_e$  are characteristic of the rate of change of the interactions between the metallic species and neighboring protons [39].

Equation 8:

$$R_1 = \frac{1}{T_1} \cong \frac{1}{15} \frac{S(S+1)g_e^2\beta^2g_N^2\beta_N^2}{\hbar^2r^6} + \left(\frac{A}{\hbar}\right)^2 \frac{S(S+1)}{3} \left[\frac{2\tau_e}{1+(\omega_I\tau_e)^2}\right]$$

Equation 9:

$$R_2 = \frac{1}{T_2} \cong \frac{1}{15} \frac{S(S+1)g_e^2\beta^2g_N^2\beta_N^2}{h^2r^6} + \left(\frac{A}{\hbar}\right)^2 \frac{S(S+1)}{3} \left[\tau_c + \frac{\tau_c}{1+(\omega_S\tau_e)^2}\right]$$



In this work, we carried out a prediction of transverse relaxation time by the hyperfine coupling constant calculations, in fact is the most sensitive variable of Equation 8 and 9. The hyperfine coupling constant depends on three contributions, which are the isotropic Fermi contact (FC) and the anisotropic spin–dipolar contributions and the spin–orbit contribution. Thus, the focus of this work is on the Fermi Contact (FC) contribution, which is obtained through nonrelativistic HFCC calculations that are necessary for this type of system. The contribution of  $A_{\text{iso}}$  is represented by Equation 10 [7].

Equation 10:

$$A_{\text{iso}} = \frac{4\pi}{3} \beta_e \beta_N g_e g_N \langle S_Z \rangle^{-1} \rho_N^{\alpha-\beta}$$

where  $\beta_N$  and  $\beta_e$  are the nuclear and Bohr magnetons, respectively,  $g_N$  and  $g_e$  are nuclear and free-electron  $g$  values,  $S$  is the total electron spin of the system, and  $\rho_N^{\alpha-\beta}$  represents the difference between majority spin ( $\alpha$ ) and minority spin ( $\beta$ ) densities at the position of the nucleus  $N$  [7]. Initially, the theoretical strategy was validated with  $A_{\text{iso}}$  calculations of  $\text{Fe}^{2+}$  atoms of the  $[\text{Fe}(\text{H}_2\text{O})_6]^{2+}$  complex. In our calculations, we assume the spin state with the lowest energy [50, 51] for  $[\text{Fe}(\text{H}_2\text{O})_6]^{2+}$  as well as for  $[\text{Gd}(\text{H}_2\text{O})_8]^{3+}$ , and  $[\text{Mn}(\text{H}_2\text{O})_6]^{2+}$ . In this context, some DFT functionals were evaluated for the  $A_{\text{iso}}$  calculation. Our findings point out that PBE1PBE data are in the best agreement with the experimental results. This conclusion is also according to previous works for similar systems [17, 23]. After defining the functional,  $A_{\text{iso}}$  calculations were carried out for  $[\text{Fe}(\text{H}_2\text{O})_6]^{2+}$ ,  $[\text{Gd}(\text{H}_2\text{O})_8]^{3+}$  and  $[\text{Mn}(\text{H}_2\text{O})_6]^{2+}$  complexes by applying the OWSCA method, the results are reported in Table 1 and 2. Initially, it was analyzed the  $[\text{Fe}(\text{H}_2\text{O})_6]^{2+}$  complex and from our theoretical findings a difference of 0.01 MHz was obtained between structures with the explicit solvent ( $(A_{\text{iso}}^{\text{eq}}(\text{PBE1PBE}(\text{H}_2\text{O})//\text{PBE1PBE}(\text{H}_2\text{O})))$  and explicit/implicit solvent ( $(A_{\text{iso}}^{\text{eq}}(\text{PBE1PBE}(\text{H}_2\text{O})/\text{PCM}/\text{PBE1PBE}(\text{H}_2\text{O})))$ ), which is not so significant. Considering now the thermal and solvent effects on the  $A_{\text{iso}}$  calculations ( $(A_{\text{iso}}^{300\text{K}}(\text{MD}(\text{H}_2\text{O})//\text{MD}(\text{H}_2\text{O})))$ ), a value of 0.46 and 0.48 MHz were obtained by the SI and OWSCA selection methods, respectively. In this perspective, our results highlight that the thermal and solvent effects play important roles and greatly influence the  $A_{\text{iso}}$  values. Whereas

the SI and OWSCA methods are efficient selection methods for MD simulations, configurations from the OWSCA method leads to a slight good agreement with experimental  $A_{\text{iso}}$  values. From the data, a good performance of the OWSCA method was observed, which could lead to similar results from the SI method, which is considered a consolidated method in the literature for selection of MD or MC configurations [24, 25, 42]. It is also worth noting that the SI method takes the statistically uncorrelated configurations in equally spaced time intervals, however, the OWSCA method employed in the present work uses time instants that are not equally spaced, evidencing great flexibility in optimization analysis, which can, in some cases, lead to more satisfactory results. Furthermore, there are other advantages to using the wavelet transform instead of other mathematical procedures, such as the Fourier transform. Despite both wavelet and Fourier transforms being able to detect the dominant frequencies in the signals, the wavelets are more efficient in dealing with time-frequency analysis [52]. In fact, the wavelet transform can map each function to its coefficients with respect to this basis. In addition, the mathematics used is simpler and faster than in the Fourier transform [26, 52].

**Table 1:**  $A_{\text{iso}}$  values of  $\text{Fe}^{2+}$  atoms of selected  $[\text{Fe}(\text{H}_2\text{O})_6]^{2+}$  structures by optimal wavelet signal compression algorithm (OWSCA) and statistical inefficiency (SI) Methods.

$[\text{Fe}(\text{H}_2\text{O})_6]^{2+}$	$A_{\text{iso}}(\text{MHz})$	
	SI	OWSCA
$A_{\text{iso}}^{\text{eq}}$ (PBE1PBE( $\text{H}_2\text{O}$ )/PBE1PBE( $\text{H}_2\text{O}$ ))	0.43	
$A_{\text{iso}}^{\text{eq}}$ (PBE1PBE ( $\text{H}_2\text{O}$ )/PCM//PBE1PBE( $\text{H}_2\text{O}$ ))	0.42	
$A_{\text{iso}}^{300\text{K}}$ (MD( $\text{H}_2\text{O}$ )/MD( $\text{H}_2\text{O}$ ))	0.46	0.48
<i>Experimental</i>	0.50	

In an attempt to validate our OWSCA methodology even more, theoretical  $A_{\text{iso}}$  calculations were performed with  $[\text{Gd}(\text{H}_2\text{O})_8]^{3+}$  and  $[\text{Mn}(\text{H}_2\text{O})_6]^{2+}$  complexes using the SI and OWSCA methods. For  $[\text{Gd}(\text{H}_2\text{O})_8]^{3+}$ , the  $A_{\text{iso}}$  values with the explicit solvent ( $A_{\text{iso}}^{\text{eq}}$  (PBE1PBE(H<sub>2</sub>O)//PBE1PBE(H<sub>2</sub>O))) were 1.22 and 2.34 MHz for <sup>1</sup>H and <sup>17</sup>O atoms, respectively. Now, with the explicit and implicit solvent ( $A_{\text{iso}}^{\text{eq}}$  (PBE1PBE (H<sub>2</sub>O)/PCM//PBE1PBE(H<sub>2</sub>O))), the values were of 1.13 and 2.59 MHz for the <sup>1</sup>H and <sup>17</sup>O atoms, respectively. Taking into account the thermal effects, for the SI method, the values of 1.04 and 2.84 MHz were obtained for the <sup>1</sup>H and <sup>17</sup>O atoms. On the other hand, for the OWSCA method, the values of 1.01 and 2.49 MHz were obtained for <sup>1</sup>H and <sup>17</sup>O atoms, respectively. For the  $[\text{Mn}(\text{H}_2\text{O})_6]^{2+}$  complex with the explicit solvent ( $A_{\text{iso}}^{\text{eq}}$  (PBE1PBE(H<sub>2</sub>O)//PBE1PBE(H<sub>2</sub>O))) the values 1.34 and 4.95 MHz were computed for the <sup>1</sup>H and <sup>17</sup>O atoms, while with the explicit and implicit solvent ( $A_{\text{iso}}^{\text{eq}}$  (PBE1PBE (H<sub>2</sub>O)/PCM//PBE1PBE(H<sub>2</sub>O))), the values of 1.25 and 4.55 MHz for the <sup>1</sup>H and <sup>17</sup>O atoms were observed, respectively. For the SI method, the theoretical values with the thermal effects ( $A_{\text{iso}}^{300\text{K}}$  (MD(H<sub>2</sub>O)//MD(H<sub>2</sub>O))) were of 1.04 MHz for the <sup>1</sup>H atoms and 5.50 MHz for the <sup>17</sup>O atoms, however, for the OWSCA method, the values were of 0.93 and 5.35 MHz for the <sup>1</sup>H and <sup>17</sup>O atoms, respectively. Thus, it is possible to notice that for both complexes, a better agreement with the experimental available data can be observed with the OWSCA method.

**Table 2:**  $A_{\text{iso}}$  values of  $^1\text{H}$  and  $^{17}\text{O}$  atoms of selected  $[\text{Gd}(\text{H}_2\text{O})_8]^{3+}$  and  $[\text{Mn}(\text{H}_2\text{O})_6]^{2+}$  structures by optimal wavelet signal compression algorithm (OWSCA) and statistical inefficiency (SI) Methods.

	$A_{\text{iso}}(\text{MHz})$							
	$[\text{Gd}(\text{H}_2\text{O})_8]^{3+}$				$[\text{Mn}(\text{H}_2\text{O})_6]^{2+}$			
	$^1\text{H}$		$^{17}\text{O}$		$^1\text{H}$		$^{17}\text{O}$	
	SI	OWSCA	SI	OWSCA	SI	OWSCA	SI	OWSCA
$A_{\text{iso}}^{\text{eq}}(\text{PBE1PBE}(\text{H}_2\text{O})//\text{PBE1PBE}(\text{H}_2\text{O}))$	1.22		2.34		1.34		4.95	
$A_{\text{iso}}^{\text{eq}}(\text{PBE1PBE}(\text{H}_2\text{O})/\text{PCM}/\text{PBE1PBE}(\text{H}_2\text{O}))$	1.13		2.59		1.25		4.55	
$A_{\text{iso}}^{300\text{K}}(\text{MD}(\text{H}_2\text{O})//\text{MD}(\text{H}_2\text{O}))$	1.04	1.01	2.84	2.49	1.04	0.93	5.50	5.35
<i>Experimental</i>	$0.84^5$		-		$0.86^{61}$		$5.40^{61}$	

### 3.5-QTAIM, spin density distribution analysis, thermal and solvent effects on the $\gamma\text{-Fe}_2\text{O}_3$

Turning now to our proposal of a new contrast agent ( $\gamma\text{-Fe}_2\text{O}_3$ ), which is reported in Table 3. By analyzing the results, differences of only 0.02 MHz for hydrogen atoms and 0.01 MHz for oxygen atoms were observed for the structures with the explicit ( $(A_{\text{iso}}^{\text{eq}}(\text{PBE1PBE}(\text{H}_2\text{O})//\text{PBE1PBE}(\text{H}_2\text{O})))$  and explicit/implicit solvent ( $(A_{\text{iso}}^{\text{eq}}(\text{PBE1PBE}(\text{H}_2\text{O})/\text{PCM}/\text{PBE1PBE}(\text{H}_2\text{O})))$ ), which is a not relevant. For the equilibrium structure with explicit and implicit solvent ( $(A_{\text{iso}}^{\text{eq}}(\text{PBE1PBE}(\text{H}_2\text{O})/\text{PCM}/\text{PBE1PBE}(\text{H}_2\text{O})))$ ), the  $A_{\text{iso}}$  value was of 3.16 MHz for the  $^1\text{H}$  atoms and 4.55 MHz for the  $^{17}\text{O}$  atoms. Thus, a difference between explicit solvent and implicit /explicit is 0.06 MHz and 0.19 MHz for the  $^1\text{H}$  and  $^{17}\text{O}$  atoms was obtained, respectively. Turing now to the influence of thermal effects ( $(A_{\text{iso}}^{300\text{K}})$

((MD(H<sub>2</sub>O)//MD(H<sub>2</sub>O))), the  $A_{\text{iso}}$  values are 3.85 MHz and 3.99 MHz for the <sup>1</sup>H and <sup>17</sup>O, respectively. Thus, the thermal effects should be taken into consideration as they greatly influence the system.

**Table 3:**  $A_{\text{iso}}$  values for  $\gamma\text{-Fe}_2\text{O}_3$  of the selected structures by optimal wavelet signal compression algorithm (OWSCA).

$\gamma\text{-Fe}_2\text{O}_3$	$A_{\text{iso}}(\text{MHz})$	
	<sup>1</sup> H	<sup>17</sup> O
$A_{\text{iso}}^{\text{eq}}(\text{PBE1PBE}(\text{H}_2\text{O})//\text{PBE1PBE}(\text{H}_2\text{O}))$	3.14	4.54
$A_{\text{iso}}^{\text{eq}} \text{PBE1PBE}(\text{H}_2\text{O})/\text{PCM}//\text{PBE1PBE}(\text{H}_2\text{O})$	3.16	4.55
$A_{\text{iso}}^{300\text{K}}(\text{MD}(\text{H}_2\text{O})//\text{MD}(\text{H}_2\text{O}))$	3.85	3.99

The use of implicit solvent does not influence the  $A_{\text{iso}}$  values of our system, in both cases ( $[\text{Fe}(\text{H}_2\text{O})_6]^{2+}$  and  $\gamma\text{-Fe}_2\text{O}_3$ ). In this approach, the thermal effects ((MD(H<sub>2</sub>O)//MD(H<sub>2</sub>O))) were very important to the system, thus, the MD and thermal effects are fundamental to a more realistic understanding of the system. It has also been observed that for all cases analyzed the <sup>17</sup>O is more sensitive than <sup>1</sup>H to  $A_{\text{iso}}$  parameters, what was expected. The quantum theoretical methods developed by Richard Bader [53] has shown to be a clear and efficient tool to identify and characterize the interactions of a intra/intermolecular nature, as well as to also check how atoms behave when covalent or unsaturated bond formation occurs [54, 55]. Thus, the QTAIM calculations were carried out in order to verify the nature of the chemical bond and the influence of hydrogen bonds on the  $A_{\text{iso}}$  values. From the parameters proposed by Koch and Popelier [56], a hydrogen bond is characterized by the decrease of the values  $M_1(\text{H})$  and  $V(\text{H})$ , as well as the increase of  $q(\text{H})$  and  $E(\text{H})$ . Thus, it can be seen from Tables 3 and 4, that both compounds studied ( $[\text{Fe}(\text{H}_2\text{O})_6]^{2+}$  and  $\gamma\text{-Fe}_2\text{O}_3$ ) satisfy these parameters. In other words, in

the hydrogen bonds between the water molecules the oxygen atoms of the  $[\text{Fe}(\text{H}_2\text{O})_6]$  and of  $\gamma\text{-Fe}_2\text{O}_3$ , are able to significantly increase the  $A_{\text{iso}}$  values.

**Table 4:** Additional atomic properties obtained by QTAIM calculations for hydrogen bonded atoms (in au) of  $[\text{Fe}(\text{H}_2\text{O})_6]^{2+}$ .

Structure	$q(\mathbf{H})$	$M_1(\mathbf{H})$	$V(\mathbf{H})$	$E(\mathbf{H})$
<b>1<sub>H(OH)</sub></b>	+0.438209	+0.202219	+31.913500	-0.418842
<b>2<sub>H(a)···O(a)</sub></b>	+0.535203	+0.186412	+26.051455	-0.373193

**Table 5:** Additional atomic properties obtained by QTAIM calculations for hydrogen bonded atoms (in au) of the  $\gamma\text{-Fe}_2\text{O}_3$ .

Structure	$q(\mathbf{H})$	$M_1(\mathbf{H})$	$V(\mathbf{H})$	$E(\mathbf{H})$
<b>1<sub>H(OH)</sub></b>	+0.508138	+0.169063	+24.845773	-0.400389
<b>2<sub>H(a)···O(a)</sub></b>	+0.514241	+0.148394	+21.396720	-0.384766

The Table 6 shows the values of the parameters analyzed. 1a and 1b are the analyzed interactions for the  $[\text{Fe}(\text{H}_2\text{O})_6]^{2+}$  and 2a 2b and 2 are the  $\gamma\text{-Fe}_2\text{O}_3$  (the atoms are specified in Figure 7). According to the Koch and Popelier parameter, the atoms in **1a**, **1b**, **2a** and **2c** possess  $\nabla^2\rho(r) > 0$  and  $H(r) > 0$  suggesting partial covalent interactions, the specified atoms in 2b possess  $\nabla^2\rho(r) < 0$  and  $H(r) < 0$  suggesting covalent interactions, the values of ellipticity ( $\epsilon$ ) (parameter used to describe the character of the chemical bond) were reasonably high which features a  $\pi$  binding character, characterizing the hydrogen bonds, these interactions can actually influence the  $A_{\text{iso}}$  values and the system stabilization. From the rigorous concepts of QTAIM, the BCPs (bond critical points) are located on hydrogen bonds formed by proton donors and  $\pi$  electrons, Figure 7 (**1b** and **2b**) [57, 58], thus the low  $\rho(r)$  values along with the positive results of the

Laplacian ( $\nabla^2\rho(r)$ ) indicate the formation of hydrogen bonds in each BCP intermolecular. Thus, when water molecules in the system with  $\gamma\text{-Fe}_2\text{O}_3$  are added, there are interactions of free water molecules with the oxygen (**HO...H**) and iron (**HO...Fe**) of  $\gamma\text{-Fe}_2\text{O}_3$ . It was also observed that some water molecules are broken and bind on the surface of  $\gamma\text{-Fe}_2\text{O}_3$ , further stabilizing the system.

**Table 6:** QTAIM parameters obtained at the hydrogen bond BCPs for the structures of **1-2**(au) (Structures: 1:  $[\text{Fe}(\text{H}_2\text{O})_6]^{2+}$  with water and 2:  $\gamma\text{-Fe}_2\text{O}_3$  with water molecules).

Structure	$\rho(r)$	$\nabla^2\rho(r)$	$\epsilon$	$V(r)$	$G(r)$	$H(r)$
<b>1a</b> <sub>(Oa...Ha)</sub>	+0.016478	+0.051291	+0.024445	-0.013511	+0.013167	-0.000344
<b>1b</b> <sub>(Ob...Hb)</sub>	+0.026654	+0.094203	+0.100450	-0.024452	+0.024001	-0.000451
<b>2a</b> <sub>(Oa...Ha)</sub>	+0.012580	+0.044821	+0.236350	-0.010046	+0.010626	-0.000580
<b>2b</b> <sub>(Ob...Hb)</sub>	+0.294317	-1.330915	+0.023039	-0.447893	+0.057582	-0.390311
<b>2c</b> <sub>(Fea...Oc)</sub>	+0.225673	+1.633337	+0.068607	-0.570257	+0.489296	-0.080961

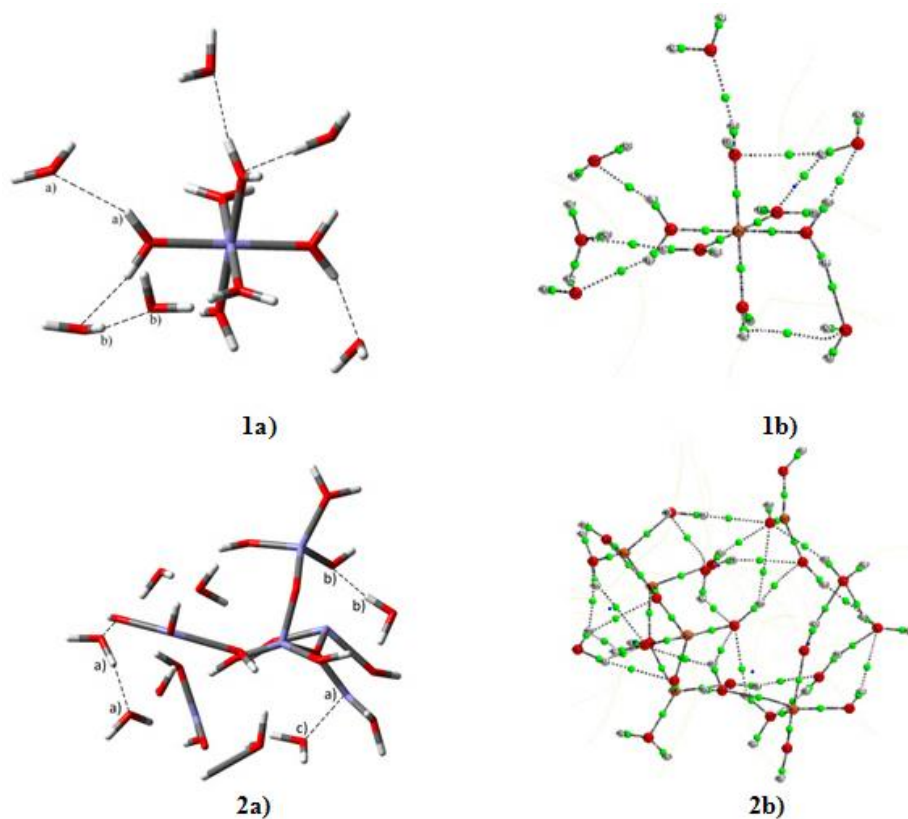


Figure 7 - a)  $[\text{Fe}(\text{H}_2\text{O})_6]^{2+}$  and  $\gamma\text{-Fe}_2\text{O}_3$  structures with water molecules, b) bond critical points (BCP).

The distribution of the spin density in a given paramagnetic molecule indicates the contributions due to electrons with the majority spin ( $\alpha$ ) and the minority spin ( $\beta$ ) [6, 59]. In general,  $\alpha$  spin density represents from where electrons are coming and the  $\beta$  spin density, to where the electrons are going. In Figure 8 these regions are represented by the colors blue (spin  $\alpha$ ) and green (spin  $\beta$ ). We observed that for the iron complex,  $[\text{Fe}(\text{H}_2\text{O})_6]^{2+}$ , there is a high negative spin density around the free water molecules and a high density of positive spin around the metal. There is a transfer of electrons of the metal to the water molecules, which indeed could explain the higher  $A_{\text{iso}}$  values around the water molecules. For the  $\gamma\text{-Fe}_2\text{O}_3$  a high density of positive and negative spin around the iron and oxygen atoms of the oxide is observed and this shows that the  $\gamma\text{-Fe}_2\text{O}_3$  atoms are donating and receiving electrons at the same time. This movement of electrons around of the system may also increase  $A_{\text{iso}}$  values around the water molecules.



Thus, the molecular orbitals hosting the unpaired electrons (SOMOs) in both systems must have a major contribution from the metal “d” orbitals, but a combination with the atomic orbitals of the ligands is expected, particularly from donor atoms like oxygen and iron. The high density of negative spin around the complex and iron oxide can be attributed to a weak spin-polarization effect that changes the signal density. Thus, it should be kept in mind that the  $A_{\text{iso}}$  values of  $^1\text{H}$  and  $^{17}\text{O}$  results of the hyperfine coupling of electron spin and nucleus, therefore, only reflect the spin density of the unpaired with orbital n.

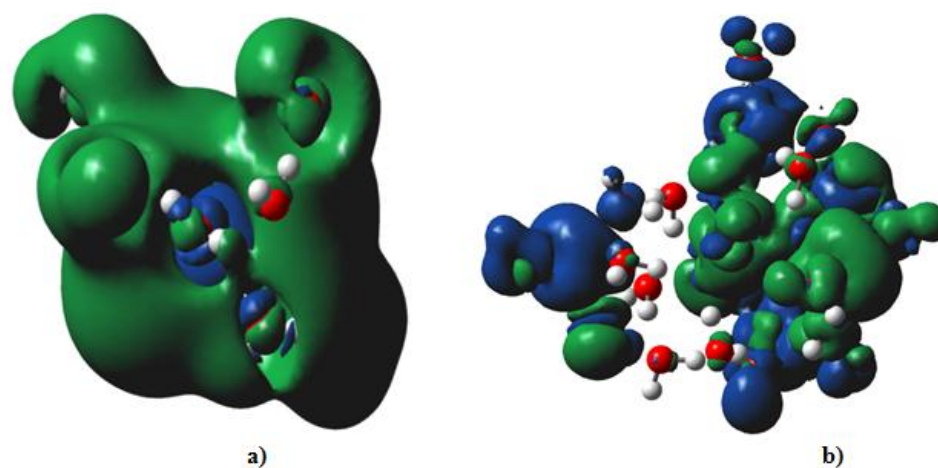


Figure 8 - Spin-density map of the compounds (the isosurface contour value is 0.0004). a)  $[\text{Fe}(\text{H}_2\text{O})_6]^{2+}$  with water molecules b)  $\gamma\text{-Fe}_2\text{O}_3$  with water molecules.

#### 4-Conclusions

From our findings,  $\gamma\text{-Fe}_2\text{O}_3$  possesses longer relaxation times ( $T_1$  and  $T_2$ ) due to both higher changes of  $A_{\text{iso}}$ , compared to the  $A_{\text{iso}}$  values  $[\text{Gd}(\text{DOTA})(\text{H}_2\text{O})]^-$  (experimental value 0.590 MHz [60]), because  $\text{Gd}^{+3}$  complexes have been widely used in the last decades [61, 62] as contrast agents. In this perspective, maghemite can be used as a promising contrast agent. From the theoretical side, the results with the solvent effects are significantly better than results from the optimization in vacuum, showing the convenience of including this effect in the hyperfine coupling constants calculations. It is also important to mention that configurations from the OWSCA method leads to a slight good agreement with experimental  $A_{\text{iso}}$  values for  $[\text{Mn}(\text{H}_2\text{O})_6]^{2+}$  and  $[\text{Gd}(\text{H}_2\text{O})_8]^{3+}$  complexes. Furthermore our theoretical findings highlight that

the thermal and solvent effects play important roles and greatly influence the  $A_{\text{iso}}$  values. Thus, from our results, the SI and OWSCA methods are efficient selection methods for MD simulations.

Herein, a new application based on wavelet analysis was developed and validated for selection of conformations from MD simulations, including, in this way, the thermal and solvent effects on the spectroscopic properties of MRI probes. It is important to stress that the dynamic contribution should be accounted for by selecting an appropriate ensemble of statistically independent conformations, which can be reached by both SI or OWSCA methods. The OWSCA method contains four steps, (i) the discrete wavelet transform of the original MD data, allowing a more precise evaluation of the MD conformations profiles; (ii) optimization of compression parameters. This step is crucial because an optimization procedure is conducted, allowing to select the best MD conformations which represent the most significant part of the dataset. (iii) Wavelet compression and (iv) inverse discrete wavelet transform, resulting in a lower number of MD conformations. In this way, the configuration generated in the simulation can be drastically reduced without loss of statistical information. To our knowledge, this is the first application of this methodology to spectroscopic parameters in the condensed phase

## **5-Acknowledgements**

The authors thank the Brazilian agencies FAPEMIG, CAPES, and CNPq for the financial support of this research the UFLA and UFF for infrastructure and encouragement in this work. This work was also supported by Excellence project FIM.

## **6-References**

1. Telegrafo M, Rella L, Stabile Ianora AA, et al (2015) Unenhanced breast MRI (STIR, T2-weighted TSE, DWIBS): An accurate and alternative strategy for detecting and differentiating breast lesions. *Magn Reson Imaging* 33:951–955. doi: 10.1016/j.mri.2015.06.002
2. Chaudhuri S, Basu K, Sengupta B, et al (2008) Ground- and excited-state proton transfer

- and antioxidant activity of 3-hydroxyflavone in egg yolk phosphatidylcholine liposomes: Absorption and fluorescence spectroscopic studies. *Luminescence* 23:397–403. doi: 10.1002/bio.1052
3. de Angelis C, Brizzi RF, Pellicano R (2013) Endoscopic ultrasonography for pancreatic cancer: current and future perspectives. *World J Gastrointest Oncol* 4:220–230. doi: 10.3978/j.issn.2078-6891.2013.002
  4. Mancini DT, Sen K, Barbatti M, et al (2015) Excited-State Proton Transfer Can Tune the Color of Protein Fluorescent Markers. *ChemPhysChem* 16:3444–3449. doi: 10.1002/cphc.201500744
  5. Esteban-Gómez D, de Blas A, Rodríguez-Blas T, et al (2012) Hyperfine coupling constants on inner-sphere water molecules of Gd(III)-based MRI contrast agents. *Chemphyschem* 13:3640–50. doi: 10.1002/cphc.201200417
  6. Patinec V, Rolla GA, Botta M, et al (2013) Hyperfine coupling constants on inner-sphere water molecules of a triazacyclononane-based Mn(II) complex and related systems relevant as MRI contrast agents. *Inorg Chem* 52:11173–11184. doi: 10.1021/ic4014366
  7. Klug G, Kampf T, Bloemer S, et al (2010) Intracellular and extracellular T1 and T2 relaxivities of magneto-optical nanoparticles at experimental high fields. *Magn Reson Med* 64:1607–1615. doi: 10.1002/mrm.22557
  8. Werner EJ, Datta A, Jocher CJ, Raymond KN (2008) High-relaxivity MRI contrast agents: where coordination chemistry meets medical imaging. *Angew. Chem Int Ed (English)* 47:8568–80. doi: 10.1002/anie.200800212
  9. Perazella MA (2009) Current status of gadolinium toxicity in patients with kidney disease. *Clin J Am Soc Nephrol* 4:461–9. doi: 10.2215/CJN.06011108
  10. Yoffe S, Leshuk T, Everett P, Gu F (2013) Superparamagnetic Iron Oxide Nanoparticles (SPIONs): Synthesis and Surface Modification Techniques for use with MRI and Other Biomedical Applications. *Curr Pharm Des* 19:493–509. doi: 10.2174/1381612811306030493

11. Sun C, Lee JSH, Zhang M (2008) Magnetic nanoparticles in MR imaging and drug delivery. *Adv Drug Deliv Rev* 60:1252–1265. doi: 10.1016/j.addr.2008.03.018
12. Schwarz S, Fernandes F, Sanroman L, et al (2009) Synthetic and biogenic magnetite nanoparticles for tracking of stem cells and dendritic cells. *J Magn Magn Mater* 321:1533–1538. doi: 10.1016/j.jmmm.2009.02.081
13. Jung H, Park B, Lee C, et al (2014) Dual MRI T1 and T2(\*) contrast with size-controlled iron oxide nanoparticles. *Nanomedicine* 10:1679–1689. doi: 10.1016/j.nano.2014.05.003
14. Oliveira, LCA; Fabris. JD; Pereira MC (2013) Óxidos de ferro e suas aplicações em processos catalíticos: uma revisão. *Quim Nova* 36:123–130.
15. Ghose SK, Waychunas GA, Trainor TP, Eng PJ (2010) Hydrated goethite ( $\alpha$ -FeOOH) (100) interface structure: Ordered water and surface functional groups. *Geochim Cosmochim Acta* 74:1943–1953. doi: 10.1016/j.gca.2009.12.015
16. Oliveira LCA, Ramalho TC, Gonçalves M, et al (2007) Pure niobia as catalyst for the oxidation of organic contaminants: Mechanism study via ESI-MS and theoretical calculations. *Chem Phys Lett* 446:133–137. doi: 10.1016/j.cplett.2007.08.037
17. Grau-Crespo R, Al-Baitai AY, Saadoun I, de Leeuw NH (2010) Vacancy ordering and electronic structure of  $\gamma$ -Fe<sub>3</sub>O<sub>4</sub> (maghemite): a theoretical investigation. *J Phys Condens Matter* 22:255401. doi: 10.1088/0953-8984/22/25/255401
18. Gonçalves MA, da Cunha EFF, Peixoto FC, Ramalho TC (2015) Probing thermal and solvent effects on hyperfine interactions and spin relaxation rate of  $\delta$ -FeOOH(100) and [MnH<sub>3</sub>buea(OH)]<sub>2</sub><sup>-</sup>: Toward new MRI probes. *Comp Theor Chem* 1069:96–104. doi: 10.1016/j.comptc.2015.07.006
19. Gonçalves MA, Peixoto FC, da Cunha EFF, Ramalho TC (2014) Dynamics, NMR parameters and hyperfine coupling constants of the Fe<sub>3</sub>O<sub>4</sub>(100)–water interface: Implications for MRI probes. *Chem Phys Lett* 609:88–92. doi: 10.1016/j.cplett.2014.06.030

20. Rapaport DC (2004) *The art of molecular dynamics simulation*. Cambridge University Press, Cambridge
21. van der Wijst T, Fonseca Guerra C, Swart M, et al (2009) Rare Tautomers of 1-Methyluracil and 1-Methylthymine: Tuning Relative Stabilities through Coordination to Pt II Complexes. *Chem Eur J* 15:209–218. doi: 10.1002/chem.200801476
22. Mancini DT, Souza EF, Caetano MS, Ramalho TC (2014) <sup>99</sup>Tc NMR as a promising technique for structural investigation of biomolecules: theoretical studies on the solvent and thermal effects of phenylbenzothiazole complex. *Magn Reson Chem* 52:129–37. doi: 10.1002/mrc.4043
23. Tachikawa H (2002) Ab initio molecular dynamics (MD) calculations of hyperfine coupling constants of methyl radical. *Chem Phys Lett* 352:113–119. doi: 10.1016/S0009-2614(01)01427-0
24. Coutinho K, Georg HCC, Fonseca TLL, et al (2007) An efficient statistically converged average configuration for solvent effects. *Chem Phys Lett* 437:148–152. doi: 10.1016/j.cplett.2007.02.012
25. Coutinho K, Canuto S, Zerner MC (2000) Monte Carlo-quantum mechanics study of the solvatochromic shifts of the lowest transition of benzene. *J Chem Phys* 112:9874–9880. doi: 10.1063/1.481624
26. Schroder P (1995) Wavelets for computer graphics: a primer. *IEEE Comput Graph Appl. Mag* 15:76–84. doi: 10.1109/38.376616
27. Domingues MO, Gomes SM, Cortina E (1995) Biorthogonal wavelets applied to meteorological satellite images (METEOSAT) image compressing. In: Szu HH (ed). pp 726–733
28. Ducla-Soares JL, Santos-Bento M, Laranjo S, et al (2007) Wavelet analysis of autonomic outflow of normal subjects on head-up tilt, cold pressor test, Valsalva manoeuvre and deep breathing. *Exp Physiol* 92:677–686. doi: 10.1113/expphysiol.2007.038026
29. Domingues MO, Mendes O, da Costa AM (2005) On wavelet techniques in atmospheric

- sciences. *Adv Space Res* 35:831–842. doi: 10.1016/j.asr.2005.02.097
30. Jørgensen JE, Mosegaard L, Thomsen LE, et al (2007) Formation of  $\gamma$ -Fe<sub>2</sub>O<sub>3</sub> nanoparticles and vacancy ordering: An in situ X-ray powder diffraction study. *J Solid State Chem* 180:180–185. doi: 10.1016/j.jssc.2006.09.033
  31. Baerends EJ, Autschbach J, Bashford D, Bérces A, Bickelhaupt FM, Bo C, Boerrigter PM, Cavallo L, Chong DP, Deng L, et al (2009) ADF2009.01. 2009.
  32. Frisch MJ, Trucks GW, Schlegel HB, et al Gaussian 09.
  33. Duin V (2002) ReaxFF User Manual.
  34. Aryanpour M, Duin ACTV, Kubicki JD (2013) Development of a reactive force field for iron-oxyhydroxide systems. *J Phys Chem A* 21:6298–6307
  35. Rolla GA, Iglesias CP, Botta M, Tei L, Helm L (2013) <sup>1</sup>H and <sup>17</sup>O NMR relaxometric and computational study on macrocyclic Mn(II) complexes. *Inorg Chem* 52:3268–3279
  36. Micskei K, Powell DH, Helm L, Brücher E, Merbach AE (1993) Water exchange on [Gd(H<sub>2</sub>O)<sub>8</sub>]<sup>3+</sup> and [Gd(PDTA)(H<sub>2</sub>O)<sub>2</sub>] in aqueous solution: a variable-pressure, -temperature and magnetic field <sup>17</sup>O NMR study. *Magn Reson Chem* 31:1011–1020. doi:10.1002/mrc.1260311111
  37. MATLAB 7.6 and Statistics Toolbox.
  38. Mitchell M (1998) An Introduction to Genetic Algorithms. 209. doi: 10.1016/S0898-1221(96)90227-8
  39. Hedegård ED, Kongsted J, Sauer SP (2012) Improving the calculation of electron paramagnetic resonance hyperfine coupling tensors for d-block metals. *Phys Chem Chem Phys* 14:10669. doi: 10.1039/c2cp40969k
  40. da Silva Gonçalves A, França TCC, Caetano MS, Ramalho TC (2014) Reactivation steps by 2-PAM of tabun-inhibited human acetylcholinesterase: reducing the computational cost in hybrid QM/MM methods. *J Biomol Struct Dyn* 32:301–307. doi: 10.1080/07391102.2013.765361

41. Ramalho TC, da Cunha EFF, de Alencastro RB (2004) Solvent effects on  $^{13}\text{C}$  and  $^{15}\text{N}$  shielding tensors of nitroimidazoles in the condensed phase: a sequential molecular dynamics/quantum mechanics study. *J Phys Condens Matter* 16:6159–6170. doi: 10.1088/0953-8984/16/34/015
42. Coutinho K, Canuto S (1997) Solvent Effects from a Sequential Monte Carlo - Quantum Mechanical Approach. In: Per-Olov Löwdin John R. Sabin MCZJK, Karelson M (eds). Academic Press, pp 89–105
43. Misiti M, Misiti Y, Oppenheim G, Poggi JM (2007) Wavelets and their applications, ISTE DSP Series
44. Kamada M, Toda M, Sekijima M, et al (2011) Analysis of motion features for molecular dynamics simulation of proteins. *Chem Phys Lett* 502:241–247. doi: 10.1016/j.cplett.2010.12.028
45. Lepage M, Gore JC (2004) Contrast mechanisms in magnetic resonance imaging. *JPCS* 3:78–86. doi: 10.1088/1742-6596/3/1/008
46. Hedegård ED, Kongsted J, Sauer SPA (2011) Optimized Basis Sets for Calculation of Electron Paramagnetic Resonance Hyperfine Coupling Constants: aug-cc-pVTZ-J for the 3d Atoms Sc–Zn. *J Chem Theory Comput* 7:4077–4087. doi: 10.1021/ct200587k
47. Godbout N, Salahub DR, Andzelm J, Wimmer E (1992) Optimization of Gaussian-type basis sets for local spin density functional calculations. Part I. Boron through neon, optimization technique and validation. *Can J Chem* 70:560–571. doi: 10.1139/v92-079
48. Ziener CH, Bauer WR, Melkus G, et al (2006) Structure-specific magnetic field inhomogeneities and its effect on the correlation time. *J Magn Reson Im* 24:1341–7. doi: 10.1016/j.mri.2006.08.005
49. Rodríguez-Rodríguez A, Esteban-Gómez D, de Blas A, et al (2012) Solution structure of Ln(III) complexes with macrocyclic ligands through theoretical evaluation of  $^1\text{H}$  NMR contact shifts. *Inorg Chem* 51:13419–29. doi: 10.1021/ic302322r
50. Harris D, Loew GH, Komornicki A (1997) Structure and Relative Spin-State Energetics of

[Fe(H<sub>2</sub>O)<sub>6</sub>]<sup>3+</sup>: A Comparison of UHF, Møller–Plesset, Nonlocal DFT, and Semiempirical INDO/S Calculations. *J Phys Chem A* 101:3959–3965. doi: 10.1021/jp963296x

51. Borel A, Yerly F, Helm L, Merbach AE (2002) Multiexponential Electronic Spin Relaxation and Redfield's Limit in Gd(III) Complexes in Solution: Consequences for <sup>17</sup>O/<sup>1</sup>H NMR and EPR Simultaneous Analysis. *J Am Chem Soc* 124:2042–2048. doi: 10.1021/ja016919f
52. Gao RX, Yan R (2011) From Fourier Transform to Wavelet Transform: A Historical Perspective. In: *Wavelets*. Springer US, Boston, MA, pp 17–32
53. Galdino B, Oliveira D, Cássia R De, et al (2009) Uma comprovação químico-quântica sobre a formação de ligações de hidrogênio e interações secundárias em sistemas heterocíclicos intermoleculares Introdução. *Orbital* 1:167–182.
54. Grabowski SJ (2011) What is the covalency of hydrogen bonding? *Chem Rev* 111:2597–625. doi: 10.1021/cr800346f
55. Koch U, Popelier PLA (1995) Characterization of C-H-O Hydrogen Bonds on the Basis of the Charge Density. *J Phys Chem A* 99:9747–9754. doi: 10.1021/j100024a016
56. Oliveira BG, Araújo RCMU, Ramos MN, Oliveira, GB; Araújo RCMU (2010) A topologia molecular QTAIM e a descrição mecânico-quântica de ligações de hidrogênio e ligações de di-hidrogênio. *Quim Nova* 33:1155–1162. doi: 10.1590/S0100-40422010000500029
57. Cortesguzman F, Bader RFW (2005) Complementarity of QTAIM and MO theory in the study of bonding in donor-acceptor complexes. *Coord Chem Rev* 249:633–662. doi: 10.1016/j.ccr.2004.08.022
58. Ruiz E, Cirera J, Alvarez S (2005) Spin density distribution in transition metal complexes. *Coord Chem Rev* 249:2649–2660. doi: 10.1016/j.ccr.2005.04.010
59. Alarcón E, González-Béjar M, Gorelsky S, et al (2010) Photophysical characterization of atorvastatin (Lipitor®) ortho-hydroxy metabolite: role of hydroxyl group on the drug



photochemistry. *Photochem Photobiol Sci* 9:1378–84. doi: 10.1039/c0pp00102c

60. Powell DH, Dhubhghaill OMN, Pubanz D, et al (1996) Structural and Dynamic Parameters Obtained from  $^{17}\text{O}$  NMR , EPR , and NMRD Studies of Monomeric and Dimeric  $\text{Gd}^{3+}$  Complexes of Interest in Magnetic Resonance Imaging : An Integrated and Theoretically Self-Consistent Approach 1. *JACS* 7863:9333–9346.
61. Ramalho TC, da Cunha EFF, de Alencastro RB (2004) Theoretical Study of Adiabatic and Vertical Electron Affinity of Radiosensitizers in Solution Part 2: Analogues of Tirapazamine. *J Chem Theory* 03:1–13. doi: 10.1142/S0219633604000866
62. Huang CH, Tsourkas A (2013) Gd-based macromolecules and nanoparticles as magnetic resonance contrast agents for molecular imaging. *Curr Top Med Chem* 13:411–421. doi: 10.2174/1568026611313040002

**Article 3-Comparing Structure and Dynamics of Solvation of Different Iron Oxide Phases  
for Enhanced Magnetic Resonance Imaging**

**(article published in *Select Chemistry*)**

**Abstract:** Cancer is a global epidemic that significantly affects all ages and socioeconomic groups. One of the great difficulties of cancer is its diagnosis, mainly in the initial phase. Currently, the most used and effective technique for cancer diagnosis is Magnetic Resonance Imaging (MRI). For a better visualization of MRI images, it is necessary to use contrast agents (CAs). These CAs are paramagnetic compounds capable of enhancing the relaxation rates of water protons in tissues. The most used CAs in MRI are gadolinium ( $Gd^{3+}$ ) complexes. However, these CAs are very toxic to the body.<sup>[5]</sup> Thus, in this study, the 100 faces of various iron oxides ( $\delta$ -FeOOH,  $\alpha$ -FeOOH,  $Fe_2O_3$ ,  $Fe_3O_4$ ) were analyzed in order to replace  $Gd^{3+}$  complexes. For this purpose, calculations of molecular dynamics (MD) were performed and the main conformations were selected using the OWSCA method for subsequent quantum calculations of the hyperfine coupling constant. The results show a large increase in  $A_{iso}$  values. Thus, it is suggested that the compounds studied may be promising CAs in MRI.

## 1.0-Introduction

Cancer is one of the most frightening diseases of society and comprises a group of more than 100 diseases, with a high mortality rate due to the difficulty in its diagnosis, mainly in its initial phase.<sup>[1,2]</sup> Among the most used diagnostic techniques for cancer, Magnetic Resonance Imaging (MRI) is highlighted. Currently, MRI has become an important part of image resolution in the modern clinic, since MRI has a non-invasive character, high spatial resolution and great depth of soft tissue penetration.<sup>[3-5]</sup> MRI usually relies on the detection of the nuclear magnetization of mobile water protons<sup>[6]</sup> and on the principles of nuclear magnetic resonance (NMR).<sup>[6]</sup> The NMR signal is generated by hydrogen nuclei present in water and its changes are dependent on chemical environment; the relaxation process of hydrogen is governed by three parameters: proton density, longitudinal relaxation time  $T_1$ , and transverse relaxation time  $T_2$ . However, the variation in proton density between tissues is small; thus, most of the contrast measured in MRI images is based on  $T_1$  or  $T_2$  relaxation times.<sup>[7]</sup> Relaxation rates ( $R_1 = 1/T_1$  and  $R_2 = 1/T_2$ ) depend on the hyperfine coupling constant ( $A$  or  $A_{iso}$ ) between the electron spin of the metal ion and the  $^1H$  or  $^{17}O$  nuclear spin.<sup>[8]</sup> It is possible to obtain images of human tissues only with the natural relaxation of water hydrogens; however, image resolution is not frequently satisfactory. Thus, paramagnetic contrast agents (CAs), such as magnetite, are used to improve

image signal quality, since those CAs are able to decrease  $T_1$  and  $T_2$  relaxation times of water molecules in the vicinity of their structure.<sup>[9,10]</sup> CAs are paramagnetic compounds which increase image contrast by preferentially influencing  $T_1$  and/or  $T_2$  relaxation times of water molecules in the vicinity of their compounds<sup>11</sup>. Currently, the CAs most used as MRI probes are gadolinium ( $Gd^{3+}$ ) complexes; despite being very effective, they are very toxic to the body, even in small concentrations. Thus, less toxic and more efficient CAs able to substitute  $Gd^{3+}$  complexes have been studied.<sup>[5,10,12]</sup> SPIONs (superparamagnetic iron oxide nanoparticles) have been investigated as novel contrast agents in MRI, due to a combination of favorable superparamagnetic properties.<sup>[13,14]</sup> The unique magnetic properties of SPIONs arise from a combination of atomic composition, crystal structure and size effects. SPIONs exhibit ferromagnetic behavior, have iron atoms  $Fe^{2+}$  and  $Fe^{3+}$  and can mainly alter the relaxation time  $T_2$  of water protons surrounding the particle.<sup>[15,16]</sup> In this paper, ferroxhyte ( $\delta$ -FeOOH), goethite ( $\alpha$ -FeOOH), hematite ( $Fe_2O_3$ ) and magnetite ( $Fe_3O_4$ ) were studied as spectroscopic probes. The face 100 of iron oxides was selected. It is important to keep in mind that the face 100 is very important, since it has a chiral subdomain. Furthermore, the face 100 is in the plane perpendicular to the lattice fringes, which can be very promising to explore this face in theoretical calculations.<sup>[9,17-19]</sup> Currently, little attention has been given to SPIONS as CAs, mainly in computational studies evaluating thermal and solvent effects of water molecules on the hyperfine coupling constant ( $A_{iso}$ ) of SPIONs.<sup>[9,20]</sup>

Following this line, the aim of this study is to analyze water coordination in the face 100 of different phases of iron oxides ( $\delta$ -FeOOH,  $\alpha$ -FeOOH,  $Fe_2O_3$ ,  $Fe_3O_4$ ), in order to evaluate their thermal and solvent effects on the hyperfine coupling constant ( $A_{iso}$ ) and to propose the respective iron oxides as promising CAs in MRI.

## **2.0-Results and Discussion**

### **2.1-Optimal wavelet signal compression algorithm (OWSCA)**

For the selection of MD structures, the OWSCA method was chosen. This method has already been successfully used for the treatment of another system.<sup>[21]</sup> The OWSCA method is based on the wavelet transform.<sup>[22]</sup> Discrete wavelets are functions used as tools for data processing or manipulation in order to analyze data at different resolution scales, mainly to detect transients, remove noise and compress data.<sup>[23]</sup>

Thus, the discrete wavelet transform of a given data set  $x(t)$  can be basically defined according to Equation 1.<sup>[24]</sup>

Equation 1:

$$d_{j,k} = \int_{-\infty}^{\infty} x(t) \psi_{j,k}(t) dt$$

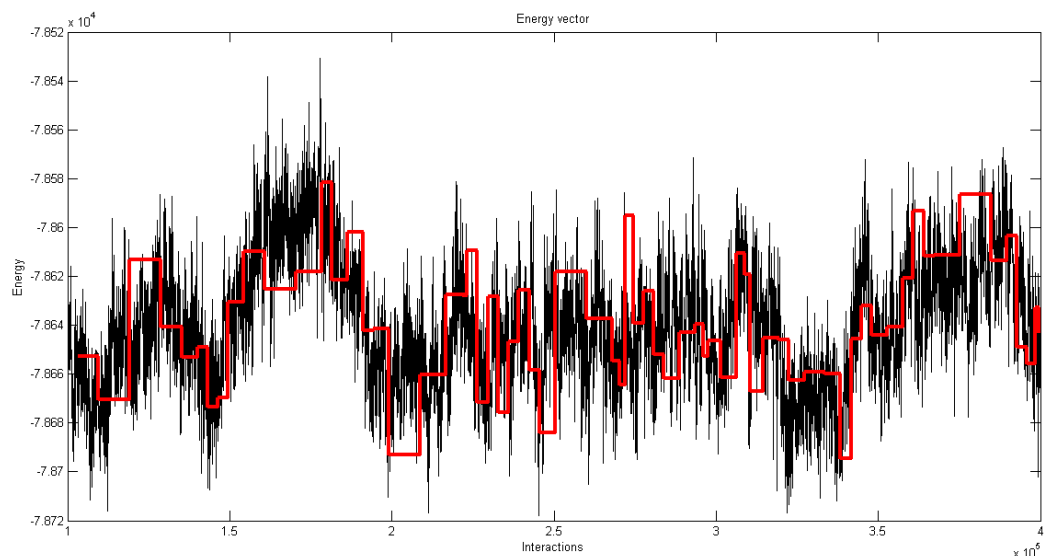
where,  $d_{j,k}$  is the wavelet coefficient,  $t$  is the variable time (normalized between 0 and 1),  $j$  represents the scaling parameter (resolution), which determines the time and frequency resolutions of the scaled wavelet function  $\psi$  and  $k$  represents the shifting parameter, which translates the scaled wavelet along the time axis. Typically  $j$  and  $k$  are correlated, where  $j = 0 \cdots N - 1$  and  $k = 0 \cdots 2^N - 1$ , where  $N$  denotes the maximum resolution. In this study, the Haar wavelet was used; it is defined according to Equation 2:

Equation 2:

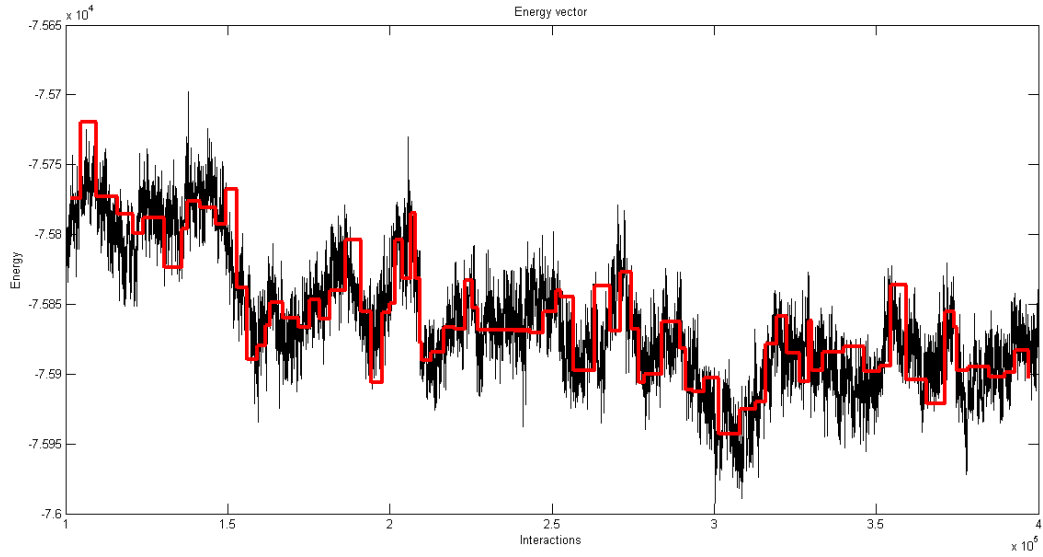
$$\psi_{Haar}(t) = \begin{cases} -1 & 0 \leq t < 0.5 \\ 1 & 0.5 \leq t < 1 \\ 0 & otherwise \end{cases}$$

Haar is the simplest wavelet function and presents a compact support. However, it has a discontinuous profile. This property can be an advantage for the analysis of signals with abrupt (non-smooth) transitions.<sup>[24]</sup> In general, the OWSCA method can be summarized according to Figure S1 in the supplementary material. In this paper, the OWSCA method was used for the system ( $[\text{Fe}(\text{H}_2\text{O})_6]^{2+}$ ,  $\delta\text{-FeOOH}$ ,  $\alpha\text{-FeOOH}$ ,  $\text{Fe}_2\text{O}_3$ ,  $\text{Fe}_3\text{O}_4$ ), while the  $[\text{Fe}(\text{H}_2\text{O})_6]^{2+}$  complex was used to validate our methodology. The OWSCA method aims to compress  $x(t)$  in order to reduce the number of MD conformations to be analyzed. After compression,  $x(t)$  is reduced to  $y(t)$ . Thus,

OWSCA was used to compress a data set with 7801 points (MD conformations). The comparison between the original data  $x(t)$  and the compressed data  $y(t)$  can be observed in Figure 1; the black line is the original DM signal and the red is the compromised signal (treated by OWSCA). It can be observed that the original data set  $x(t)$  has a high (noisy) oscillatory profile, while the compressed data set  $y(t)$  presents a smoother profile, not equidistantly spaced. Figure 1a shows the treatment of complex  $[\text{Fe}(\text{H}_2\text{O})_6]^{2+}$  signal; thus, the signal processing 50 conformations was selected. For the system  $\delta\text{-FeOOH}$ , 40 conformations were selected (Figure 1b). For the other systems, the signal treatment was very similar to the  $\delta\text{-FeOOH}$  oxide; therefore, Figures of other systems were not included. For the  $\alpha\text{-FeOOH}$  system, 32 conformations were selected; 35 conformations were selected for  $\text{Fe}_2\text{O}_3$  and 34 for  $\text{Fe}_3\text{O}_4$ . It is possible to observe that, for all systems, the number of structures selected by the OWSCA method was similar, which was expected, since all systems consist of iron oxides. Figure S3 reveals the amplitude of the coefficients in OWSCA method.



a)



b)

Figure 1 - Energy of MD conformations (original and compressed) at each time (fs). a)  $[\text{Fe}(\text{H}_2\text{O})_6]^{2+}$  complex and b)  $\delta\text{-FeOOH}$ .

In order to quantify the precision of the OWSCA procedure, the residue defined according to Equation 3 was computed:

Equation 3:

$$res = \frac{\sqrt{\sum_i (E_i - E_c)^2}}{\bar{E}}$$

where,  $E_i$  is the  $i$ th MD conformation energy of the original data set  $x(t)$  and  $E_c$  is the  $i$ th MD conformation energy of the compressed data set  $y(t)$ , both evaluated at  $i = 1, \dots, n_y$ .  $\bar{E}$  is the average MD conformation energy of the original data set  $x(t)$  evaluated at all points. Thus, the residue computed was 0.18% for  $[\text{Fe}(\text{H}_2\text{O})_6]^{2+}$ . The same OWSCA analysis was performed for other iron oxides: for  $\delta\text{-FeOOH}$ , a residue of 0.07% was found, while for  $\alpha\text{-FeOOH}$ ,  $\text{Fe}_3\text{O}_4$  and  $\text{Fe}_2\text{O}_3$ , the residues were 1.2%, 0.48% and 0.054, respectively. It should be emphasized that

the validation of the OWSCA method was performed after theoretical spectroscopic calculations, explained in the next topic.

## 2.2-Theoretical strategies of hyperfine coupling constant ( $A_{\text{iso}}$ ) calculations.

It is important to mention that the hyperfine coupling constant ( $A_{\text{iso}}$  or HFCCs) is the most important and sensitive variable of both relaxation times,  $T_1$  and  $T_2$ . Thus, in order to predict the relaxation time  $T_1$  of iron oxides, theoretical calculations of  $A_{\text{iso}}$  values were carried out.<sup>[17]</sup> The  $A_{\text{iso}}$  tensor for the nucleus N consists of three contributions, which are the isotropic Fermi contact (FC), the anisotropic spin–dipolar contributions and the spin–orbit contribution. Anisotropic components are only significant in ordered samples where the molecules are oriented by the static external field; therefore, the anisotropic contact is generally equal to zero. The Spin-orbit contribution is valid when the relativistic effects of atoms<sup>[25, 26]</sup> are taken into account. Thus, the calculation of isotropic FC contribution ( $A_{\text{iso}}$ ) was emphasized, and is given by Equation 4:

Equation 4:

$$A_{\text{iso}} = \frac{4\pi}{3} \beta_e \beta_N g_e g_N \langle S_Z \rangle^{-1} \rho_N^{\alpha-\beta}$$

where,  $\beta_N$  and  $\beta_e$  are the nuclear and Bohr magnetons, respectively,  $g_N$  and  $g_e$  are nuclear and free-electron g values,  $S$  is the total electron spin of the system, and  $\rho_N^{\alpha-\beta}$  represents the difference between majority spin ( $\alpha$ ) and minority spin ( $\beta$ ) densities at the position of the nucleus N.<sup>[8,27]</sup>

To validate our methodology,  $A_{\text{iso}}$  calculations of  $\text{Fe}^{2+}$  atoms of the complex  $[\text{Fe}(\text{H}_2\text{O})_6]^{2+}$  were carried out. Initially, by analyzing the difference between the explicit solvent model ( $A_{\text{iso}}^{\text{eq}}$  (PBE1PBE( $\text{H}_2\text{O}$ )/PBE1PBE( $\text{H}_2\text{O}$ ))) and implicit/explicit solvent ( $A_{\text{iso}}^{\text{eq}}$  (PBE1PBE( $\text{H}_2\text{O}$ )/PCM/PBE1PBE( $\text{H}_2\text{O}$ ))) (Table 1). A difference of 0.01 MHz was found, which is not significant. Considering thermal and solvent effects on  $A_{\text{iso}}$  calculations



( $A_{\text{iso}}^{300\text{K}}(\text{MD}(\text{H}_2\text{O})//\text{MD}(\text{H}_2\text{O}))$ ), a value of 0.48 MHz was obtained, corresponding to a difference of only 0.02 MHz between theoretical and experimental values. Therefore, it is possible to observe that the OWSCA selection method was successfully used, the experimental and theoretical results were similar, which show that the structures selected by the method were adequate to realistically represent the system.

**Table 1:**  $A_{\text{iso}}$  values of  $\text{Fe}^{2+}$  atoms for the selected  $[\text{Fe}(\text{H}_2\text{O})_6]^{2+}$  structures.

$[\text{Fe}(\text{H}_2\text{O})_6]$	$A_{\text{iso}}(\text{MHz})$
$A_{\text{iso}}^{\text{eq}}(\text{PBE1PBE}(\text{H}_2\text{O})//\text{PBE1PBE}(\text{H}_2\text{O}))$	0.43
$A_{\text{iso}}^{\text{eq}}(\text{PBE1PBE}(\text{H}_2\text{O})/\text{PCM}//\text{PBE1PBE}(\text{H}_2\text{O}))$	0.42
$A_{\text{iso}}^{300\text{K}}(\text{MD}(\text{H}_2\text{O})//\text{MD}(\text{H}_2\text{O}))$	0.48
<i>Experimental</i>	<i>0.50</i>

### 2.3-Hyperfine coupling constant (HFCCs) calculations of $^{17}\text{O}$ and $^1\text{H}$ in iron oxides.

After the validation of our methodology,  $A_{\text{iso}}$  calculations for  $^1\text{H}$  and  $^{17}\text{O}$  atoms of iron oxides ( $\delta\text{-FeOOH}$ ,  $\alpha\text{-FeOOH}$ ,  $\text{Fe}_2\text{O}_3$ ,  $\text{Fe}_3\text{O}_4$ ) were performed. Initially,  $\delta\text{-FeOOH}$  for the equilibrium structure with the explicit solvent ( $A_{\text{iso}}^{\text{eq}}(\text{PBE1PBE}(\text{H}_2\text{O})//\text{PBE1PBE}(\text{H}_2\text{O}))$ ) for  $^1\text{H}$  and  $^{17}\text{O}$  atoms, values 2.01 and 2.34 MHz were obtained, respectively. For the equilibrium structure with the explicit/implicit solvent, values of 1.75 and 2.47 MHz were obtained for  $^1\text{H}$  and  $^{17}\text{O}$  atoms, respectively. Thus, a difference of 0.26 and 0.13 MHz was observed between the explicit and explicit/implicit solvent for  $^1\text{H}$  and  $^{17}\text{O}$  atoms and described in Table 2, respectively, which is not significant. Therefore, it is possible to perform the calculations by evaluating the thermal effects only with the presence of the explicit solvent, obtaining realistic results with a lower computational cost, compared to the hybrid solvent (explicit/implicit). Taking into account the thermal effects of the system ( $A_{\text{iso}}^{300\text{K}}(\text{MD}(\text{H}_2\text{O})//\text{MD}(\text{H}_2\text{O}))$ ), 2.40 MHz are obtained for  $^1\text{H}$  atoms and 2.78 MHz for  $^{17}\text{O}$  atoms.

**Table 2:**  $A_{\text{iso}}$  values of  $^1\text{H}$  and  $^{17}\text{O}$  atoms for the selected  $\delta\text{-FeOOH}$  structures.

$\delta\text{-FeOOH}$	$A_{\text{iso}}(\text{MHz})$	
	$^1\text{H}$	$^{17}\text{O}$
$A_{\text{iso}}^{\text{eq}}$ (PBE1PBE( $\text{H}_2\text{O}$ )//PBE1PBE( $\text{H}_2\text{O}$ ))	2.01	2.34
$A_{\text{iso}}^{\text{eq}}$ PBE1PBE ( $\text{H}_2\text{O}$ )/PCM//PBE1PBE( $\text{H}_2\text{O}$ )	1.75	2.47
$A_{\text{iso}}^{300\text{K}}$ (MD( $\text{H}_2\text{O}$ )//MD( $\text{H}_2\text{O}$ ))	2.40	2.78

By analyzing  $\alpha\text{-FeOOH}$ , it is possible to observe in Table 3 that, for the equilibrium structure in the presence of the explicit solvent ( $A_{\text{iso}}^{\text{eq}}$  (PBE1PBE( $\text{H}_2\text{O}$ )//PBE1PBE( $\text{H}_2\text{O}$ ))), the values for  $^1\text{H}$  and  $^{17}\text{O}$  atoms are 1.23 and 2.04 MHz, respectively. In the presence of the hybrid solvent ( $A_{\text{iso}}^{\text{eq}}$  PBE1PBE ( $\text{H}_2\text{O}$ )/PCM//PBE1PBE( $\text{H}_2\text{O}$ ))), the values were 1.33 and 2.27 MHz for  $^1\text{H}$  and  $^{17}\text{O}$  atoms. Thus, it can be noticed that the difference between explicit and explicit/implicit solvents was of 0.10 and 0.23 MHz for  $^1\text{H}$  and  $^{17}\text{O}$  atoms. Taking into account the thermal effects ( $A_{\text{iso}}^{300\text{K}}$  (MD( $\text{H}_2\text{O}$ )//MD( $\text{H}_2\text{O}$ ))), the values were 2.63 and 3.26 MHz for  $^1\text{H}$  and  $^{17}\text{O}$  atoms.

**Table 3:**  $A_{\text{iso}}$  values of  $^1\text{H}$  and  $^{17}\text{O}$  atoms for the selected  $\alpha\text{-FeOOH}$  structures.

$\alpha\text{-FeOOH}$	$A_{\text{iso}}(\text{MHz})$	
	$^1\text{H}$	$^{17}\text{O}$
$A_{\text{iso}}^{\text{eq}}$ (PBE1PBE( $\text{H}_2\text{O}$ )//PBE1PBE( $\text{H}_2\text{O}$ ))	1.23	2.04
$A_{\text{iso}}^{\text{eq}}$ PBE1PBE ( $\text{H}_2\text{O}$ )/PCM//PBE1PBE( $\text{H}_2\text{O}$ )	1.33	2.27
$A_{\text{iso}}^{300\text{K}}$ (MD( $\text{H}_2\text{O}$ )//MD( $\text{H}_2\text{O}$ ))	2.63	3.26

For the oxide, Fe<sub>2</sub>O<sub>3</sub> in Table 4, the values for the equilibrium structure in the presence of the explicit solvent ( $A_{\text{iso}}^{\text{eq}}$  (PBE1PBE(H<sub>2</sub>O)//PBE1PBE(H<sub>2</sub>O))) were 1.23 and 2.05 MHz for <sup>1</sup>H and <sup>17</sup>O atoms, respectively. In the presence of the explicit/implicit model solvent ( $A_{\text{iso}}^{\text{eq}}$  PBE1PBE (H<sub>2</sub>O)/PCM//PBE1PBE(H<sub>2</sub>O))), the values 1.33 and 2.52 MHz for <sup>1</sup>H and <sup>17</sup>O atoms were obtained. Taking into account the thermal effects ( $A_{\text{iso}}^{300\text{K}}$  (MD(H<sub>2</sub>O)//MD(H<sub>2</sub>O))), the values 1.85 and 2.80 MHz were obtained for <sup>1</sup>H and <sup>17</sup>O atoms.

**Table 4:**  $A_{\text{iso}}$  values of <sup>1</sup>H and <sup>17</sup>O atoms for the selected Fe<sub>2</sub>O<sub>3</sub> structures.

Fe <sub>2</sub> O <sub>3</sub>	$A_{\text{iso}}$ (MHz)	
	<sup>1</sup> H	<sup>17</sup> O
$A_{\text{iso}}^{\text{eq}}$ (PBE1PBE(H <sub>2</sub> O)//PBE1PBE(H <sub>2</sub> O))	1.23	2.05
$A_{\text{iso}}^{\text{eq}}$ PBE1PBE (H <sub>2</sub> O)/PCM//PBE1PBE(H <sub>2</sub> O)	1.33	2.52
$A_{\text{iso}}^{300\text{K}}$ (MD(H <sub>2</sub> O)//MD(H <sub>2</sub> O))	1.85	2.80

Finally, the result of Fe<sub>3</sub>O<sub>4</sub> was analyzed and reported in Table 5, for the equilibrium structure in the presence of the explicit solvent ( $A_{\text{iso}}^{\text{eq}}$  (PBE1PBE(H<sub>2</sub>O)//PBE1PBE(H<sub>2</sub>O))); <sup>1</sup>H and <sup>17</sup>O values were 1.45 MHz and 2.02 MHz, respectively. For  $A_{\text{iso}}^{\text{eq}}$  PBE1PBE (H<sub>2</sub>O)/PCM//PBE1PBE(H<sub>2</sub>O), the values were 1.06 and 2.41 MHz for <sup>1</sup>H and <sup>17</sup>O atoms, respectively. Thus, a difference of 0.39 MHz for <sup>1</sup>H and <sup>17</sup>O atoms was found between explicit and explicit/implicit solvents, which was not significant. Analyzing the thermal effects ( $A_{\text{iso}}^{300\text{K}}$  (MD(H<sub>2</sub>O)//MD(H<sub>2</sub>O))), a difference of 1.85 and 2.45 MHz was found for <sup>1</sup>H and <sup>17</sup>O atoms, respectively. These data put in evidence that thermal effects can significantly influence  $A_{\text{iso}}$  values of the system.

**Table 5:**  $A_{\text{iso}}$  values of  $^1\text{H}$  and  $^{17}\text{O}$  atoms for the selected  $\text{Fe}_3\text{O}_4$  structures.

$\text{Fe}_3\text{O}_4$	$A_{\text{iso}}(\text{MHz})$	
	$^1\text{H}$	$^{17}\text{O}$
$A_{\text{iso}}^{\text{eq}}$ (PBE1PBE( $\text{H}_2\text{O}$ )/PBE1PBE( $\text{H}_2\text{O}$ ))	1.45	2.02
$A_{\text{iso}}^{\text{eq}}$ PBE1PBE ( $\text{H}_2\text{O}$ )/PCM//PBE1PBE( $\text{H}_2\text{O}$ )	1.06	2.41
$A_{\text{iso}}^{300\text{K}}$ (MD( $\text{H}_2\text{O}$ )/MD( $\text{H}_2\text{O}$ ))	1.85	2.45

In general, it is possible to observe that  $A_{\text{iso}}$  values increase considerably when iron oxides are introduced into the system with water molecules, according to the literature.  $A_{\text{iso}}$  experimental values for  $[\text{GdL}(\text{H}_2\text{O})]^{n+/-} \cdot x\text{H}_2\text{O}$  complexes for  $^1\text{H}$  atoms can range between 0.5 – 0.6 MHz, [28, 29]  $A_{\text{iso}}$  values are more sensitive to  $^{17}\text{O}$  atoms. It is also possible to observe that thermal effects greatly influence the system; thus, they are very important for spectroscopic calculations. Figure 2 shows a graph with all the studied oxides and from this result, it is clear the influence of the thermal effects on the  $A_{\text{iso}}$  values.

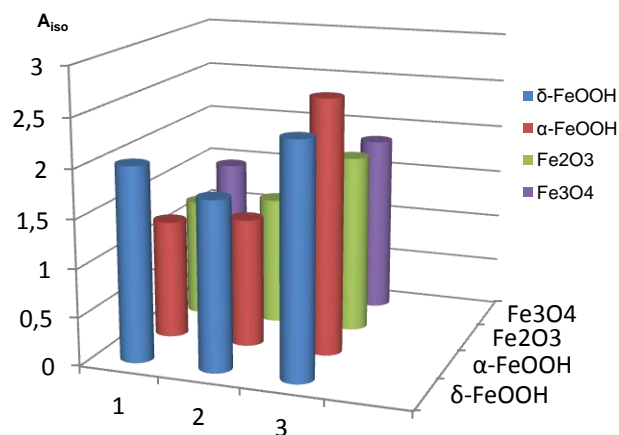


Figure 2 -  $A_{\text{iso}}$  values for the studied oxides.

## 2.4-QTAIM, spin density distribution and NCI analysis

After evaluating spectroscopic parameters, such as  $A_{\text{iso}}$ , QTAIM calculations, spin density distribution and NCI calculations were performed. These calculations were carried out in order to explain the increase in  $A_{\text{iso}}$  and its influence on the thermal effects of the systems.

The Quantum Theory of Atoms in Molecules (QTAIM) was developed in the early 1990s by Richard Bader and collaborators.<sup>[30, 31]</sup> The QTAIM theory can explain the nature of intra/intermolecular interactions and show the possible formation of hydrogen bonds.<sup>[32, 33]</sup> For the analysis of QTAIM calculations, the criteria proposed by Koch and Popelier<sup>[34]</sup> were followed; as  $A_{\text{iso}}$  values were similar for all iron oxides, the formation of hydrogen bonds was analyzed only in  $\text{Fe}_3\text{O}_4$ . According to the Koch and Popelier's criteria, a hydrogen bond is characterized by the decrease in the values  $M_1(\text{H})$  and  $V(\text{H})$ , as well as the increase in  $q(\text{H})$  and  $E(\text{H})$ . Therefore, it can be observed from Table 6 and 7 that the selected hydrogen meets these parameters.

**Table 6:** Additional atomic properties obtained by QTAIM for hydrogen bonded atoms (in au) of  $\text{Fe}_3\text{O}_4$ .

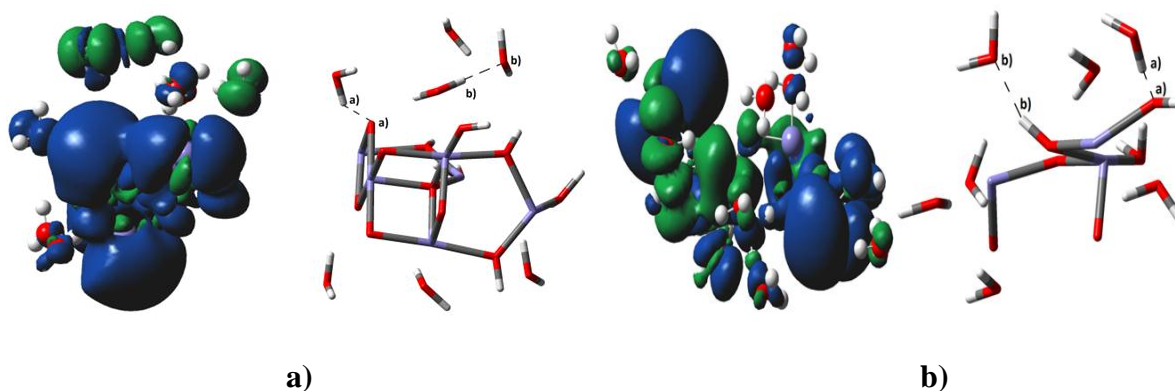
Structure	$q(\text{H})$	$M_1(\text{H})$	$V(\text{H})$	$E(\text{H})$
$\mathbf{1}_{\text{H}(\text{OH})}$	+0.331989	+0.316471	+41.356611	-0.480079
$\mathbf{2}_{(\text{Ob}\cdots\text{Hb})}$	+0.469184	+0.193958	+20.061943	-0.416471

The atoms in **1a**, **2a**, **2b** and **3a** have  $\nabla^2\rho(r) > 0$  and  $H(r) > 0$ , suggesting partial noncovalent interactions; the atoms specified in **3b** and **4a**, **4b** have  $\nabla^2\rho(r) > 0$  and  $H(r) < 0$ , suggesting partial covalent interactions and the atoms in **3b** have  $\nabla^2\rho(r) < 0$  and  $H(r) < 0$ , suggesting covalent interactions. The values of ellipticity ( $\epsilon$ ) (parameter used to describe the character of the chemical bond) were high, which features a  $\pi$  binding character, characterizing hydrogen bonds. These interactions (**HO $\cdots$ H** and **HO $\cdots$ Fe**) can actually influence  $A_{\text{iso}}$  values and system stabilization; the regions mentioned may also be seen in Figure 3.

**Table 7:** QTAIM parameters obtained at the hydrogen bond BCPs for the structures with water molecules **1-2**(au) (Structures: 1: Fe<sub>3</sub>O<sub>4</sub>; 1 δ-FeOOH; 2: α-FeOOH; 3: Fe<sub>2</sub>O<sub>3</sub>;4: Fe<sub>3</sub>O<sub>4</sub> ).

Structure	$\rho(\mathbf{r})$	$\nabla^2\rho(\mathbf{r})$	$\varepsilon$	$V(\mathbf{r})$	$G(\mathbf{r})$	$H(\mathbf{r})$
<b>1a</b> <sub>(Fea...Oa)</sub>	+0.0246	+0.0981	+0.0688	-0.0188	+0.0216	+0.0028
<b>1b</b> <sub>(Ob...Hb)</sub>	+0.0009	-0.0039	+0.6243	-0.0013	+0.0002	-0.0012
<b>2a</b> <sub>(Ha...Oa)</sub>	+0.0304	+0.1349	+0.4520	-0.0328	+0.0332	+0.0005
<b>2b</b> <sub>(Ob...Hb)</sub>	+0.0250	+0.0931	+0.1851	-0.0226	+0.0229	+0.0003
<b>3a</b> <sub>(Oa...Ha)</sub>	+0.0220	+0.0894	+0.0756	-0.0203	+0.0213	+0.0010
<b>3b</b> <sub>(Fea...Ob)</sub>	+0.0170	+0.0510	+0.2045	-0.0174	+0.0151	-0.0024
<b>4a</b> <sub>(Oa...Ha)</sub>	+0.0409	+0.0432	+0.1848	-0.0368	+0.0238	-0.0131
<b>4b</b> <sub>(Ob...Hb)</sub>	+0.0068	+0.0132	+0.2034	-0.0049	+0.0041	-0.0008

Spin density distribution in a given paramagnetic molecule indicates the contributions due to electrons with the majority spin ( $\alpha$ ) and the minority spin ( $\beta$ )<sup>[27,35]</sup> (Figure 3, colors blue (spin  $\alpha$ ) and green (spin  $\beta$ )). In general, a similarity is observed in all iron oxides. In fact, there is a high negative spin density around free water molecules and a high density of positive spin around the metal, with a contribution of d-orbitals of unpaired electrons (SOMOs).



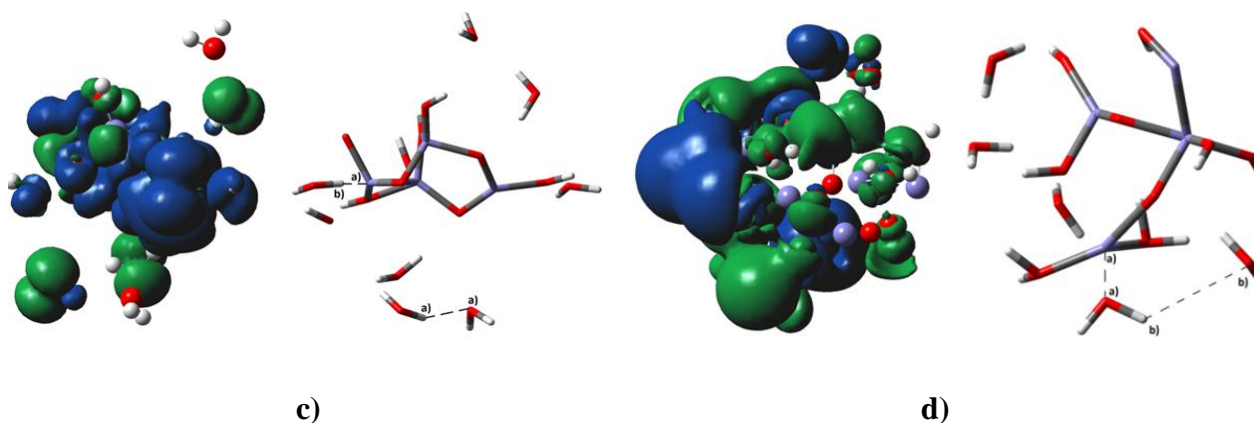
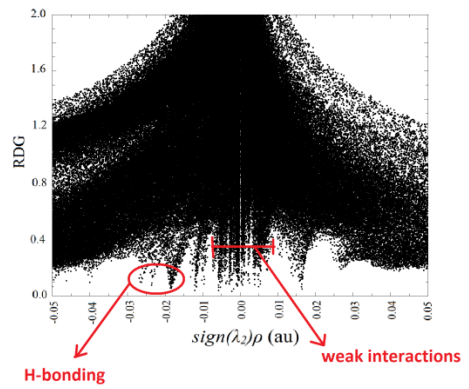
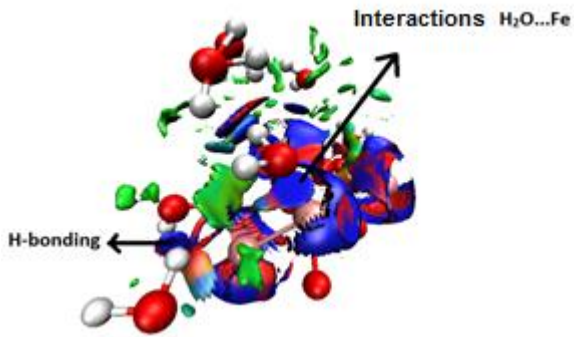
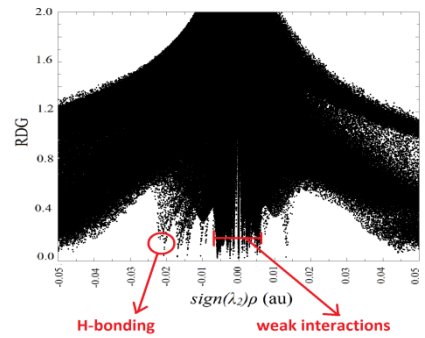
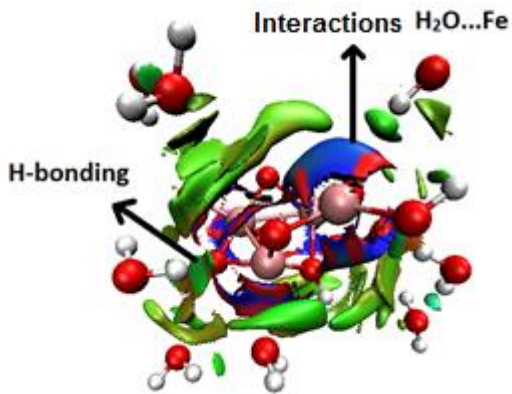


Figure 3 - Structure of the iron oxide with water molecules and their respective spin-density map (the isosurface contour value is 0.0004). a)  $\delta$ -FeOOH; b)  $\alpha$ -FeOOH; c)  $\text{Fe}_2\text{O}_3$ ; d)  $\text{Fe}_3\text{O}_4$

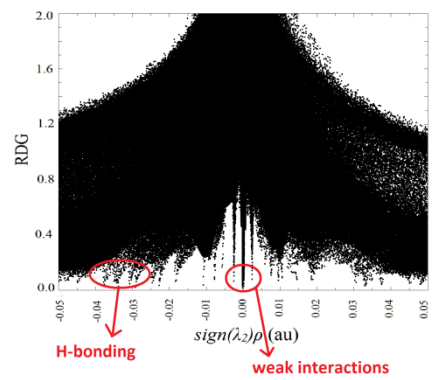
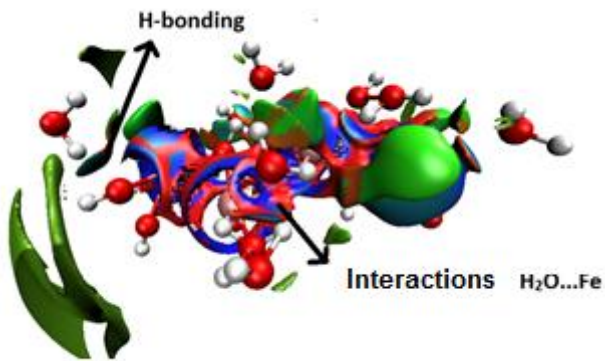
The analysis of NCI (non-covalent interactions) can be applicable to large systems, including proteins and DNA, where the analysis of noncovalent interactions is of great potential value. This shows that this type of analysis can be successfully used in our system, NCI will be shown to allow quantitative treatment of hydrogen-bond energetics.<sup>[36-38]</sup> In Figure 3, the blue region indicates strong attraction, green indicates very weak interaction, and red indicates strong repulsion; thus, in Figure 4, the regions marked with an arrow are regions that have a high electronic density. NCI analyses have a high packing ratio; therefore, many intermolecular interactions appear around  $\rho \leq 0.02$  au and are clearly distinguished from more energetic contacts such as hydrogen bonds; it is possible to observe the hydrogen bonds in the graph of RDG vs.  $\text{sign}(\lambda_2) \rho$  (ua).<sup>[39]</sup> In Figure 3, it is possible to observe hydrogen bonds; these regions are in full agreement with the analyses carried out by QTAIM. Thus, it is possible to notice the values are directly related to the strength of the hydrogen bonds ( $\text{O}\cdots\text{H}$ ), besides the interactions between water molecules and iron oxide ( $\text{Fe}\cdots\text{O}$ ). In all cases, we observed that the strength of the interaction is similar for all studied oxides but tended to increase with the strength and the type of the evolved interactions (Figure 4).



a)



b)



c)



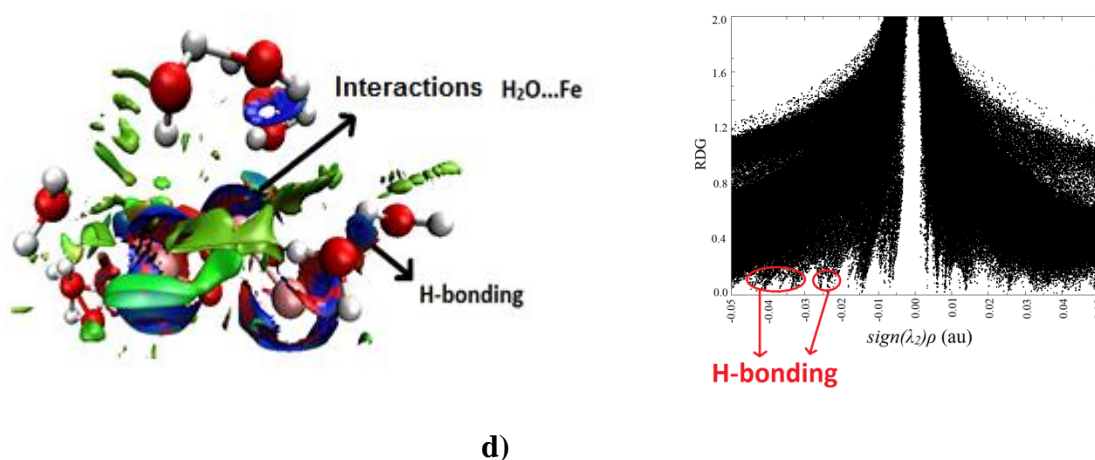


Figure 4- NCI isosurfaces and reduced density gradient RDG vs.  $\text{sign}(\lambda^2) \rho$  (au). a)  $\delta$ -FeOOH; b)  $\alpha$ -FeOOH; c)  $\text{Fe}_2\text{O}_3$ ; d)  $\text{Fe}_3\text{O}_4$ .

We believe that  $A_{\text{iso}}$  can rationalize the NMR relaxation properties, which is a crucial parameter for MRI probes. In fact, both relaxation rates ( $R_1$  and  $R_2$ ) depend on the hyperfine coupling constant ( $A_{\text{iso}}$ ) between the electron spin of the metal ion and the  $^1\text{H}$  nuclear spin. Thus, a deeper understanding of the relaxation rate mechanisms of water molecules on the influence of paramagnetic ions requires a combined understanding of solvent and thermal effects on  $^1\text{H}$  hyperfine coupling constant ( $A$ ) calculations. From our theoretical findings, the increase in  $A_{\text{iso}}$  values is mainly due to the H bonds between water molecules and the oxides, then, it is expected that oxyhydroxides, such as ferroxhyte ( $\delta$ -FeOOH) and goethite ( $\alpha$ -FeOOH) can be more active as MRI probes. In line with that, the results involving solvent and thermal effects, the ( $A_{\text{iso}}^{300\text{K}}$  (MD( $\text{H}_2\text{O}$ )/MD( $\text{H}_2\text{O}$ ))) methodology in Tables 2 to 5, put clearly in evidence this tendency (Tables 2-5). This feature could, in principle, reveal the use of  $\delta$ -FeOOH as a promising contrast agent for MRI.

### 3.0-Conclusions

The results obtained from the theoretical calculations presented in this study showed a large increase in  $A_{\text{iso}}$  values for the atoms  $^1\text{H}$  and  $^{17}\text{O}$  of water molecules when iron oxides ( $\delta$ -FeOOH,  $\alpha$ -FeOOH,  $\text{Fe}_2\text{O}_3$ ,  $\text{Fe}_3\text{O}_4$ ) are introduced into the system. Thus, with the increase in  $A_{\text{iso}}$

values and, consequently, in  $T_2$  and  $T_2^*$  values of water molecules in the system, the calculations showed that there is no significant difference between implicit and explicit solvent in the system and  $^{17}\text{O}$  atoms are more sensitive than  $^1\text{H}$  atoms to the spectroscopic parameters of  $A_{\text{iso}}$ . This increase in  $A_{\text{iso}}$  values was mainly due to the H bonds between water molecules and between water molecules and the oxides; this fact was proven by QTAIM and NCI calculations. Studies have shown that thermal effects are very important for a more realistic description of the system, since they directly influence  $A_{\text{iso}}$  values. It was demonstrated that the OWSCA method was successfully applied in the selection of DM structures and this method can have a variety of applications in the selection of DM structures in theoretical physical chemistry. At last, we strongly affirm that all the iron oxides studied are great candidates as promising ACs in MRI.

#### **4.0-Supporting Information Summary**

The contents of the SI includes details of the Computational methods, OWSCA is summarized (Figure S1), other energy of MD conformations (original and compressed) (Figure S2) and Wavelet coefficients (Figure S3).

#### **5.0-Acknowledgements**

The authors thank the Brazilian agencies FAPEMIG, CAPES, and CNPq for the financial support of this research the UFLA and UFF for infrastructure and encouragement in this work. This work was also supported by Excellence project FIM.

**6.0-Keywords:** Contrast Agents, Iron Oxide, MRI, OWSCA, SPIONs

## 7.0-Reference

- [1] V. L. De Almeida, A. Leitão, C. Barrett, C. Alberto and C. Luis, *Quim. Nova* **2005**, 28, 118–129.
- [2] D. R. R. Batista, M. De Mattos and S. F. da Silva, *Rev. Enferm. da UFMSM* **2015**, 5, 499–510.
- [3] J. Y. et al LI, *Spectrochim. Acta Part A Mol. Biomol. Spectrosc.* **2013**, 102, 66–70.
- [4] H. Jung, B. Park, C. Lee, J. Cho, J. Suh, J. Park, Y. Kim, J. Kim, G. Cho and H. Cho, *Nanomedicine Nanotechnology, Biol. Med.* **2014**, 10, 1679–1689.
- [5] M. Borges, S. Yu, A. Laromaine, A. Roig and S. Su, *RSC Advances* **2015**, 86779–86783.
- [6] M. Lepage and J. C. Gore, *J. Phys. Conf. Ser.* **2004**, 3, 78–86.
- [7] A. Accardo, D. Tesauro, L. Aloj, C. Pedone and G. Morelli, *Coord. Chem. Rev.* **2009**, 253, 2193–2213.
- [8] G. Klug, T. Kampf, S. Bloemer, J. Bremicker, C. H. Ziener, A. Heymer, U. Gbureck, E. Rommel, U. Nöth, W. A. Schenk, P. M. Jakob and W. R. Bauer, *Magn. Reson. Med.* **2010**, 64, 1607–1615.
- [9] M. A. Gonçalves, F. C. Peixoto, E. F. F. da Cunha and T. C. Ramalho, *Chem. Phys. Lett.* **2014**, 609, 88–92.
- [10] S. J. Dorazio and J. R. Morrow, *Eur. J. Inorg. Chem.* **2012**, 2006–2014.
- [11] D. Esteban-Gómez, A. de Blas, T. Rodríguez-Blas, L. Helm and C. Platas-Iglesias, *Chemphyschem* **2012**, 13, 3640–50.
- [12] A. O. Olatunde, S. J. Dorazio, J. a Sperryak and J. R. Morrow, *J. Am. Chem. Soc.* **2012**, 134, 18503–5.
- [13] M. E. Khosroshahi, H. A. Rezvani, H. Keshvari, S. Bonakdar and M. Tajabadi, *Mater Sci Eng C Mater Biol Appl.* **2016**, 62, 544–52.
- [14] S. Yoffe, T. Leshuk, P. Everett and F. Gu, *Current Pharmaceutical Design.* **2013**, 19, 493–509.
- [15] Z. R. Stephen, F. M. Kievit and M. Zhang, *Mater. Today* **2012**, 14, 330–338.
- [16] A. M. Mesquita, I. R. Guimarães, G. M. M. d. Castro, M. A. Gonçalves, T. C. Ramalho and M. C. Guerreiro, *Appl. Catal. B Environ.* **2016**, 192, 286–295.
- [17] M. A. Gonçalves, E. F. F. da Cunha, F. C. Peixoto and T. C. Ramalho, *Comput. Theor.*

- Chem.* **2015**, 1069, 96–104.
- [18] L. C. A. Oliveira, T. C. Ramalho, M. Gonçalves, F. Cereda, K. T. Carvalho, M. S. Nazzarro and K. Sapag, *Chem. Phys. Lett.* **2007**, 446, 133–137.
- [19] S. K. Ghose, G. a. Waychunas, T. P. Trainor and P. J. Eng, *Geochim. Cosmochim. Acta* **2010**, 74, 1943–1953.
- [20] M. A. Gonçalves, E. F. F. da Cunha, F. C. Peixoto and T. C. Ramalho, *Comput. Theor. Chem.* **2015**, 1069, 96–104.
- [21] M. A. Gonçalves, L. S. Santos, D. M. Prata, F. C. Peixoto, E. F. F. da Cunha and T. C. Ramalho, *Theor. Chem. Acc.* **2017**, 136, 2-13.
- [22] P. SCHRODER, *IEEE Comput. Graph. Appl.* **1995**, 15, 76–84.
- [23] G. Beylkin, *Proceedings of symposia in applied mathematics* **1993**, 47, 89.
- [24] G. Oppenheim, *Proc. Symp. Appl. Math.* **2007**.
- [25] E. D. Hedega, J. Kongsted and S. P. A. Sauer, *J. Chem. Theory Comput.* **2013**.
- [26] V. G. M. Martin Kaupp, Michael Bühl, *Calculation of NMR and EPR Parameters: Theory and Applications* **2004**.
- [27] V. Patinec, G. A. Rolla, M. Botta, R. Tripier, D. Esteban-Gomez and C. Platas-Iglesias, *Inorg. Chem.* **2013**, 52, 11173–11184.
- [28] D. H. Powell, O. M. N. Dhubghaill, D. Pubanz, L. Helm, Y. S. Lebedev, W. Schlaepfer and A. E. Merbach, *J. Am. Chem. Soc.* **1996**, 118, 9333–9346.
- [29] C. F. G. C. Geraldes and S. Laurent, *Contrast Media Mol. Imaging* **2009**, 4, 1–23.
- [30] R. J. Matta, C F; Boyd, *No The Quantum Theory of Atoms in Molecules* **2007**.
- [31] B. Galdino, D. Oliveira, R. De Cássia, M. Ugulino and D. Araújo, *Orbital* **2009**, 1, 167–182.
- [32] S. J. Grabowski, *Chem. Rev.* **2011**, 111, 2597–625.
- [33] U. Koch and P. L. A. Popelier, *J. Phys. Chem.* **1995**, 99, 9747–9754.
- [34] B. G. Oliveira, R. C. M. U. Araújo, M. N. Ramos and R. C. M. U. Oliveira, G B; Araújo, *Quim. Nova* **2010**, 33, 1155–1162.
- [35] E. Alarcón, M. González-Béjar, S. Gorelsky, R. Ebensperger, C. Lopez-Alarcón, J. C. Netto-Ferreira and J. C. Scaiano, *Photochem. Photobiol. Sci.* **2010**, 9, 1378–84.
- [36] J. Contreras-García, E. R. Johnson, S. Keinan, R. Chaudret, J. P. Piquemal, D. N. Beratan and W. Yang, *J. Chem. Theory Comput.* **2011**, 7, 625–632.

- [37] J. R. Lane, J. Contreras-García, J. P. Piquemal, B. J. Miller and H. G. Kjaergaard, *J. Chem. Theory Comput.* **2013**, 9, 3263–3266.
- [38] J. Contreras-García, W. Yang and E. R. Johnson, *J. Phys. Chem. A* **2011**, 115, 12983–12990.
- [39] A. Otero-de-la-Roza, E. R. Johnson and J. Contreras-García, *Phys. Chem. Chem. Phys.* **2012**, 14, 12165.



Supporting Information  
Copyright Wiley-VCH Verlag GmbH & Co. KGaA, 69451 Weinheim, 2017

**Comparing Structure and Dynamics of Solvation of  
Different Iron Oxide Phases for Enhanced Magnetic  
Resonance Imaging**

Mateus A. Gonçalves, Lizandro S. Santos, Fernando C. Peixoto, Elaine F. F. da Cunha,  
Telles C. Silva, and Teodorico C. Ramalho\*

## **Supporting Information**

### **1. Computational methods**

### **2. References**

### **3. Figures**

**Figure S1:** OWSCA is summarized.

**Figure S2:** Energy of MD conformations (original and compressed) at each time (fs). a) goethite  
b) hemathite, c) magnethite.

**Figure S3:** Wavelet coefficients of  $x(t)$ .

## 1. Computational methods

### 1.1. Structure optimization

All structures were built in BAND program, [1] using the following coordinates. For  $\delta$ -FeOOH: Space Group: P-3m1; network parameters:  $a = 2.946(2) \text{ \AA}$ ,  $c = 4.552 \text{ \AA}$ ; and the atom position parameters were: Fe:  $x, y, z = 0$ ; O:  $x = 0.3333, y = 0.6667, z = 0.2468$ ; H:  $x = 0.3333, y = 0.6667, z = 0.5100$ . [2] For  $\alpha$ -FeOOH: Space Group: PNMA; network parameter:  $a=9.950 \text{ \AA}$ ,  $b=3.010 \text{ \AA}$ ,  $c=4.620 \text{ \AA}$ ; and the position parameters were: Fe:  $x = 0.145, y = 0.250, z = -0.045$ ; H:  $x: -0.080, y: 0.250, z: -0.380$ ; O1:  $x = -0.199, y = 0.250, z = 0.288$ ; O2:  $x = -0.053, y = 0.250, z = -0.198$ . [23] For Fe<sub>2</sub>O<sub>3</sub>; Space Group R-3c;  $a = 5.038 \text{ \AA}$ ;  $c = 13.772$ ;  $\alpha = \beta = 90.0$ ;  $Z=6$  and the atom position parameters were Fe:  $x,y,z = 0.0000$ ; O :  $x = 0.3059, y = 0.0000, z = 0.2500$  [4] and for Fe<sub>3</sub>O<sub>4</sub>: Space Group Fd-3m;  $a = 8.3941 \text{ \AA}$ ;  $\alpha = 90.00$ ;  $Z = 8$  and the atom position parameters were Fe1:  $x,y,z = 0.1250$ ; Fe2:  $x,y,z = 0.5000$ ; O:  $x,y,z = 0.2549$ . [5] Optimization was carried out in the BAND program using the functional PBE and the base Slater triple-double-zeta (TZ2P) for iron, oxygen and hydrogen atoms.

### 1.2. Molecular dynamics simulations

After structure optimizations, molecular dynamics simulations (MD) were performed with the REAX-FF program [5], using the FEOCH force field. [6] The simulation consisted of the iron oxide system coordinated with water molecules in a cubic cell with a side of  $20 \text{ \AA}$ ; the volume of the cube was determined by the density of liquid water ( $\rho=0.996 \text{ g.cm}^{-3}$ ), for the simulations we consider a layer of the oxides. MD consisted of a thermalization phase of 500 ps, followed by an additional period of 2.0 ns; the simulation was performed at 310.65 K (physiological temperature) and the system consisted of 300 water molecules. [7] It is important to mention that during the simulation we freeze the atoms of the oxides and leave only the molecules of water free to move, this in fact is important because the oxide did not react during the whole simulation.



### **1.3. Optimal Wavelet Signal Compression Algorithm (OWSCA) and hyperfine coupling constant (HFCC) calculations**

After MD simulations, MD conformations were selected using the OWSCA method.[8] It was performed in the Matlab 7.6® [9] software, with its built-in Wavelet Toolbox. Thus, the main conformations of each MD simulation were selected for subsequent hyperfine coupling constant (HFCC or Aiso) calculations. HFCC calculations were performed using the Gaussian 09 program;[10] functional PBE1PBE[20] with the basis set augcc-pVTZ-J[11] was used for oxygen and hydrogen atoms, and Lan12dz for iron atoms for all structures. In this study, the following notation, which has already been successfully used in other papers, was used: level of A<sub>iso</sub> computation//level of geometry optimization or MD simulation. Thus, this study will count on the following stocking: (PBE1PBE(H<sub>2</sub>O)//PBE1PBE(H<sub>2</sub>O)) for the Aiso calculations of equilibrium structure involving explicit solvent; (PBE1PBE(H<sub>2</sub>O)/PCM//PBE1PBE(H<sub>2</sub>O)) for the Aiso calculations of equilibrium structure involving explicit solvent and implicit solvent (PCM); considering the dynamic effects of Aiso geometry optimization calculations with explicit solvent, the following notation was used: (MD(H<sub>2</sub>O)//MD(H<sub>2</sub>O)).

### **1.4. QTAIM, Spin Density Distributions and NCI Calculations.**

*The Quantum Theory of Atoms in Molecules* (QTAIM) calculations were performed using the AIMALL program package[12] (were performed using calculations the QTAIMQB program, the analysis of the results were performed by the AIMSTUDIO program, both are part of the AIMALL program package). It is important to emphasize that, for QTAIM calculations, the .CHK file, which was obtained through calculations performed by the Gaussian 09 program, was used.[10] Calculations of noncovalent interactions (NCI) over the structures optimized at the PBE1PBE/aug-cc-pVTZJ level were performed using the NCIPLOT program.[13] Atomic spin density was evaluated using the natural population analysis (NPA), performed in the Gaussian 09 program,[10] the contour surface was fixed at 0.0004 a.u.

## 2. References

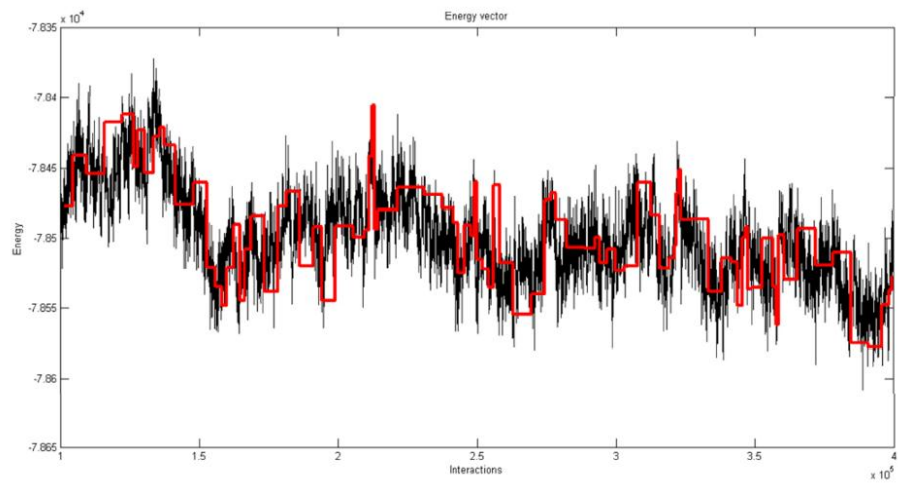
- [1] Baerends E. J, Autschbach J, Bashford D, Bérces A, Bickelhaupt F. M, Bo C, Boerrigter P. M, Cavallo L, Chong D. P, Deng L, Dickson R. M, Ellis D. E, van Faassen M, Fan M, Fischer T. H, Fonseca Guerra C, Ghysels A, Giammona A, van Gisbergen S. J. A, Götz A. W, Groeneveld J. A, Gritsenko O. V, Grüning M, Harris F. E, Harris P, van den Hoek P, Jacob C. R, Jacobsen H, Jensen L, van Kessel G, Kootstra F, Krykunov M. V, van Lenthe E, McCormack D. A, Michalak A, Mitoraj M, Neugebauer J, Nicu V. P, Noodleman L, Osinga V. P. O, Patchkovskii S, Philipsen P. H. T, Post D, Pye C. C, Ravenek W, Rodriguez J. I, Ros P, Schipper P. R. T, Schreckenbach G, Seth M, Snijders J. G, Solà M, Swart M, Swerhone D, te Velde G, Vernooijs P, Versluis L, Visscher L, Visser O, Wang F, Wesolowski T. A, van Wezenbeek E. M, Wiesenekker G, Wolff S. K, Woo T. K, Yakovlev A. L, Ziegler T. ADF2009.01, SCM, Theoretical Chemistry, Vrije Universiteit, Amsterdam (The Netherlands), 2009.
- [2] A. C. da Silva, M. R. Almeida, M. Rodriguez, A. R. T. Machado, L. C. A. de Oliveira and M. C. Pereira, *J. Photochem. Photobiol. A Chem.* **2017**, 332, 54–59.
- [3] A. Chronos, K. Desai, S. E. Redfern, M. O. Zacate and R. W. Grimes, *J. Mater. Sci.* **2006**, 41, 675–687.
- [4] M. E. Fleet, *Crystallogr. Cryst. Chem.* **1981**, 37, 917–920.
- [5] Duin V. ReaxFF User Manual. 2002.
- [6] M. Aryanpour, A. C. T. van Duin and J. D. Kubicki, *J. Phys. Chem. A* **2010**, 114, 6298–6307.
- [7] D. T. Mancini, E. F. Souza, M. S. Caetano and T. C. Ramalho, *Magn. Reson. Chem.* **2014**, 52, 129–37.
- [8] J.O.S. Giacoppo, J.B. Caregal, E.F.F. da Cunha, and T. C. Ramalho, *Mol. Sim.* **2017**, 43, 121-133.
- [9] MATLAB 7.6 and Statistics Toolbox.
- [10] M. J. Frisch, G. W. Trucks, H. B. Schlegel, G. E. Scuseria, M. A. Robb, J. R. Cheeseman, G. Scalmani, V. Barone, B. Mennucci, G. A. Petersson, H. Nakatsuji, M. Caricato, X. Li, H. P. Hratchian, A. F. Izmaylov, J. Bloino, G. Zheng, J. L. Sonnenberg, M. Had and DJF Gaussian 09. 2009.
- [11] E. D. Hedegård, J. Kongsted and S. P. a. Sauer, *Phys. Chem. Chem. Phys.* **2012**, 14, 10669.

- [12] Keith TA. AIM ALL. TK Gristmill Software, Overland Park KS. **2010**.
- [13] J. Contreras-García, E. R. Johnson, S. Keinan, R. Chaudret, J.-P. Piquemal, D. N. Beratan and W. Yang, *J. Chem. Theory Comput.* **2011**, 7, 625–632.
- [14] P. SCHRODER, *IEEE Comput. Graph. Appl.* **1995**, 15, 76–

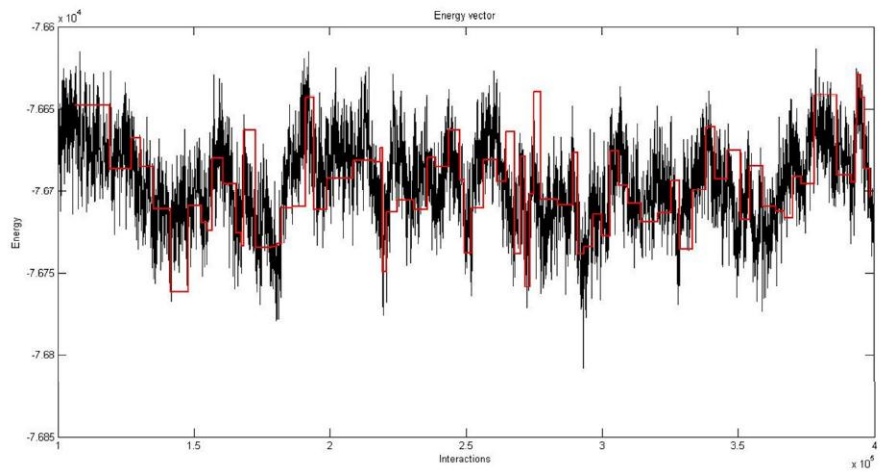
### 3. Figures

Description of OWSCA
1. Discrete wavelet transform
$d_{j,k} = \int_{-\infty}^{\infty} x(t) \psi_{j,k}(t) dt, j = 0, \dots, N - 1; k = 0, \dots, 2^N - 1$
2. Optimization to find $\delta_j^*$ , $j = 0, \dots, N - 1$
3. Wavelet compression ( for each $j$ )
$d_{j,k} = 0 \text{ if } d_{j,k} \leq \delta_j^*, j = 0, \dots, N - 1; k = 0, \dots, 2^N - 1$
4. Inverse discrete wavelet transform
$y(t) = \sum_{j=0}^{N-1} \sum_{k=0}^{2^N-1} d_{j,k} \psi_{j,k}(t)$

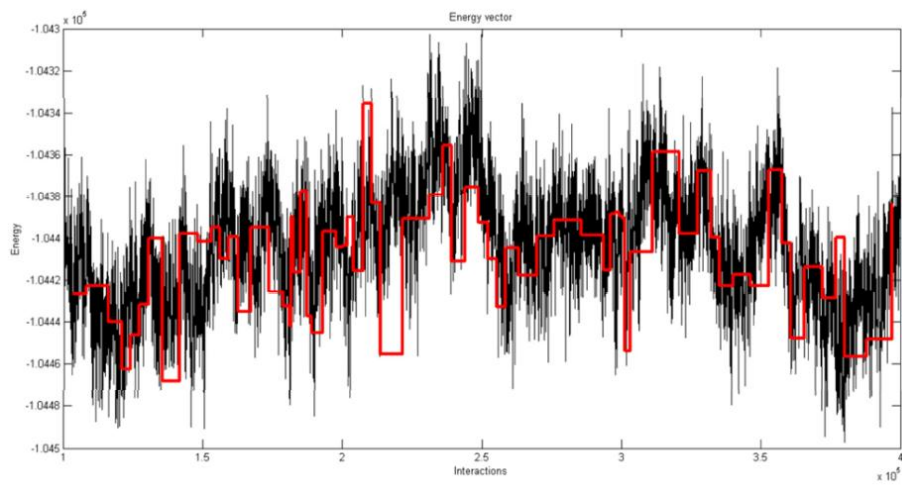
**Figure S1.** OWSCA is summarized



a)



b)



c)

**Figure S2.** Energy of MD conformations (original and compressed) at each time (fs).

a) goethite b) hemathite, c) magnethite.

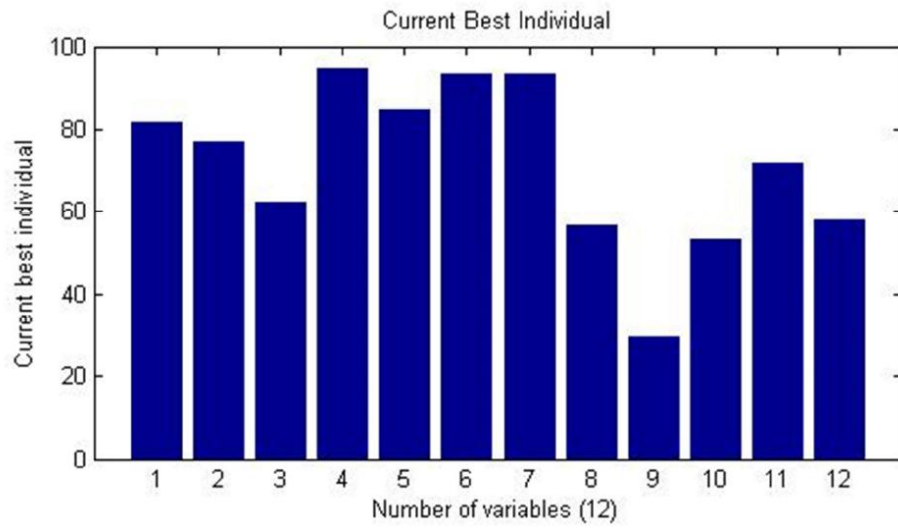


**Figure S3.** Optimal thresholds  $\delta_j^*$

**Article 4-NMR Relaxation and Relaxivity Parameters of MRI probes revealed by optimal wavelet signal compression of molecular dynamics simulations**

(article submitted in *International Journal of Quantum Chemistry-IJC*)

## Abstract

The MRI contrast agents (CAs) have been routinely used for detecting tumors at early stages. Currently, the most used CAs in MRI are gadolinium ( $Gd^{3+}$ ) complexes. However, these CAs can be toxic to the body. Thus, this work proposes  $Ni^{2+}$  complexes ( $[Ni(ACAC)_2(H_2O)_2]$ ,  $[Ni(TEA)]^{2+}$ ) as promising CAs. For the theoretical prediction, molecular dynamics simulations (MD) were carried out and the conformations were selected by the OWSCA method. The  $T_1$  and  $T_2$  values were obtained directly by means of the spectral density. Our findings showed that the  $Ni^{2+}$  complexes can be promising CAs in MRI.

**Keywords:** MRI; Contrast Agents; Computational Chemistry; OWSCA; Molecular Dynamics.



## 1-Introduction

Even with recent technological advances, cancer is still one of the biggest problems humankind has to face [1], being very difficult to diagnose in its initial phase. Following this line, one of the most employed and efficient techniques for the detection of pathologies in their initial phase is Magnetic Resonance Imaging (MRI) [2–4]. The MRI technique uses the NMR relaxation rates constants, longitudinal ( $R_1 = 1/T_1$ ) or transverse ( $R_2 = 1/T_2$ ), of water protons present in the body as contrast among different tissues. In most MRI exams, with only the natural relaxation of the hydrogens of the water it is not possible to obtain clear images of the tissues [1]. Thus, to have a better relaxation of the those nuclei, contrast agents (CAs) are used [5,6]. The CAs are paramagnetic compounds capable of increasing relaxation times constants  $T_1$  and  $T_2$  of water hydrogens in tissues. Currently, the most used CAs are the  $Gd^{3+}$  complexes, which can shorten both relaxation times constants ( $T_1$  and  $T_2$ ). Although  $Gd^{3+}$  complexes are highly efficient in the  $^1H$  relaxation of water molecules, they are very toxic and have serious effects on the organism [7].

It is important to keep in mind that to be a good contrast agent the paramagnetic compound must necessarily have a low toxicity as well as a high relaxation and relaxivity. The relaxivity of a contrast agent is the relaxation rate of a solution as a function of concentration [C], thus, the high-relaxivity agents with favorable properties for imaging applications remains an important goal [8]. Thus, new CAs are being studied to replace the  $Gd^{3+}$  complexes, as for example the  $Ni^{2+}$  complexes, which are less toxic than  $Gd^{3+}$ , and show quite effective [9,10]. In this perspective, the  $Ni^{2+}$  complexes can shorten the relaxation time  $T_2$  of the water hydrogens, and can be used as promising CAs. The paramagnetic Ni(II) complexes used as CAs for MRI are called paraCEST (paraCEST = paramagnetic chemical exchange saturation transfer; NiCEST = Ni(II) based CEST agents), the Morrow's group showed that the paraCEST complexes of Ni (II) can increase significantly relaxation time of protons of water producing highly shifted and, in some cases, narrow proton resonances [11]. It is also interesting to mention that the ligands used in these complexes must be chelates (have high stability) and have amino groups to act as electron donors [11,12]. Similarly to Fe(II), the key to forming successful paraCEST agents for Ni(II) is control of spin state, metal ion dissociation kinetics and fluxionality of the macrocyclic

complex on the NMR time scale. However, stabilizing the divalent oxidation state under biologically relevant conditions is more straightforward for Ni(II) than for Fe(II) [11]. Some studies have shown that Ni<sup>2+</sup> contrast agents are very effective [12], moreover, the magnetite nanoparticulate coated Ni<sup>2+</sup> compounds showed that T<sub>2</sub> relaxivity is almost twice the commercial Gd-DTPA-BMA contrast agent [4,13].

Molecular Dynamics simulations are very important to accurately obtain the relaxation times constants T<sub>1</sub> and T<sub>2</sub> of water hydrogens [14]. Thus, MD simulations as well as NMR spin relaxation parameters are crucial techniques to gain insights about fast internal motions. The MD simulations can provide important clues about the inter- and intramolecular motions employing empirical force fields as molecular models [15,16]. The NMR relaxation measurements yield the dipolar correlation function, from which dynamic quantities, such as generalized order parameters S<sup>2</sup> and effective correlation times  $\tau_e$ , can be obtained [16]. One method to obtain the T<sub>1</sub> and T<sub>2</sub> relaxation parameters directly from the MD calculations is by means of the spectral density. The method uses the Fourier transform of the correlation function to obtain the spectral density ( $J(\omega)$ ) [17,18]. In spite of its great relevance, little computational work has been done considering the study of the direct prediction of NMR relaxation parameters from MD simulations of MRI probes in solution [19–22]. Furthermore, it should be kept in mind that the main difficulty of MD simulations is the great number of conformations generated. Thus, for an MD analysis, this feature significantly increases the computational demand and, in some cases, it is computationally infeasible to carry out QM calculations for all structures from MD simulations. To overcome this scenario, theoretical methods of conformers selection from MD simulations can be employed [9, 20].

Thus, in this work, besides obtaining the relaxation parameters by the spectral density, the MD structures were selected by the OWSCA (Optimal Wavelet Signal Compression Algorithm) method. Up to now, this approach relating the spectral density and the OWSCA method is unpublished in the literature.

Considering this scenario, the aim of the work is to develop a theoretical protocol based on spectral density and OWSCA methodology able to obtain the relaxation parameters (T<sub>1</sub> and T<sub>2</sub>) of <sup>1</sup>H atoms of the water molecules. Following this line, we propose two Ni<sup>2+</sup> complexes ([Ni(ACAC)<sub>2</sub>(H<sub>2</sub>O)<sub>2</sub>], [Ni(TEA)]<sup>2+</sup>) as new MRI probes.

## 2. Computational methods

### 2.1. Optimization, Molecular Dynamics simulations and Optimal Wavelet Signal Compression Algorithm (OWSCA) of $Ni^{2+}$ complexes

Firstly,  $Ni^{2+}$  complexes were constructed in GaussView 5.0 and optimized in Gaussian 09 program [23] using the functional B3LYP with basis set 6-311g. Then, Molecular Dynamics (MD) simulations were performed in REAX-FF [24], which was developed and validated by van Duin and coworkers [25]. The MD simulations were performed at a physiological temperature of 310.65 K, within a domain containing 300 water molecules, which were determined by the density of liquid water ( $\rho = 0.996 \text{ g.cm}^{-3}$ ). A thermalization phase of 500 ps, followed by an additional period of 2.0 ns was assumed, leading to 400000 iterations. The simulation was performed using the force field NiCH [25], which was developed and validated for the iron oxides.

After performing the MD calculations, the Optimal Wavelet-Signal Compression Algorithm (OWSCA), which has already been successfully applied to the treatment of different systems [9,26], was used to select the most representative structures within the data set. The OWSCA is based on the discrete wavelet transform of the dataset  $x(t)$ , according to:

$$d_{j,k} = \int_{-\infty}^{\infty} x(t) \psi_{j,k}(t) dt \quad (1)$$

where  $d_{j,k}$  is the wavelet coefficient,  $t$  is the variable time (normalized between 0 and 1),  $j$  represents the scaling parameter (resolution), which determines the time and frequency resolutions of the scaled wavelet function  $\psi$  and  $k$  represents the shifting parameter, which translates the scaled wavelet along the time axis. Typically  $j$  and  $k$  are correlated, where  $j = 0 \cdots N - 1$  and  $k = 0 \cdots 2^N - 1$ , where  $N$  denotes the maximum wavelet resolution. In this way,  $\psi_{j,k}$  can be defined by Equation 2:

$$\psi_{j,k}(t) = \frac{1}{\sqrt{2^j}} \psi\left(\frac{t - k2^j}{2^j}\right) \quad (2)$$

Notice that in Equation (1) the term  $x(t)$  represents the whole dataset of MD conformations. Each conformation is denoted by the energy of MD conformation (at kcal.mol<sup>-1</sup>Å<sup>-1</sup>) at a correspondent simulation time (in fs).

In this research we have used the Haar wavelet, also known as Daubechies-1, defined according to Equation (3):

$$\boldsymbol{\psi}(t) = \begin{cases} -1 & 0 \leq t < 0.5 \\ 1 & 0.5 \leq t < 1 \\ 0 & \text{otherwise} \end{cases} \quad (3)$$

After the discrete wavelet transform the wavelet coefficients  $d_{j,k}$  are obtained. In the sequence the wavelet coefficients are thresholded with the goal to preserve only those most representative, indicating the most suitable MD conformations, according to the Equation (4). This compression procedure is given by the following optimization problem:

$$\min_{\delta} \frac{\sqrt{\sum_{i=1}^{n_x} [x(t_i) - \tilde{x}(t_i)]^2}}{n_x} \quad (4)$$

subject to:

$$\mathbf{d} = \int_{-\infty}^{\infty} x(t) \boldsymbol{\psi}(t) dt \quad (4-a)$$

$$\tilde{d}_{j,k} = 0 \text{ if } d_{j,k} \leq \delta_j, j = 0, \dots, N-1; k = 0, \dots, 2^N - 1 \quad (4-b)$$

$$\tilde{\mathbf{x}}(t) = \sum_{j=0}^{N-1} \sum_{k=0}^{2^N-1} \tilde{d}_{j,k} \psi_{j,k}(t) \quad (4-c)$$

$$\delta_{min} \ll \delta \ll \delta_{max} \quad (4-d)$$

$$I \leq 50 \quad (4-e)$$

where the coefficients  $\tilde{d}_{j,k}$  denote an individual compressed wavelet coefficient,  $\mathbf{d}$  is the vector of wavelet coefficients,  $\tilde{\mathbf{x}}(t)$  is the transformed dataset after the compression operation,  $n_x$  is the size of  $\tilde{\mathbf{x}}(t)$  and  $\mathbf{x}(t)$ . It is important to emphasize that the resultant function  $\tilde{\mathbf{x}}(t)$  is square-

shaped due to the use of Haar wavelet functions. In this way, the number of intervals is denoted by  $I$ . For optimization, we established that the maximum number of intervals must be less than 50. Notice that each step change in the  $\tilde{\mathbf{x}}(t)$  function will correspond to the selected times for the calculation of relaxation parameters.

In the system above, the goal is minimizing the objective function denoted by Equation (4), which measures the distance between the original energy of MD-conformations,  $x(t)$  and the transformed dataset after the inverse wavelet transform (Equation 4-c), considering the rule given by Equation (4-b). Thus, the optimization algorithm adjusts the compression parameters  $\boldsymbol{\delta}$ , with  $\delta_i, i = 1 \cdots N$ . For more details of the Optimal Wavelet-Signal Compression Algorithm (OWSCA) see [9] and [16].

## 2.2. Estimation of the Relaxation parameters $R_1$ and $R_2$

In this work, we focused on directly determining the relaxation time of the  $^1\text{H}$  atoms of the water molecules present within the systems under study. Since  $R_1$  and  $R_2$  relaxation rates constants play an important role in NMR spectroscopy properties and describe information how signals change with time [27], they were directly estimated from available MD results.

Firstly, the distance between the metal and the hydrogen in each conformation selected by the OWSCA procedure was calculated. Then, the autocorrelations of this set of distances were calculated and fitted to:

$$C(t) = \frac{1}{5} e^{-\frac{t}{\tau_c}} \left[ S^2 + (1 - S^2) e^{-\frac{t}{\tau_e}} \right] \quad (5)$$

where the rotational correlation time is given by  $\tau_c$ ,  $S^2$  is the order parameter and  $\tau_e$  is the effective correlation time. Once  $\tau_c$ ,  $S^2$  and  $\tau_e$  are estimated, the spectral density  $J(\omega)$  can be calculated, which is given by the Fourier transform of the correlation function [15,18].

$$J(\omega) = 2 \int_0^\infty C(t) \cos(\omega t) dt = \frac{2}{5} \left[ \frac{S^2 \tau_c}{1 + \tau_c^2 + \omega^2} + \frac{(1 - S^2) \tau}{1 + \tau^2 \omega^2} \right] \quad (6)$$

which determines the relaxation rates.

$$r_1 = \frac{1}{T_1} = K[J(\omega_0) + J(2\omega_0)] \quad (7)$$

$$r_2 = \frac{1}{T_2} = \frac{K}{4} [J(0) + 10J(\omega_0) + J(2\omega_0)] \quad (8)$$

$$K = \left(\frac{\mu_0}{4\pi}\right)^2 \frac{3\hbar^2\gamma^4 I(I+1)}{2r^6} \quad (9)$$

where,  $I$  is the spin quantum number and  $\omega_0$  is the Larmor angular frequency for the hydrogen,  $\mu_0$  vacuum permeability,  $\hbar$  Planck constant,  $r$  average distance between nuclei of  $\text{Ni}^{2+}$  (Figure 4). it is important to mention that the Larmor angular frequency refers to the rate of precession of the magnetic moment of the proton around the external magnetic field ( $B_0$ ) and gyromagnetic radius of hydrogen ( $\gamma$ ) given by  $\omega_0 = \gamma_H B_0$  [26], in this work we used  $B_0$  of 1.5 tesla and  $\gamma_H$  of 42.58 MHz/T, thus, the Larmor angular frequency of  $^1\text{H}$  would be  $(42.58 \text{ MHz/T}) \times (1.5\text{T}) = 63.87 \text{ MHz}$ .

The flowsheet of the OWSCA applied to calculate the relaxation parameters is shown in Figure 1.

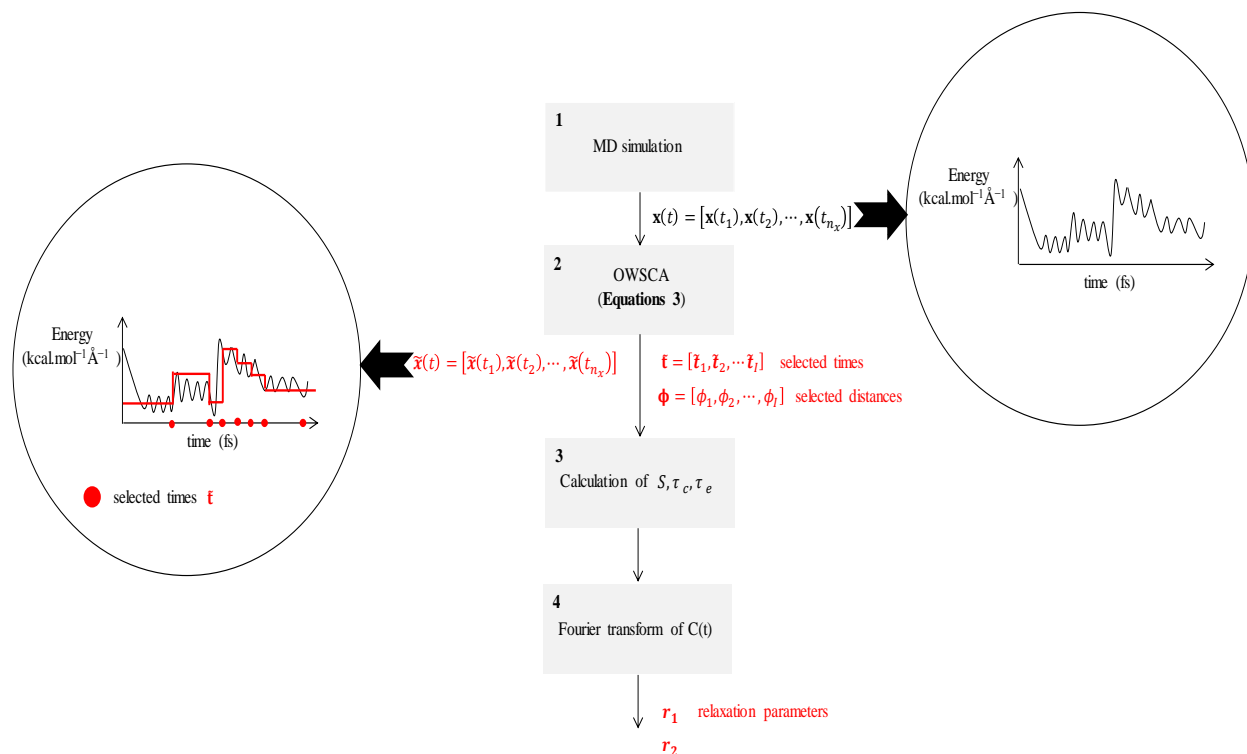
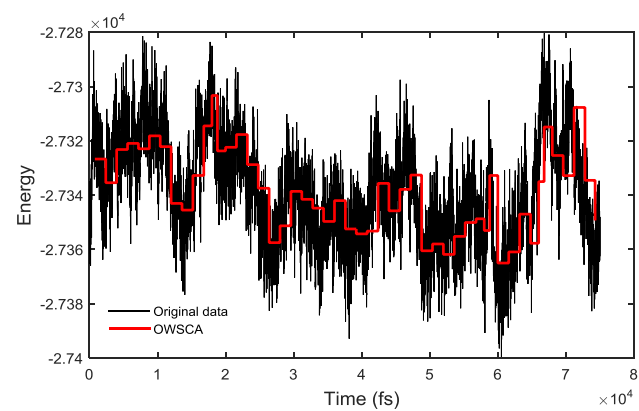


Figure 1 - Flowsheet of the OSWCA applied to calculate the relaxation parameters.

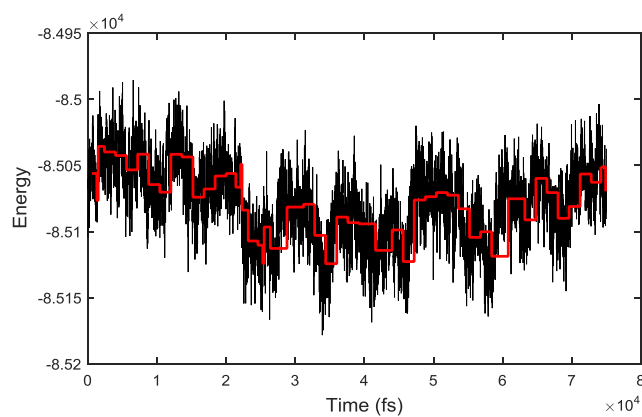
### 3-Results and Discussion

#### 3.1-Optimal Wavelet Signal Compression Algorithm (OWSCA)

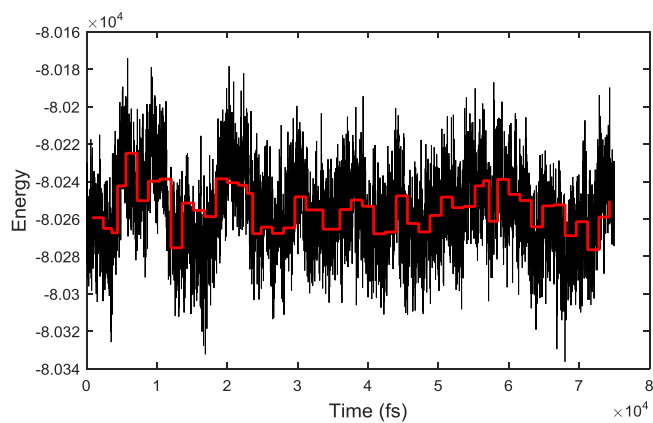
The OWSCA was able to compress the MD conformations data set from (typically) 8000 points to around 40. The comparison between the original data  $X(t)$  and the compressed data  $y(t)$  can be observed in Figure 2; the black line is the original MD signal and the red is the compromised signal (treated by OWSCA). Thus, 3 systems were treated ( $\text{Fe}_3\text{O}_4$ ,  $[\text{Ni}(\text{ACAC})_2(\text{H}_2\text{O})_2]$  and  $[\text{Ni}(\text{TEA})]^{2+}$ ) with the OWSCA method. For  $\text{Fe}_3\text{O}_4$  37 structures were obtained, for  $[\text{Ni}(\text{ACAC})_2(\text{H}_2\text{O})_2]$ , 39 structures and 49 structures for the  $[\text{Ni}(\text{TEA})]^{2+}$  complex. From the results, it is possible to observe that the application of the OWSCA methodology is given with efficiency by the high compression of points.



**a)  $\text{Fe}_3\text{O}_4$**



**b)  $[\text{Ni}(\text{ACAC})_2(\text{H}_2\text{O})_2]$**



**c)  $[\text{Ni}(\text{TEA})]^{2+}$**

Figure 2 - Energy of MD conformations (original and compressed) at each time (fs). a)  $\text{Fe}_3\text{O}_4$ , b)  $[\text{Ni}(\text{ACAC})_2(\text{H}_2\text{O})_2]$ , c)  $[\text{Ni}(\text{TEA})]^{2+}$ .



### 3.2-Validating the theoretical parameters for Relaxation Rates $R_1$ and $R_2$

We validated our methodology with magnetite (Table 1). The validation of the methodology was performed in 0.1 mM. The theoretical  $R_1$  and  $R_2$  values obtained from the molecular dynamics were 35.72 and 55.55  $s^{-1}$ , respectively. The experimental  $R_2$  value reported from the literature for magnetite is 50.50  $s^{-1}$ . Thus, there was a difference of only 5.55  $s^{-1}$  between the theoretical and experimental values. In this context, the experimental and theoretical values are quite close, which shows that the implementation of our methodology for obtaining the  $R_1$  and  $R_2$  values is quite effective. Moreover, the results indicate that the OWSCA procedure, which selects the most representative structures, is valid for the calculation of these parameters, since the simulated results were close to the experimental data. In this regard, the relaxation rates of Ni complexes were calculated following the same procedure adopted in this section, which is discussed in the next topic.

**Table 1:**  $R_1$  and  $R_2$  values of magnetite

Magnetite	$R_1(s^{-1})$	$R_2(s^{-1})$
Theoretical (MD)	35.72	55.55
<i>Experimental</i>	-	50.50 [33,34]

### 3.3- Relaxation rate constants ( $R_1$ and $R_2$ ) and Relaxivity of $Ni^{2+}$ complexes

The relaxation times and rate in liquid samples is expressed in terms of the spectral density, or the amount of energy available in the local magnetic fields in the system, at the Larmor frequency  $\omega_0$ , and the strength of the locking field  $B_0$  [6]. Thus, the spectral density describes motion frequencies that can promote relaxation that depends on the Fourier transform of the autocorrelation function, which gives the probability of finding the frequency (energy)  $\omega_0$  in the heat bath. This frequency is provided by the thermal motion of the molecule, that is characterized by certain correlation times (as already mentioned in equation 1) [28].

Based on this context, in this work, we propose two  $Ni^{2+}$  complexes as promising contrast agents in RMI,  $[Ni(ACAC)_2(H_2O)_2]$  and  $[Ni(TEA)]^{2+}$ . The ligands chosen are important for the

study, because they have OH<sup>-</sup> and H<sub>2</sub>O groups that can make hydrogen bonds with the free water molecules in the system [29, 30]. Figure 3 shows the Ni<sup>2+</sup> complexes used in this work.

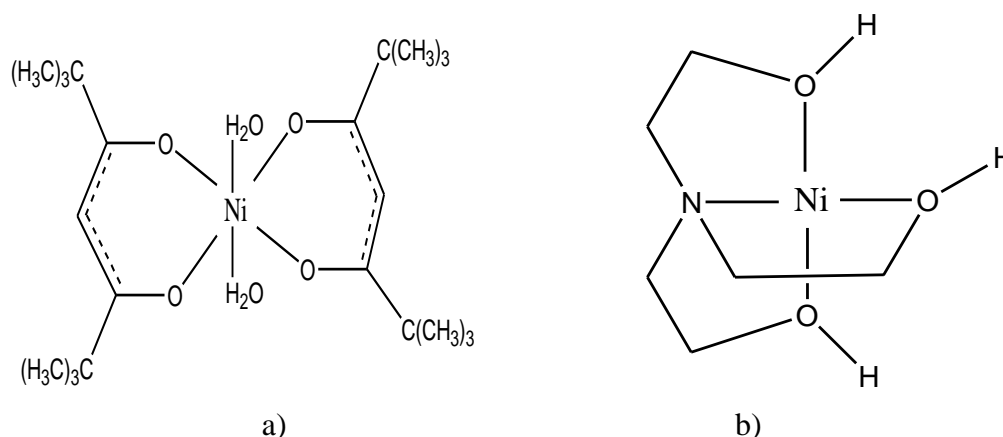


Figure 3 - Ni<sup>2+</sup> complex a) [Ni(ACAC)<sub>2</sub>(H<sub>2</sub>O)<sub>2</sub>] , b) [Ni(TEA)]<sup>2+</sup>.

In this line, with Equations 5 and 6, it is possible to compute relaxation times for the systems examined here. For this purpose, it is very important to have an accurate description of the MD calculation results, as well as to correctly evaluate the thermal effect on the relaxation parameters.

Initially, for analyzing the complex [Ni(ACAC)<sub>2</sub>(H<sub>2</sub>O)<sub>2</sub>] , it is possible to observe in Table 2 that the relaxation rate constants R<sub>1</sub> and R<sub>2</sub> values for the <sup>1</sup>H atoms were 15.37 and 23.05 s<sup>-1</sup>, respectively. Thus, the relaxation times constants T<sub>1</sub> and T<sub>2</sub> were 0.065 and 0.043 s, respectively. It is important to mention that the relaxation time is inversely proportional to the relaxation rate constants (R<sub>1</sub> = 1/T<sub>1</sub> and/or R<sub>2</sub> = 1/T<sub>2</sub>) as already shown. By analyzing, now, the complex [Ni(TEA)]<sup>2+</sup> for the <sup>1</sup>H atom, the values of 30.58 and 45.88 s<sup>-1</sup> for R<sub>1</sub> and R<sub>2</sub> were found. The relaxation times constants T<sub>1</sub> and T<sub>2</sub> were of 0.033 and 0.022 s, respectively. Thus, for both analyzed Ni<sup>2+</sup> complexes, the relaxation times were higher in T<sub>1</sub>. In fact, it is already mentioned in the literature that the Ni<sup>2+</sup> complexes act preferentially in the relaxation times constants T<sub>1</sub> [4,12]. The Figure 5 shows the MD system of the a) [Ni(ACAC)<sub>2</sub>(H<sub>2</sub>O)<sub>2</sub>] complex with the water molecules and it is possible to observe the distance, ϕ, that was used in Equation 8 for the determination of the relaxation parameters.

Surely, the results obtained from  $T_1$  and  $T_2$  were very satisfactory, moreover better than many  $Gd^{3+}$  complexes reported in the literature [24–26, 30]. One of the most commonly used CAs is the MAGNEVIST ( $[Gd(DTPA)(H_2O)]$ ), whose  $T_2$  value is 0.02s in the field of 1.5T [32, 36], thus, both  $Ni^{2+}$  complexes studied showed a relaxation time superior to that of MAGNEVIST. Another  $Gd^{3+}$  complex widely used as a CA is Gd-DOTA, whose the  $T_1$  and  $T_2$  values are 0.032 and 0.025s, respectively [31, 33]. It is worth mentioning that our results for  $Ni^{2+}$  complexes were efficient compared to Gd-DOTA. The  $[Ni(TEA)]^{2+}$  complex revealed to be very similar to Gd-DOTA, while the  $[Ni(ACAC)_2(H_2O)_2]$  complex has much higher  $T_1$  and  $T_2$  relaxation times constants than the Gd-DOTA. Thus, both complexes studied may be promising substitutes for classical CAs that are based on  $Gd^{3+}$  complexes.

In this work, we have also evaluated the relaxivity of  $Ni^{2+}$ . This parameter of a MR contrast agent is defined as the concentration-dependent increase the relaxation rate of paramagnetic agents, or how the relaxation rates of a solution change as a function of concentration  $[C]$ . Since a contrast agent can affect the two relaxation rates ( $1/T_1$  and  $1/T_2$ ) individually, there are two corresponding relaxivities, denoted  $r_1$  and  $r_2$ . The relaxivities ( $r_1(mM^{-1}s^{-1})$  and  $r_2(mM^{-1}s^{-1})$ ) are generally defined as the slope of the linear regression generated from a plot of the measured relaxation rate ( $1/T_i$ , where  $i = 1, 2$ ) *versus* concentration (equation 10) [8,36]. In this line, for calculating the relaxivity, a different number of water molecules, 300, 600 and 900, were employed.

For the  $[Ni(ACAC)_2(H_2O)_2]$  complex,  $r_1=70.72mM^{-1}s^{-1}$  and  $r_2=294.92mM^{-1}s^{-1}$  (Figure 4a) were obtained. Turning now to the  $[Ni(TEA)]^{2+}$  complex, the obtained values were  $r_1=142.82mM^{-1}s^{-1}$  and  $r_2=110.78mM^{-1}s^{-1}$ . Our findings show a very promising relaxivity value corresponding to the  $r_1$  and  $r_2$  parameters. It is worth noticing that the  $r_1$  value is around  $33.2mM^{-1}s^{-1}$  for  $Gd^{3+}$  complexes [39], thus, our results in  $r_1$  show that for both  $Ni^{2+}$  complexes a significant increase in relation to  $Gd^{3+}$  complexes. The  $r_2$  values were higher in relation to  $r_1$ , however, it is observed that for some nickel and iron oxides, the  $r_2$  values are more sensitive and higher, being that for some SPIONs these values can reach  $758 mM^{-1}s^{-1}$  [38]. In this line, our results are in agreement with those reported in the literature.

$$\frac{1}{T_i} = r_i \cdot [C] \quad (10)$$

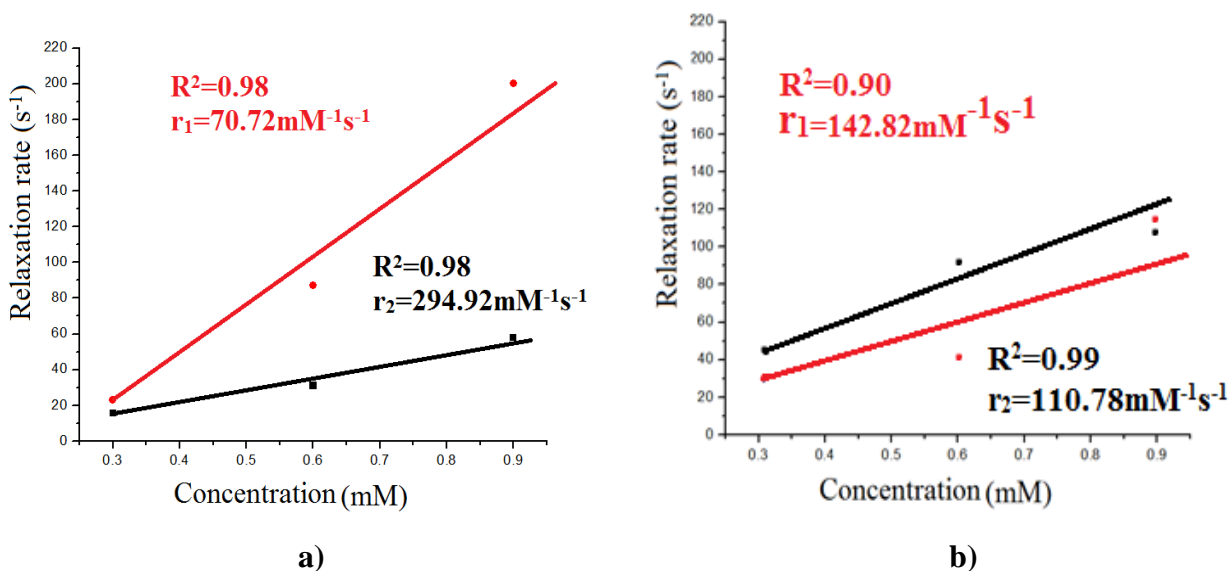


Figure 4 - Relaxivity of Ni<sup>2+</sup> complexes a) [Ni(ACAC)<sub>2</sub>(H<sub>2</sub>O)<sub>2</sub>], b) [Ni(TEA)]<sup>2+</sup>.

The results obtained showed that the [Ni(ACAC)<sub>2</sub>(H<sub>2</sub>O)<sub>2</sub>] complex had better T<sub>1</sub> and T<sub>2</sub> values than the [Ni(TEA)]<sup>2+</sup> complex. Indeed, analyzing the structure of both complexes (Figure 3), the [Ni(ACAC)<sub>2</sub>(H<sub>2</sub>O)<sub>2</sub>] complex has two water molecules, which, in fact, contribute to a relaxation time increase. Actually, there is a change between the water molecules coordinated with the metal and those of the solvent.

**Table 2:** R<sub>1</sub> and R<sub>2</sub> values of Ni<sup>2+</sup> complexes

Complexes	R <sub>1</sub> (s <sup>-1</sup> )	R <sub>2</sub> (s <sup>-1</sup> )	T <sub>1</sub> (s)	T <sub>2</sub> (s)
[Ni(ACAC) <sub>2</sub> (H <sub>2</sub> O) <sub>2</sub> ]	15.37	23.05	0.065	0.043
[Ni(TEA)] <sup>2+</sup>	30.58	45.88	0.033	0.022

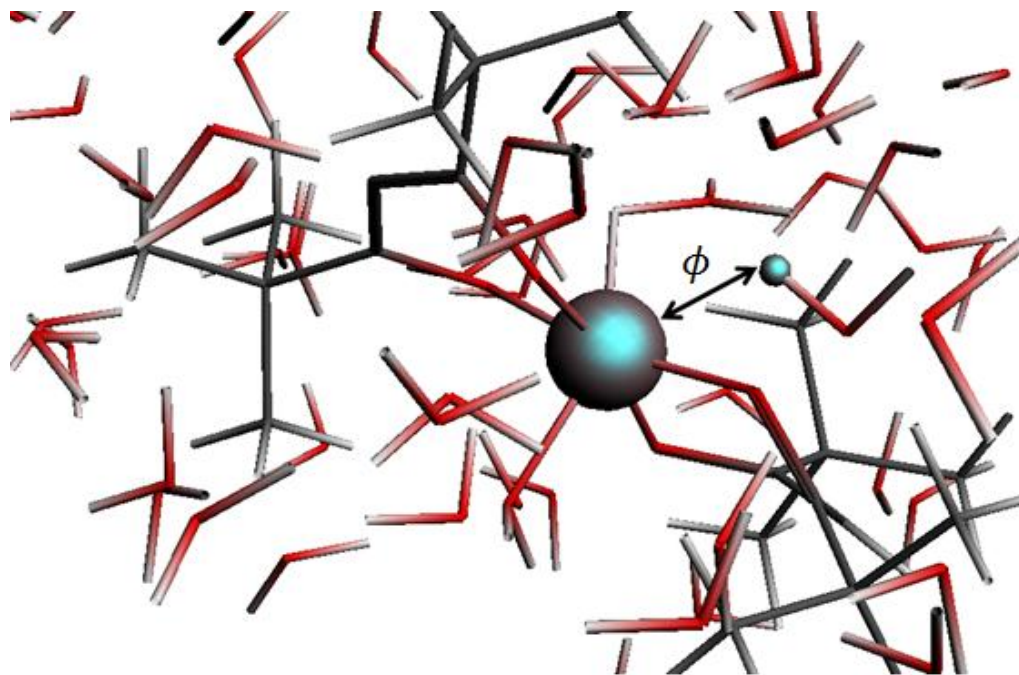


Figure 5 - MD system of the  $[\text{Ni}(\text{ACAC})_2(\text{H}_2\text{O})_2]$  complex.

#### 4.0-Conclusions

In this work, we have examined the relaxation time constants ( $T_1$  and  $T_2$ ) by means of the spectral density function ( $J(\omega)$ ) for two  $\text{Ni}^{2+}$  complexes ( $[\text{Ni}(\text{ACAC})_2(\text{H}_2\text{O})_2]$  and  $[\text{Ni}(\text{TEA})]^{2+}$ ). The methodology for  $J(\omega)$  calculations from the optimal wavelet signal compression of molecular dynamics has been validated with magnetite, obtaining a small difference between the experimental and theoretical values. Thus, we conclude that the implementation of  $J(\omega)$  has effectively been done and can be applied to various types of systems.

In addition, we present here two proposals of Contrast Agents,  $[\text{Ni}(\text{ACAC})_2(\text{H}_2\text{O})_2]$  and  $[\text{Ni}(\text{TEA})]^{2+}$ . The results are better for the  $[\text{Ni}(\text{ACAC})_2(\text{H}_2\text{O})_2]$  complex, however, both complexes were shown to be efficient and promising compared to  $\text{Gd}^{3+}$  complexes (for showing a high  $T_1$  and  $T_2$  and being less toxic). In fact, the results obtained indicate that the compounds studied can be promising CAs in MRI.

## 5.0 - Acknowledgements

The authors thank the Brazilian agencies FAPEMIG, FAPERJ, CAPES, and CNPq for the financial support of this research the UFLA and UFF for infrastructure and encouragement in this work. This work was also supported by Excellence project FIM.

## 6. Reference

- [1] C. De Angelis, R.F. Brizzi, R. Pellicano, *J. Surg. Oncol.* **2013**, 4, 230.
- [2] S. Chaudhuri, K. Basu, B. Sengupta, A. Banerjee, P.K. Sengupta, Sengupta, *J. Lumin.* **2008**, 23, 403.
- [3] M.A. Gonçalves, E.F.F. da Cunha, F.C. Peixoto, T.C. Ramalho, *Comput. Theor. Chem.* **2015**, 136, 15.
- [4] M. A. Gonçalves, T. C. Ramalho, *Rev. Virtual Quim.* **2017**, 9, 1524.
- [5] G. Bačić, A. Pavićević, F. Peyrot, *Redox Biology.* **2016**, 8, 242.
- [6] M. Lepage, J.C. Gore, *J. Phys. Conf. Ser.* **2004**, 3, 86.
- [7] M. Jaishankar, T. Tseten, N. Anbalagan, B.B. Mathew, K.N. Beeregowda, *Interdiscip. Toxicol.* **2014**, 7, 72.
- [8] M. Rohrer, H. Bauer, J. Mintorivitch, M. Requardt, H. J. Weinmann, *Invest. Radiol.* **2005**, 40, 724.
- [9] M.A. Gonçalves, L.S. Santos, D.M. Prata, F.C. Peixoto, E.F.F. da Cunha, T.C. Ramalho, *Theor. Chem. Acc.* **2017**, 136.
- [10] M. A. Perazella, *CJASN.* **2009**, 4, 469.
- [11] A.O. Olatunde, S.J. Dorazio, J. A Sperryak, J.R. Morrow, *J. Am. Chem. Soc.* **2012**, 134, 1805.
- [12] M. Carnes, D. Buccella, J.Y.-C. Chen, A.P. Ramirez, N.J. Turro, C. Nuckolls, M. Steigerwald, *Angew. Chem.* **2009**, 121, 3435.
- [13] T. Ahmad, I. Rhee, S. Hong, Y. Chang, J. Lee, *J. Nanosci. Nanotechnol.* **2011**, 11, 5650.
- [14] V.G.M. Martin Kaupp, M. Bühl, *Calculation of NMR and EPR Parameters: Theory and Applications*, **2004**.
- [15] A. Villa, G. Stock, *J. Chem. Theory Comput.* **2006**, 2, 1236.

- [16] B. Frenkel, D.; Smit, Understanding molecular simulations: from algorithms to applications, **1996**.
- [17] P. Chen, M. Hologne, O. Walker, J. Hennig, *J. Chem. Theory Comput.* **2018**, 19.
- [18] J.P. Grivet, *J. Chem. Theory Comput.* **2005**, 123, 8.
- [19] O. V Yazyev, L. Helm, *J. Chem. Phys.* **2007**, 127, 84506.
- [20] M. A. Gonçalves, F.C. Peixoto, E.F.F. da Cunha, T.C. Ramalho, *Chem. Phys. Lett.* **2014**, 609, 92.
- [21] A. Lasoroski, R. Vuilleumier, R. Pollet, *J. Chem. Phys.* **2013**, 139, 104115.
- [22] V. Patinec, G.A. Rolla, M. Botta, R. Tripier, D. Esteban-Gomez, C. Platas-Iglesias, *Inorg. Chem.* **2013**, 52, 11184.
- [23] M.J. Frisch, G.W. Trucks, H.B. Schlegel, G.E. Scuseria, M.A. Robb, J.R. Cheeseman, G. Scalmani, V. Barone, B. Mennucci, G.A. Petersson, H. Nakatsuji, M. Caricato, X. Li, H.P. Hratchian, A.F. Izmaylov, J. Bloino, G. Zheng, J.L. Sonnenberg, M. Hada, M. Ehara, K. Toyota, R. Fukuda, J. Hasegawa, M. Ishida, T. Nakajima, Y. Honda, O. Kitao, H. Nakai, T. Vreven, J.A. Montgomery Jr., J.E. Peralta, F. Ogliaro, M. Bearpark, J.J. Heyd, E. Brothers, K.N. Kudin, V.N. Staroverov, R. Kobayashi, J. Normand, K. Raghavachari, A. Rendell, J.C. Burant, S.S. Iyengar, J. Tomasi, M. Cossi, N. Rega, J.M. Millam, M. Klene, J.E. Knox, J.B. Cross, V. Bakken, C. Adamo, J. Jaramillo, R. Gomperts, R.E. Stratmann, O. Yazyev, A.J. Austin, R. Cammi, C. Pomelli, J.W. Ochterski, R.L. Martin, K. Morokuma, V.G. Zakrzewski, G.A. Voth, P. Salvador, J.J. Dannenberg, S. Dapprich, A.D. Daniels, Ö. Farkas, J.B. Foresman, J.V. Ortiz, J. Cioslowski, D.J. Fox, Gaussian Inc., Wallingford CT, 2009.
- [24] A. van Duin, ReaxFF User Manual, **2002**.
- [25] K. Chenoweth, A.C.T. van Duin, W. A. Goddard, *J. Phys. Chem. A.* **2008**, 112, 1053.
- [26] M.A. Gonçalves, L.S. Santos, F.C. Peixoto, E.F.F. da Cunha, T.C. Silva, T.C. Ramalho, *ChemistrySelect* **2017**, 2, 10142.
- [27] F. Nmr, G. Gonzhlez, D.H. Powell, V. Tissieres, A.E. Merbach, *J. Phys. Chem.* **1994**, 98, 59.
- [28] J. Larmor, *Philos. Mag.* **1897**, 44, 512.
- [29] G. M. Clore, J. Iwahara, *Chem. Rev.* **2009**, 109, 4139.
- [30] N.G.R. Hearn, E.M. Fatila, R. Clérac, M. Jennings, K.E. Preuss, *Inorg. Chem.* **2008**, 47, 10341.
- [31] F. Uggeri, S. Aime, P.L. Anelli, M. Botta, M. Brocchetta, C. De Haën, G. Ermondi, M. Grandi, P. Paoli. *Inorg. Chem.* **1995**, 34, 642.
- [32] P.J. Klemm, W.C. Floyd, D.E. Smiles, J.M.J. Fréchet, K.N. Raymond, *Contrast Media Mol. Imaging.* **2012**, 7, 99.

- [33] A. Kastrup, G.H. Glover, *Magn. Reson. Med.* **2001**, 604, 604.
- [34] E. Boros, M. Polasek, Z. Zhang, P. Caravan, *J. Am. Chem. Soc.* **2012**, 134, 19868.
- [35] F. Xu, C. Cheng, D.-X. Chen, H. Gu, *ChemPhysChem.* **2012**, 13, 341.
- [36] C. Paquet, H.W. De Haan, D.M. Leek, H.Y. Lin, B. Xiang, G. Tian, A. Kell, B. Simard, *ACS Nano.* **2011**, 5, 3112.
- [37] Rohrer. M, Bauer. H, Mintorovitch. J, Requardt. M, Weinmann, H. J. *Invest. Radiol.* **2005**, 40, 724.
- [38] A. Saha, S. c. Mohanta, K. Deka, P. Deb, P. S. Devi, *ACS Appl. Mater. Interfaces* **2017**, 9, 4141.
- [39] G. Kotek, S. T. van Tiel, P. A. Wielopolski, G. C. Houston, G. P. Krestin, M. R Bernsen, *Contrast Media Mol. Imaging* **2012**, 7, 203



## GENERAL CONCLUSION

The development of new contrast agents for MRI is very important and promising due to the scarcity of articles in the literature addressing these new probes. In fact, the problems faced with the toxicity of  $\text{Gd}^{2+}$  complexes require new investigations of compounds capable of replacing them.

Thus, in the present work, we studied several compounds of iron oxides (SPIONs) and  $\text{Ni}^{2+}$  complexes (paraCEST) as promising CAs for MRI. For this purpose,  $A_{\text{iso}}$  calculations were performed for the water molecules ( $^1\text{H}$  and  $^{17}\text{O}$  atoms) of the system. The results showed a considerable increase in  $A_{\text{iso}}$  values when the SPIONs and paraCEST are introduced within the system with the water molecules. This increase can be attributed, in large part, to the hydrogen bonds, confirmed by QTAIM and NCI calculations. In this work, a new selection method of MD structures (entitled OWSCA) has been developed as well as we have calculated the relaxation times through the spectral density function ( $J(\omega)$ ).

In general, the results of the calculations indicate that the compounds studied may be possible substitutes for the classical contrast agents based on  $\text{Gd}^{2+}$ . The SPIONs and paraCESTs are able to decrease relaxation times ( $T_1$  and  $T_2$ ). It is also important to mention that the OWSCA method was used successfully; thus, the method can be used in the selection of conformations of several MD systems.

# ATTACHMENT

## Works Developed



Contents lists available at [ScienceDirect](#)

Chemical Physics Letters

journal homepage: [www.elsevier.com/locate/cplett](http://www.elsevier.com/locate/cplett)



### Dynamics, NMR parameters and hyperfine coupling constants of the $\text{Fe}_3\text{O}_4(100)$ -water interface: Implications for MRI probes



Mateus A. Gonçalves<sup>a</sup>, Fernando C. Peixoto<sup>b</sup>, Elaine F.F. da Cunha<sup>a</sup>, Teodorico C. Ramalho<sup>a,\*</sup>

<sup>a</sup> Department of Chemistry, Federal University of Lavras, P.O. Box 3037, 37200-000 Lavras, MG, Brazil

<sup>b</sup> Department of Chemical and Petroleum Engineering (UFF), Rua Passo da Pátria, 156, Niterói, RJ, Brazil

#### ARTICLE INFO

##### Article history:

Received 12 February 2014

In final form 16 June 2014

Available online 23 June 2014

#### ABSTRACT

Magnetite is an iron oxide widely used as contrast agent in MRI, receiving considerable interest from nanoscience and nanotechnology. In this work, the face 100 of the magnetite structure was studied with water in order to obtain <sup>1</sup>H hyperfine coupling constants (HFCCs). Molecular dynamics (MD) calculations were performed using the ReaxFF program and for statistical inefficiency, structures were selected for HFCC and NMR calculations. From our theoretical findings, the magnetite in solution considerably increases the <sup>1</sup>H HFCC of water molecules. From our results, it is essential to incorporate the dynamics and solvent effects into NMR calculations of relaxation parameters.

© 2014 Elsevier B.V. All rights reserved.

Hindawi Publishing Corporation  
Journal of Chemistry  
Volume 2014, Article ID 754526, 6 pages  
<http://dx.doi.org/10.1155/2014/754526>



#### Research Article

### Use of Ethylenediaminetetraacetic Acid as a Scavenger for Chromium from “Wet Blue” Leather Waste: Thermodynamic and Kinetics Parameters

José E. Resende,<sup>1</sup> Mateus A. Gonçalves,<sup>1</sup> Luiz C. A. Oliveira,<sup>2</sup>  
Elaine F. F. da Cunha,<sup>1</sup> and Teodorico C. Ramalho<sup>1,3</sup>

<sup>1</sup> Departamento de Química, Universidade Federal de Lavras, Caixa Postal 3037, 37200-000 Lavras, MG, Brazil

<sup>2</sup> Departamento de Química, ICEX, UFMG, Campus Pampulha, 31270-901 Belo Horizonte, MG, Brazil

<sup>3</sup> Biomedical Research Center, University Hradec Kralove, Hradec Kralove, Czech Republic

Correspondence should be addressed to Teodorico C. Ramalho; [teo@dqf.ufla.br](mailto:teo@dqf.ufla.br)

Received 3 July 2014; Revised 2 September 2014; Accepted 4 September 2014; Published 11 December 2014

Academic Editor: Davut Avci

Copyright © 2014 José E. Resende et al. This is an open access article distributed under the Creative Commons Attribution License, which permits unrestricted use, distribution, and reproduction in any medium, provided the original work is properly cited.

One serious consequence of the current consumer society is the transformation of the environment into a waste receptacle arising from human activities. Because of the potential toxic effects of chromium solid waste containing this metal there are grounds for serious concern for the tanning and leather processing industry. The application of tannery waste as organic fertilizer has led to extensive contamination by chromium in agricultural areas and may cause the accumulation of this metal in soils and plants. This work evaluated the extraction of  $\text{Cr}^{+3}$  and  $\text{Cr}^{+6}$  contained in solid waste from the leather industry through density functional theory (DFT) calculations. The Gibbs free energy calculations reveal that the chelator ethylenediaminetetraacetic acid (EDTA) forms more stable complexes with metal ions of chromium compared with the structures of the complexes  $[\text{Cr}(\text{NTA})(\text{H}_2\text{O})_2]$  and  $[\text{Cr-collagen}]$ , the latter used to simulate the protein bound chrome leather.

Research Article

## Molecular Modeling Studies of Piperidine Derivatives as New Acetylcholinesterase Inhibitors against Neurodegenerative Diseases

Elaine F. F. da Cunha,<sup>1</sup> José E. Resende,<sup>1</sup> Tanos C. C. Franca,<sup>2</sup> Mateus Aquino Gonçalves,<sup>1</sup> Felipe R. de Souza,<sup>2</sup> Leticia Santos-Garcia,<sup>1</sup> and Teodorico C. Ramalho<sup>1</sup>

<sup>1</sup> Departamento de Química, Campus Universitário—UFLA, Universidade Federal de Lavras, 37200-000 Lavras, MG, Brazil

<sup>2</sup> Laboratory of Molecular Modeling Applied to Chemical and Biological Defense (LMCBD), Military Institute of Engineering, Rio de Janeiro, Brazil

Correspondence should be addressed to Teodorico C. Ramalho; [teo@dqi.ufla.br](mailto:teo@dqi.ufla.br)

Received 19 April 2013; Revised 7 September 2013; Accepted 15 September 2013

Academic Editor: George Psomas

Computational and Theoretical Chemistry 1069 (2015) 96–104



Contents lists available at ScienceDirect

Computational and Theoretical Chemistry

journal homepage: [www.elsevier.com/locate/comptc](http://www.elsevier.com/locate/comptc)



### Probing thermal and solvent effects on hyperfine interactions and spin relaxation rate of $\delta$ -FeOOH(100) and $[\text{MnH}_3\text{buea}(\text{OH})]^{2-}$ : Toward new MRI probes



Mateus A. Gonçalves<sup>a</sup>, Elaine F.F. da Cunha<sup>a</sup>, Fernando C. Peixoto<sup>b</sup>, Teodorico C. Ramalho<sup>a,c,\*</sup>

<sup>a</sup> Department of Chemistry, Federal University of Lavras, P.O. Box 3037, 37200-000 Lavras, MG, Brazil

<sup>b</sup> Department of Chemical and Petroleum Engineering (UFF) Rua Passo da Pátria, 156, Niterói, RJ, Brazil

<sup>c</sup> Center for Basic and Applied Research, Faculty of Informatics and Management, University of Hradec Kralove, Hradec Kralove, Czech Republic

#### ARTICLE INFO

Article history:  
Received 13 May 2015  
Received in revised form 4 July 2015  
Accepted 4 July 2015  
Available online 21 July 2015

Keywords:  
Contrast agents  
MRI  
Molecular dynamics

#### ABSTRACT

Cancer is a global epidemic, which significantly affects all ages and socio-economic groups and one reason is the great difficulty of the initial diagnostic phase. The Magnetic Resonance Imaging (MRI), through effective contrast agents, has greatly helped in the diagnosis at the initial stage. Recently, superparamagnetic iron oxide nanoparticles and complexes with  $\text{Mn}^{2+}$  have received great attention due to their applications as contrast agents for Magnetic Resonance Imaging (MRI). Those materials can shorten the  $T_2$  and  $T_2^*$  transverse relaxation times. Thus, in this work, the face 100 of the  $\delta$ -FeOOH and the complex  $[\text{MnH}_3\text{buea}(\text{OH})]^{2-}$  were studied with explicit water molecules in order to obtain the  $^1\text{H}$  and  $^{17}\text{O}$  hyperfine coupling constants (HFCCs). Molecular dynamics (MD) simulations were performed using the ReaxFF program for subsequent statistical inefficiency calculations. Thus, the structures from the MD simulation were selected for HFCC calculations. The theoretical results suggest that the  $\delta$ -FeOOH and  $[\text{MnH}_3\text{buea}(\text{OH})]^{2-}$  considerably increase the  $^1\text{H}$  and  $^{17}\text{O}$  hyperfine coupling constants of the water molecules. In addition,  $\delta$ -FeOOH is sensitive to  $^1\text{H}$  and  $^{17}\text{O}$  HFCCs parameters, however, in the complex  $[\text{MnH}_3\text{buea}(\text{OH})]^{2-}$ ,  $^{17}\text{O}$  is much more sensitive than  $^1\text{H}$  in relation to the HFCC parameters. Our findings point out  $\delta$ -FeOOH as a promising alternative to conventional contrast agents.

© 2015 Elsevier B.V. All rights reserved.

# Planejamento Fatorial para a Investigação das Propriedades Espectroscópicas, Efeitos Relativísticos e de Solvatação de Derivados Halogenados da 2-Amino-1,4-Naftoquinona

Eduardo P. Rocha, Lívia C. T. Lacerda, Mateus A. Gonçalves, Maíra S. Pires, Telles C. Silva, Henrique A. Rodrigues & Teodorico C. Ramalho

Applied Catalysis B: Environmental 192 (2016) 286–295



ELSEVIER

Contents lists available at [ScienceDirect](http://ScienceDirect)

Applied Catalysis B: Environmental

Journal homepage: [www.elsevier.com/locate/apcatb](http://www.elsevier.com/locate/apcatb)



Boron as a promoter in the goethite ( $\alpha$ -FeOOH) phase: Organic compound degradation by Fenton reaction



Aline M. Mesquita, Iara R. Guimarães\*, Guilherme M.M.de Castro, Mateus A. Gonçalves, Teodorico C. Ramalho, Mário C. Guerreiro

Department of Chemistry, Federal University of Lavras, P.O. Box 3037, Lavras, CEP 37200-000 Minas Gerais, Brazil





Artigo

**Agentes de Contraste para Imagem por Ressonância Magnética:  
Uma Revisão**

Gonçalves, M. A; Ramalho, C. T.\*

*Rev. Virtual Quim.*, 2017, 9 (4), 1511-1524. Data de publicação na Web: 5 de julho de 2017

<http://rvq.sbq.org.br>

Hindawi  
Journal of Chemistry  
Volume 2017, Article ID 8102812, 8 pages  
<http://doi.org/10.1155/2017/8102812>



*Research Article*


**Exploring EPR Parameters of  $^{99}\text{Tc}$  Complexes for Designing New MRI Probes: Coordination Environment, Solvent, and Thermal Effects on the Spectroscopic Properties**

**Bruna T. L. Pereira,<sup>1</sup> Érika Ferreira Silva,<sup>1</sup> Mateus A. Gonçalves,<sup>1</sup>  
Daiana T. Mancini,<sup>1</sup> and Teodorico C. Ramalho<sup>1,2</sup>**

<sup>1</sup>Department of Chemistry, Federal University of Lavras, P.O. Box 3037, 37200-000 Lavras, MG, Brazil

<sup>2</sup>Center for Basic and Applied Research, Faculty of Informatics and Management, University of Hradec Kralove, Hradec Kralove, Czech Republic


## Theoretical structural and electronic analyses with emphasis on the reactivity of iron oxide prototypes in methane C–H bond activation

Telles Cardoso Silva<sup>1</sup> · Katia Júlia de Almeida<sup>1</sup> ·  
Maíra dos Santos Pires<sup>1</sup> · Alexandre Alves de Castro<sup>1</sup> ·  
Mateus Aquino Gonçalves<sup>1</sup> · Elaine Fontes Ferreira da Cunha<sup>1</sup> ·  
Teodorico Castro Ramalho<sup>1,2</sup> 

Received: 30 June 2016 / Accepted: 23 October 2016 / Published online: 1 November 2016  
© Akadémiai Kiadó, Budapest, Hungary 2016

REGULAR ARTICLE

## Optimal wavelet signal compression as an efficient alternative to investigate molecular dynamics simulations: application to thermal and solvent effects of MRI probes

Mateus A. Gonçalves<sup>1</sup> · Lizandro S. Santos<sup>2</sup> · Diego M. Prata<sup>2</sup> · Fernando C. Peixoto<sup>2</sup> ·  
Elaine F. F. da Cunha<sup>1</sup> · Teodorico C. Ramalho<sup>1,3</sup> 

Received: 11 August 2016 / Accepted: 2 December 2016  
© Springer-Verlag Berlin Heidelberg 2016